MICROSTRUCTURAL EVOLUTION AND MECHANICAL PROPERTIES OF MAGNESIUM ALLOY/AUSTENITIC STAINLESS STEEL JOINTS PRODUCED BY RESISTANCE SPOT WELDING TECHNIQUES

SUNUSI MARWANA MANLADAN

FACULTY OF ENGINEERING
UNIVERSITY OF MALAYA
KUALA LUMPUR

2017

MICROSTRUCTURAL EVOLUTION AND MECHANICAL PROPERTIES OF MAGNESIUM ALLOY/AUSTENITIC STAINLESS STEEL JOINTS PRODUCED BY RESISTANCE SPOT WELDING TECHNIQUES

SUNUSI MARWANA MANLADAN

THESIS SUBMITTED IN FULFILMENT OF THE REQUIREMENTS FOR THE DEGREE OF DOCTOR OF PHILOSOPHY

**FACULTY OF ENGINEERING
UNIVERSITY OF MALAYA
KUALA LUMPUR**

2017

UNIVERSITY OF MALAYA

ORIGINAL LITERARY WORK DECLARATION

Name of Candidate: **Sunusi Marwana Manladan**

Matric No: **KHA140019**

Name of Degree: **Doctor of Philosophy**

Title of Thesis ("this Work"):

MICROSTRUCTURAL EVOLUTION AND MECHANICAL PROPERTIES OF MAGNESIUM ALLOY/AUSTENITIC STAINLESS STEEL JOINTS PRODUCED BY RESISTANCE SPOT WELDING TECHNIQUES

Field of Study: **Manufacturing Processes**

I do solemnly and sincerely declare that:

(1) I am the sole author/writer of this Work;
(2) This Work is original;
(3) Any use of any work in which copyright exists was done by way of fair dealing and for permitted purposes and any excerpt or extract from, or reference to or reproduction of any copyright work has been disclosed expressly and sufficiently and the title of the Work and its authorship have been acknowledged in this Work;
(4) I do not have any actual knowledge nor do I ought reasonably to know that the making of this work constitutes an infringement of any copyright work;
(5) I hereby assign all and every rights in the copyright to this Work to the University of Malaya ("UM"), who henceforth shall be owner of the copyright in this Work and that any reproduction or use in any form or by any means whatsoever is prohibited without the written consent of UM having been first had and obtained;
(6) I am fully aware that if in the course of making this Work I have infringed any copyright whether intentionally or otherwise, I may be subject to legal action or any other action as may be determined by UM.

Candidate's Signature Date:

Subscribed and solemnly declared before,

Witness's Signature Date:

Name:

Designation:

MICROSTRUCTURAL EVOLUTION AND MECHANICAL PROPERTIES OF MAGNESIUM ALLOY/AUSTENITIC STAINLESS STEEL JOINTS PRODUCED BY RESISTANCE SPOT WELDING TECHNIQUES

ABSTRACT

Multi-material design is gaining prominence as an efficient strategy to reduce the weight of vehicles, improve crash-worthiness, balance cost, and reduce environmental pollution. Mg alloys and austenitic stainless steels (ASS) have been identified as excellent candidates for next generation vehicle structures. Therefore, it is imperative to develop reliable means of joining them together. Resistance spot welding (RSW) is the most widely used sheet joining process. However, joining Mg alloys to steel by RSW is extremely challenging due differences in physical and metallurgical properties. In this research, different RSW techniques, namely, resistance element welding (REW), resistance spot weld bonding (RSWB), and resistance element weld bonding (REWB), were employed to join 1.5-mm-thick AZ31 Mg alloy and 0.7-mm-thick 316L ASS. For the purpose of comparison, RSW and adhesive bonding (AB) were also used. The microstructural evolution and mechanical properties of the joints were characterized using optical microscopy, scanning electron microscopy, energy dispersive spectroscopy, micro-hardness, and tensile-shear tests. The RSW joints were found to be produced through welding-brazing mode, in which the Mg alloy melted and spread on the solid ASS, forming a nugget only in the Mg alloy. The microstructure of the nugget consisted of only columnar dendritic structure, indicating that columnar-to-equiaxed transition was interrupted. Shrinkage porosity and cracking were also observed in the nugget. In contrast, a two-zone nugget was formed during REW, consisting of a peripheral nugget on the ASS side and the main nugget. The macroscophic morphology and microstructures of the RSWB and REWB joints were similar to those of traditional RSW and REW joints, respectively. However, compared with the RSW and REW joints, the RSWB and REWB

joints possessed larger bonding diameter and nugget diameter, respectively. Overall, the traditional RSW joints exhibited inferior mechanical performance with a peak load of 2.23 kN and energy absorption of 1.14 J. The REWB joints possessed the best performance, with outstanding energy absorption. Compared with the RSW joints, the REWB joints showed 238 % higher peak load and 51 times higher energy absorption; RSWB joints showed 187 % higher peak load and 24 times higher energy absorption; AB joints showed 111% higher peak load and 7 times higher energy absorption; and REW joints showed 66% higher peak load and 9 times higher energy absorption. Irrespecive of the welding current, the RSW joints failed in interfacial failure mode, while the failure mode of REW joints transited from interfacial to pullout mode with increase in welding current. The RSWB joints exhibited a hybrid failure mode comprising of delamination at the Mg/adhesive interface, cohesive failure in the adhesive, and interfacial failure. With increase in welding current, the failure mode of the REWB joints changed from hybrid failure mode involving delamination at both the Mg/adhesive and adhesive/ASS interfaces, cohesive, and pullout failure to a hybrid failure involving delamination at Mg/adhesive interface and failure in the Mg alloy. Therefore, RSWB and especially REWB could be reliable techniques for joining Mg alloy and stainless steels to obtain high peak load, outstanding energy absorption, and favorable failure mode.

Keywords: Resistance spot welding, resistance element welding, weld-bonding magnesium alloy, austenitic stainless steel

EVOLUSI MIKROSTRUKTUR DAN SIFAT-SIFAT MEKANIK SAMBUNGAN ALOI MAGNESIUM DAN KELULI TAHAN KARAT AUSTENITIK YANG DIHASILKAN OLEH TEKNIK KIMPALAN TEMPAT RINTANGAN

ABSTRAK

Reka bentuk pelbagai bahan sedang menjadi semakin terkenal sebagai strategi yang paling berkesan untuk mengurangkan berat kenderaan, meningkatkan daya tahan kemalangan, mengimbangi kos, dan mengurangkan pencemaran alam sekitar. Penggunaan aloi Mg dan keluli tahan karat austenit (ASS) telah dikenalpasti sebagai bahan yang terbaik untuk struktur kenderaan bagi generasi akan datang. Oleh itu, membangunkan cara yang boleh dipercayai untuk menggabungkan kedua-dua bahan tersebut adalah amat penting. Rintangan titik kimpalan (RSW) adalah proses yang paling biasa digunakan untuk penggabungan kepingan. Walau bagaimanapun, menggabungkan aloi Mg pada keluli menggunakan RSW adalah amat mencabar kerana perbezaan dari segi fizikal dan logam antara mereka. Dalam kajian ini, variasi teknik RSW iaitu rintangan elemen kimpalan (REW), ikatan rintangan titik kimpalan (RSWB) dan ikatan rintangan elemen kimpalan (REWB) telah digunakan untuk menggabungkan aloi AZ31 Mg dengan ketebalan 1.5 mm dan 316L ASS dengan ketebalan 0.7 mm. Untuk tujuan perbandingan, RSW dan ikatan pelekat (AB) juga telah digunakan. Perkembangan mikrostruktural dan sifat mekanikal sambungan itu dicirikan dengan menggunakan mikroskopi optik, mikroskopi pengimbasan elektron, spektroskopi penyebaran tenaga, kekerasan mikro, dan ujian tegangan-ricih. Sambungan RSW didapati dihasilkan melalui mod pematerian kimpalan, di mana aloi Mg yang dicairkan dan dituang ke atas ASS pepejal, membentuk nugget hanya dalam aloi Mg. Strukturmikro ketulan RSW yang hanya mengandungi struktur dendritik kolumnar, menunjukkan bahawa peralihan kolumnar ke sama dimensi telah terganggu. Pengecutan keliangan dan keretakan juga diperhatikan di dalam nugget RSW. Sebaliknya, dua bahagian nugget telah dibentuk semasa REW, yang terdiri daripada nugget periferal di bahagian ASS dan nugget utama. Morfologi makroskopik dan mikrostruktur sambungan RSWB dan REWB adalah sama dengan sambungan RSW dan REW tradisional. Walau bagaimanapun, berbanding sambungan RSW dan REW, sambungan RSWB dan REWB masing-masing mempunyai diameter ikatan dan diameter nugget yang lebih besar. Secara keseluruhan, sambungan RSW tradisional menunjukkan prestasi mekanikal yang rendah dengan beban puncak 2.23 kN dan penyerapan tenaga 1.14 J. Sambungan REWB mempunyai prestasi yang terbaik, dengan penyerapan tenaga yang cemerlang. Berbanding dengan sambungan RSW, sambungan REWB menunjukkan beban puncak 238% lebih tinggi, penyerapan tenaga sebanyak 51 kali lebih tinggi; Sambungan RSWB menunjukkan beban puncak 187% lebih tinggi dan penyerapan tenaga sebanyak 24 kali lebih tinggi; sambungan AB menunjukkan beban puncak 111% lebih tinggi, penyerapan tenaga 7 kali lebih tinggi; dan sambungan REW menunjukkan beban puncak 66%, penyerapan tenaga 9 kali lebih tinggi. Tanpa megira arus kimpalan, sambungan RSW gagal dalam mod kegagalan antara muka, manakala mod kegagalan sambungan REW ditransmisikan dari mod antara muka ke mod tarik-keluar dengan peningkatan arus kimpalan. Sambungan RSWB mempamerkan mod kegagalan hibrid yang terdiri daripada pemisahan pada antara muka Mg/pelekat, kegagalan padu dalam pelekat, dan kegagalan antara muka. Dengan peningkatan arus kimpalan, mod kegagalan sambungan REWB berubah daripada mod kegagalan hybrid yang melibatkan pemisahan pada kedua-dua antara muka Mg/pelekat dan pelekat/ASS, kegagalan padu dan tarik-keluar pada kegagalan hibrid yang melibatkan pemisahan pada antara muka Mg/adhesif dan kegagalan dalam aloi Mg. RSWB dan terutamanya REWB boleh menjadi teknik yang berkesan untuk menyambungkan aloi Mg dan keluli tahan karat dengan beban puncak yang tinggi, penyerapan tenaga yang cemerlang, dan mod kegagalan yang menggalakkan.

Keywords: Resistance spot welding, resistance element welding, weld-bonding magnesium alloy, austenitic stainless steel

ACKNOWLEDGEMENTS

All thanks are due to Allah, by Whose favor good deeds are accomplished. May peace, mercy, and blessings of Allah be upon Prophet Muhammad.

I would like to express my profound gratitude to my able supervisors, Prof. Ir. Dr Ramesh Singh and Associate Prof. Dr Farazila Binti Yusof, for their guidance, support, and the stupendous supervision of this work.

My profound gratitude also goes to Prof. Zhen Luo for his guidance and support during my stay as an exchange student in the School of Materials Science and Engineering, Tainjin University, China. I am also grateful to all members of his group for their support and friendship, especially Dr Sansan Ao, Dr Ziming Liu, Zhang Yu, Cui Shuanglin, Zeng Yi Da, Ling Zhangxian, Cai Le, Shan He, Bi Jing, and Weidong Liu.

I am immensely grateful to my dear parents, Alh. Marwana Manladan and Hajiya Aishatu Marwana Manladan, for their unwavering support, guidance, and prayers. I also wish to thank all my family members and friends for their support and prayers, and all those who have contributed in one way or the other towards the success of this work.

I would like to thankfully acknowledge University of Malaya and Tianjin University, China for providing the facilities for this research. This research was supported financially by University of Malaya Post Graduate Research Grant (PG020-2015A).

Finally, I would like to thank my employer, Bayero University, Kano, Nigeria, for awarding me Tertiary Education Trust Fund (TETFund) scholarship to pursue my doctorate degree, and for providing good service conditions.

TABLE OF CONTENTS

LIST OF FIGURES

LIST OF TABLES

LIST OF SYMBOLS AND ABBREVIATIONS

AB	:	Adhesive bonding
ASS	:	Austenitic stainless steel
BM	:	Base metal
BMF	:	Base metal fracture
CDZ	:	Columnar dendritic zone
CET	:	Columnar-to-equiaxed transition
CGUCHAZ	:	Coarse grain upper critical heat affected zone
EDZ	:	Equiaxed dendritic zone
EMS	:	Electromagnetic stirring
F	:	Electrode force
FESEM	:	Field emission scanning electron microscope
FGUCHAZ	:	Fine grain upper critical heat affected zone
FZ	:	Fusion zone
G	:	Temperature gradient
HAZ	:	Heat affected zone
HV	:	Vickers hardness number
I	:	Welding current
IF	:	Interfacial failure
IMC	:	Intermetallic compound
J	:	Joule
kA	:	Kilo ampere
kN	:	Kilo Netwon
LSWB	:	Laser spot weld-bonding

mm	:	Millimeter
N	:	Newton
PIF	:	Partial interfacial failure
PMZ	:	Partially melted zone
PO	:	Pullout failure
R	:	Solidification growth rate
REW	:	Resistance element welding
REWB	:	Resistance element weld-bonding
RSW	:	Resistance spot welding
RSWB	:	Resistance spot weld-bonding
SEM	:	Scanning electron microscope
T	:	Welding time
TS	:	Tensile-shear test
USWB	:	Ultrasonic spot weld-bonding

CHAPTER 1: INTRODUCTION

Climate change is a major global threat. The transportation industry is applying growing efforts to reduce vehicles weight, and consequently reduce fossil fuel combustion and greenhouse gas emission. Therefore, different lightweight materials are increasingly being developed and incorporated into automotive and aerospace structures.

As the lightest structural materials, with superior specific strength, magnesium (Mg) alloys have great potentials for weight savings. Therefore, they are excellent materials for the transportation industry. Other remarkable properties which make Mg alloys attractive for the transportation industry include high elastic modulus, strong ability to withstand shock loads, hot formability, good castability, damping capacity, and recyclability (Patel et al., 2013; Zhang et al., 2015).

On the other hand, steel is currently the primary structural material in the transportation industry. Stainless steels possess superior corrosion resistance and excellent mechanical properties that meet the stringent requirements of the transportation industry on crash-safety standards and weight reduction potentials. In particular, austenitic stainless steels (ASS) possess high strength and durability, unique work-hardening behavior, high formability, excellent energy absorption capability, and decorative appearance. It has been demonstrated through the Next Generation Vehicle project (Schuberth et al., 2008) that stainless steels, especially the ASS, are promising candidates for vehicle construction, and that they can be used to replace carbon steels in vehicle construction, especially in crash-relevant components such as door pillars (Schuberth et al., 2008). Among the ASS, the low-carbon grades, such as 316L and 304L, attract greater attention due to their excellent weldability. The low carbon content is beneficial in reducing the formation of chromium carbides in the grain boundaries of the HAZ. The chromium carbides are harmful to the integrity of welded ASS because they promote intergranular corrosion (Kianersi et al., 2014b).

With the growing application of Mg alloys and ASSs in the transportation industry, it is necessary to develop reliable and efficient means of joining them together. RSW is the most commonly used sheets joining process. The process is efficient, inexpensive, highly productive, reliable, easy to operate and automate, and therefore an ideal joining process for mass production (Cukovic et al., 2014; Eshraghi et al., 2014; Florea et al., 2013; Hassanifard & Feyzi, 2015). There are approximately 5000 spot welds in a typical car body (Florea et al., 2013; Hamidinejad et al., 2012) and more than 10, 000 in a railroad passenger vehicle (Fan et al., 2016).

However, it is difficult to join Mg alloys to steel by conventional RSW due to large differences in physical and metallurgical properties between them (Manladan et al., 2017b). Because of the numerous advantages of RSW mentioned above and the paramount industrial importance of Mg alloys and ASSs, it is extremely important to develop reliable RSW techniques that can join them together. In the present research, different techniques, namely, resistance spot weld bonding (RSWB), resistance element welding (REW), and resistance element weld bonding (REWB) are employed to join Mg alloy to ASS, and the microstructural evolution and mechanical properties of the joints are discussed and compared.

RSWB is an advanced hybrid joining technology which combines the advantages of RSW and adhesive bonding(Fujii et al., 2016; Marques et al., 2016; Tao et al., 2014). In this technique, structural adhesives are applied on the surface of the sheets, followed by RSW and then curing at a suitable temperature for a suitable period of time. Although RSWB has been applied to join Mg alloy to zinc-coated steel (Xu et al., 2012), the technique has not yet been applied to join any Mg alloy/stainless steel combinations.

REW is an innovative joining technology that combines both thermal (RSW) and mechanical (rivet) joining principles. It was recently developed by Volkswagen AG to address the challenges of joining Al alloys to steels. In this technique, a technological hole is punched in the Al alloy, and an auxiliary element (a steel rivet) is inserted into the hole. Subsequently, RSW is conducted on the rivet/steel. In addition to enhancing metallurgical compatibility, the technique requires the application of relatively lower welding current, as it involves welding steel to steel (Ling et al., 2016; Qiu et al., 2015). It has so far only been used to join Al alloy to steel (Ling et al., 2016; Meschut et al., 2014a; Meschut et al., 2014b; Qiu et al., 2015) and steel to LITECOR® (Holtschke & Jüttner, 2016). However, to realize the full potentials of this technique, it needs to be studied extensively and applied to a wide range of light alloy/steel combinations. Finally, REWB combines REW and adhesive bonding.

1.1 Problem statement

The large differences between the physical and metallurgical properties of Mg alloys and steel pose a huge challenge during welding. For example, the melting point of Mg is 630 ^{o}C and that of Fe is 1450 ^{o}C, suggesting that they cannot be melted at the same time. The boiling point of Mg is about 1091^{o}C, which implies that the Mg will vaporize when it comes into contact with molten steel. This problem is compounded by the metallurgical incompatibility between them; the two materials are immiscible and, according to the Mg-Fe phase diagram, no intermediate phases are formed between them (Li et al., 2013).

The heat generation and dissipation is RSW is based on the electrical resistivity and thermal conductivity of the materials being welded. Steel has about three times the bulk resistance of Mg and about half its thermal conductivity. Thus, more heat would be generated on the steel side than on the Mg side, and more heat would be dissipated on the Mg side than on the steel side. This would cause the steel to melt and the Mg to evaporate, forming pores in the weld nugget. These factors collectively pose huge challenges in

RSW of Mg alloy to steel. Because of these challenges, limited work has so far been published on RSW of Mg alloy to steels, and most of the work focused on Mg alloys/zinc-coated steels (Feng et al., 2016b; Liu et al., 2013; Liu et al., 2010b; Xu et al., 2012). The zinc-coating on the steel was found to play a vital role in the joining. The RSW of Mg alloys to stainless steels is even more challenging because of the absence of any zinc-coating. To date, no work has been reported on joining Mg alloy to ASS by using any RSW technique, despite their paramount industrial importance.

1.2 Research objectives

The aim of the present research is to produce Mg alloy/ASS joints with good mechanical properties using different RSW techniques and to understand the microstructural evolution and joining mechanism thereof. The specific objectives of this research are as follows:

1. To evaluate the resistance spot weldability of Mg alloy/ASS dissimilar materials in terms of microstructure, peak load, energy absorption capability, and failure mode
2. To evaluate the phase transformations, microstructural evolution, and mechanical performance of Mg alloy/ASS joints produced by REW technique
3. To evaluate the effect of adding structural adhesive during RSW and REW of Mg alloy/ASS on the microstructure and mechanical properties of the joints
4. To compare the mechanical performance of Mg alloy/ASS joints produced by different RSW techniques: RSW, AB, RSWB, REW, and REWB

1.3 Significance of the study

The present study is of great importance to both researchers and vehicle manufacturers. The major benefits that could be derived include:

1. This study will help researchers and the welding engineers to better understand the mechanisms involved in welding Mg alloys to stainless steels.
2. The results of this work could be used by welding engineers to design Mg alloy/ASS spot welded and weld-bonded joints with excellent mechanical properties
3. This research could serve as a basis for the transportation industry to consider the possibility of incorporating REW technique in their production lines for joining Mg alloy/steel components

1.4 Thesis structure

This thesis consists of five chapters. In Chapter 2, the fundamentals of RSW are presented, and the available literature on RSW of Mg alloys, RSW of ASSs, and RSW of Mg alloy/steels are reviewed, with focus on structure, properties, and performance relationships. The literature on RSWB of Mg alloys and REW is also reviewed.

The materials, joining processes, and microstructural characterization and mechanical testing techniques used in this work are presented in Chapter 3.

In Chapter 4, the results obtained are presented and discussed, in terms of macrostructure and microstructure of the joints, interface characteristics, hardness variation across the joint, and tensile –shear performance. The microstructural evolution and mechanical performance of the joints produced by RSW, AB, RSWB, REW, and REWB techniques are analyzed and compared.

Finally, in Chapter 5, the conclusions drawn from this work are listed and recommendations for future work are presented.

CHAPTER 2: LITERATURE REVIEW

2.1 Fundamentals of RSW

The stages involved in a typical RSW operation are illustrated in Figure 2.1. In this operation, two or more similar or dissimilar overlapping metal sheets are placed between two water-cooled electrodes (stage 1). Pressure (F) is then applied on the electrodes to clamp the workpieces together and produce an intimate contact between them (stage 2). Electrical current (I) is then supplied to the workpieces via the electrodes for a controlled period of time (stage 3). Due to resistance of the sheets to the flow of a localized electrical current, heat is generated and a molten nugget is produced at the faying interface (stage 3). The current is then switched off, while maintaining the electrode pressure, as the nugget solidifies (stage 4). The cooling is achieved by heat conduction via the two water-cooled electrodes, and also radially outwards through the sheets (Charde et al., 2014; Liu et al., 2010a; Qiu et al., 2009; Wei et al., 2013). Finally, the electrode pressure is removed to complete the process (stage 5).

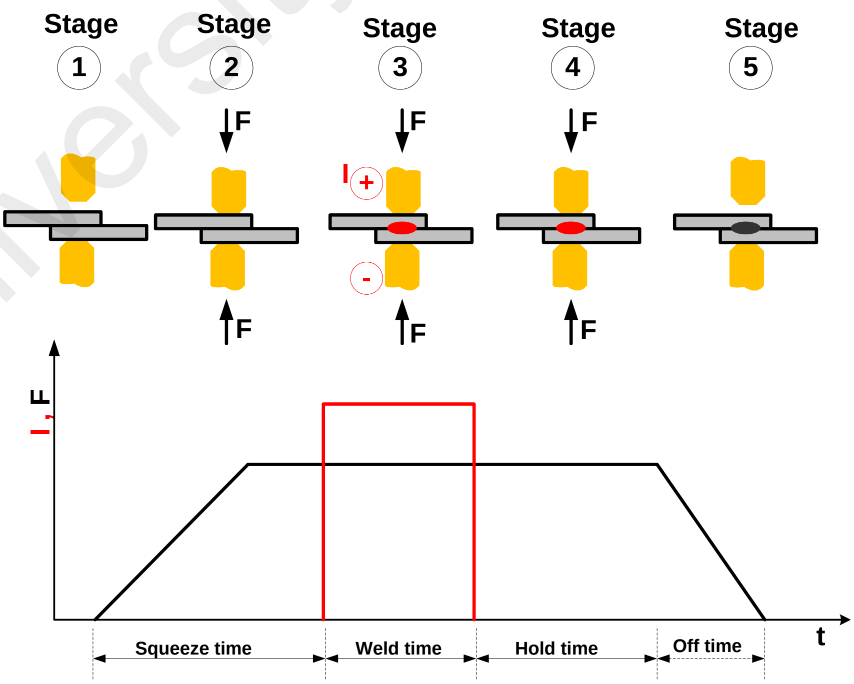

Figure 2.1: Schematic illustration of a typical RSW operation

Referring to Figure 2.1, the following should be noted (RWMA, 2003):

- Squeeze time is the time taken for the two electrodes to close and exert pressure on the work pieces
- Welding time is the duration of the application of welding current
- Holding time is the time allowed for the nugget to solidify after switching off the welding current
- Off time is the time taken for the electrodes to separate so that the weldment can be removed

The heat generation in RSW is based on Joule's law, which can be expressed as follows (Pouranvari & Marashi, 2013):

$$Q = I^2Rt \tag{2.1}$$

where Q is heat input in joules, I is the current in amperes, R is the resistance in ohms and t is the time in seconds. Therefore, the amount of heat generated depends on three factors: the current, the resistance, and the duration of the welding current.

As shown in Figure 2.2, two types of resistances exist in RSW processes, namely, bulk resistance (R3 and R5) and contact resistance, which is found at the electrode/sheet interfaces (R2 and R6) and at the faying (sheet/sheet) interface (R4) (Zhang & Senkara, 2011). In addition to these, the resistance of the upper and lower electrodes, R1 and R7, respectively, also contribute to the total resistance, which is the sum of all the resistances (R1 +R2+R3+R4+R5+R6+R7) (Williams & Parker, 2004). Of all these resistances, R4 is the most significant since the nugget formation initiates at the faying interface. If it is too low, there will be insufficient heat generation to achieve nugget formation. On the other hand, if it is too high, there will be excessive heat generation (Aslanlar et al., 2008; Manladan et al., 2017a; Williams & Parker, 2004).

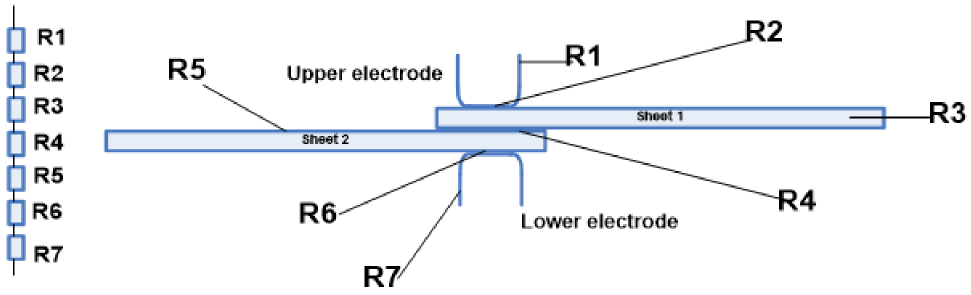

Figure 2.2 : Illustration of the electrical resistances in a sheet stack-up during RSW

The bulk resistance is sensitive to temperature and independent of pressure while the contact resistance is highly sensitive to pressure distribution, temperature, surface condition, and material characteristics. Generally, increasing the electrode force increases the actual metal-to-metal contact, thus decreasing the contact resistance (Liu et al., 2010a; Qiu et al., 2010; Zhang & Senkara, 2011). The presence of dirt, oil, coatings, and other foreign substances could also affect the contact resistance (Zhang & Senkara, 2011).

2.2 RSW of Mg alloys

2.2.1 Surface preparation for RSW of Mg alloys

To prevent corrosion, Mg alloys are normally protected using oil coating, acid pickled surface or chromate conversion coating (Liu, 2010; RWMA, 2003). This could lead to welded surfaces contamination, electrodes fouling, flashing, blowholes, and porosity in the welds. For good quality welds, the surface of Mg alloys has to be cleaned. The cleaning would reduce variations in contact resistance and reduce the heating between the electrodes and Mg alloys and hence produce better quality joints (RWMA, 2003). Cleaning the surface of Mg alloys with 2.5% (w/v) chromic acid (2.5g CrO_3 + 100 ml H_2O) was found to be effective in this regard (Liu et al., 2009; Zhou et al., 2010). For example, Zhou et al. (2010) observed that the surface of as-received AZ31B Mg alloy consisted of MgO, $Mg(OH)_2$, and $MgCO_3$. The surface exhibited variations in contact resistance, with an average contact resistance of 78 mΩ. Cleaning the surface with 2.5% (w/v) chromic acid produced more uniform contact resistance and reduced the average contact resistance to 3 mΩ (Zhou et al., 2010). During RSW, due to the high contact resistance of the as-received samples, rapid heat generation resulted in expulsion and poor quality joint. For the chromic acid-cleaned samples, no expulsion was observed even at higher welding current. Moreover, these samples produced much less damage on the electrode tip faces (Liu et al., 2009; Zhou et al., 2010). Consequently, 2.5% (w/v) chromic acid is commonly used to clean the surfaces of Mg alloys prior to RSW (Behravesh et al., 2011; Niknejad et al., 2013; Xiao et al., 2012; Xu et al., 2013). Abrasive papers have also been used to effectively clean the surface oxides (Feng et al., 2016b).

2.2.2 Nugget formation in RSW of Mg alloys

The nugget formation and growth during RSW of Mg alloys could be divided into three stages: incubation, growth, and stabilization (Wang et al., 2007). In the incubation stage, which is relatively short, usually less than 1 cycle, the nugget begins to form due to the melting of the metal. In the growth stage, which occurs in the following 2-4 cycles, the nugget grows rapidly but the growth rate decreases with time. This is due to the reduction in current density and heating rate caused by the increase in the contact area between the electrode and work piece. Finally, the nugget growth achieves stabilization after approximately 4 cycles. The duration of the incubation stage for Mg alloys was found to be similar to that of aluminum and much smaller than that of steel (Feng et al., 2006; Wang et al., 2007).

2.2.3 Microstructural evolution

The microstructural evolution is controlled by a combination of the prevailing thermal condition at the solid/liquid interface and the rate of growth of crystals, which is directly related to the thermal gradient in the weld (Wang et al., 2006). Due to the low volumetric heat capacity, good thermal conductivity, and low melting point of Mg alloys, the cooling rate of the weld is so high that the weld solidifies under non-equilibrium conditions (Babu et al., 2012).

Behravesh et al. (2011) characterized the microstructure of AZ31-H24 Mg alloy resistance spot welds and four different zones were identified, as shown in Figure 2. 3, namely, the base metal (BM), heat affected zone (HAZ), partially melted zone (PMZ), and fusion zone (FZ).

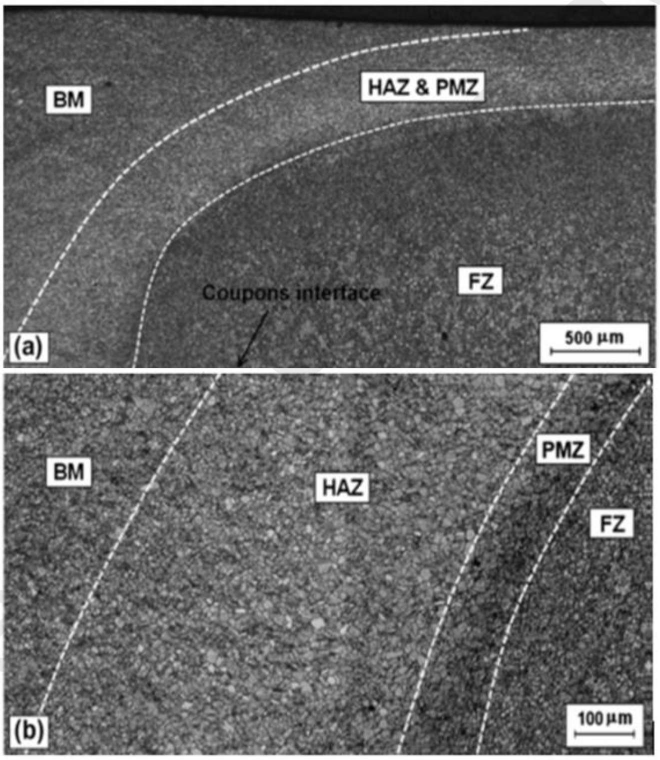

Figure 2.3: Different zones in AZ31B Mg alloy resistance spot welds (a) low magnification and (b) high magnification (Behravesh et al., 2011)

The FZ usually consists of two different zones, i.e. columnar dendritic zone (CDZ) and equiaxed dendritic zone (EDZ). The CDZ is found adjacent to the fusion line, with crystals nucleating and growing epitaxially from the unmelted BM while the EDZ is found at the center of the nugget (Niknejad et al., 2014; Niknejad et al., 2013; Xiao et al., 2011; Xiao et al., 2012; Xiao et al., 2010; Yao et al., 2014). The columnar-to-equiaxed transition (CET) occurs when the movement of the columnar front is blocked by enough equiaxed grains formed in the liquid ahead of the columnar front (Liu et al., 2010a). Compared to the columnar dendritic structure, the equiaxed grains are finer, have more isotropic structure, less segregation of alloying elements, and better mechanical properties. The columnar dendritic structure affects the mechanical properties of the weld and is therefore undesirable. As such, it is crucial to promote the formation of equiaxed grains for improved mechanical properties (Liu et al., 2010c; Xiao et al., 2012; Xiao et al., 2010).

Liu et al. (2010c) reported that the size of pre-existing second phase particles in the base metal affects CET transition. It was shown that AZ31B Mg alloy (SA), which contained both submicron sized and coarse Al_8Mn_5 particles had short, fine, and narrow CDZ and more developed equiaxed grains in the FZ. On the other hand, AZ31B Mg alloy (SB), which contained only submicron size Al_8Mn_5 particles had a well-developed columnar dendrite region, long primary arms, coarse grain size. The addition of 10 μm-long Mn particles to SA, which did not contain coarse second phase particles, effectively suppressed the CDZ and promoted the formation of equiaxed grains (Xiao et al., 2010). In another study, it was shown that increased welding current led to a decreased CDZ width for both SA and SB. The CDZ nearly vanished when the welding current was higher than a certain critical value, which was about 24 kA and 28kA for SA and SB, respectively. It was also shown that that the addition of titanium powder, with particles size less than 20μm, to the FZ during RSW of AZ31-H24 Mg alloy significantly suppressed the CDZ, as shown in Figure 2.4. The titanium particles served as inoculants to enhance the nucleation of α-Mg grains and the formation of equiaxed dendritic structure. In addition to suppressing the CDZ, the grains in the EDZ were effectively refined by the addition of titanium. The average diameter of the flower-like grains in the

EDZ with and without the addition of titanium was found to be approximately 20 µm and 65 µm, respectively. This led to significant improvement in mechanical properties (Xiao et al., 2012).

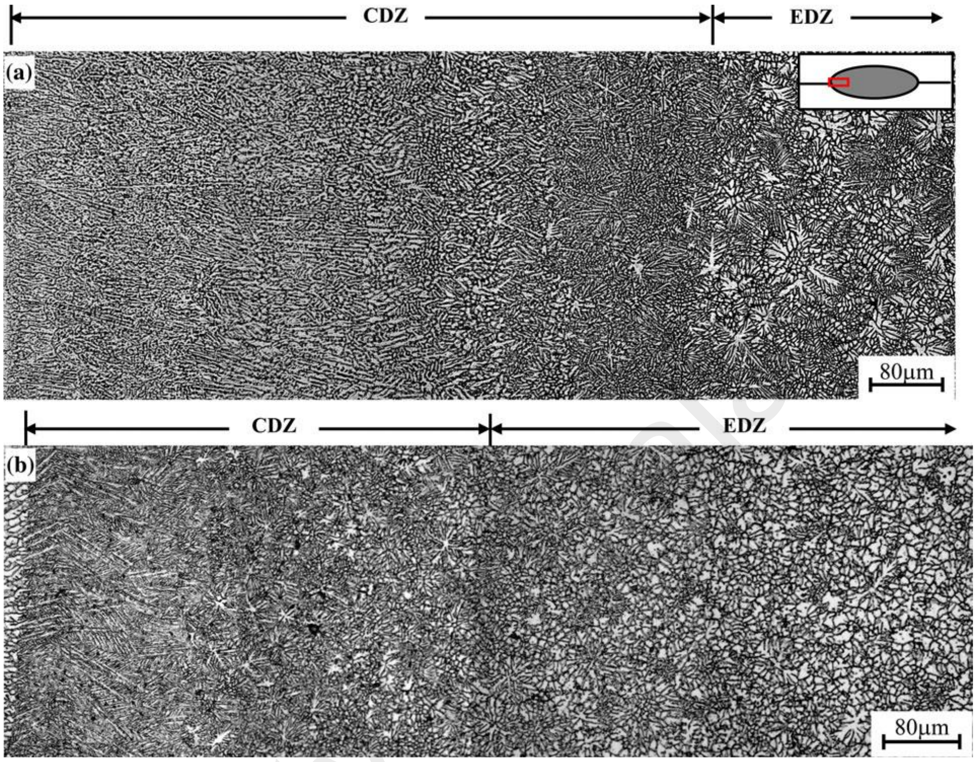

Figure 2.4 : Microstructure of the FZ AZ31 alloy welded (a) without and (b) with an addition of Ti (Xiao et al., 2012)

Generally, for resistance spot welds of AZ series Mg alloys, the grain size refinement and CET were found to improve with increase in aluminum content. Niknejad et al. (2014) investigated the microstructural evolution during RSW AZ31, AZ61, and AZ80 Mg alloys. It was observed that the higher aluminum content in AZ61 and especially AZ80 enhanced CET and grain size refinement. The average length of the columnar dendrite zone was found to be 320 µm, 170 µm, and 80 µm for AZ31, AZ61, and AZ80 Mg alloys, respectively. The size of the dendrites also decreased from AZ31 to AZ61 and AZ80. The diameter of the flowerlike dendritic grains was found to be 31 µm, 20 µ m, and 16 µm for AZ31, AZ61, and AZ80 welds, respectively.

Furthermore, Yao et al. (2014) have shown that RSW of AZ31B Mg alloys under the influence of electromagnetic stirring also influences the microstructure of the FZ. Two permanent magnets, which were co-axially mounted on the electrode arms of the RSW machine with opposite polarities, were used as the source of electromagnetic force. The results showed that RSW with electromagnetic stirring effect (EMS-RSW) promoted early CET and produced finer grains in HAZ, CDZ and EDZ compared to conventional RSW process, as shown in Figure 2.5. The high speed movement of the molten metal driven by the circumferential external magnetic force facilitated the formation of equiaxed grains by breaking the growing dendrites during the primary crystallization process. In addition, the EMS reduced the temperature gradient and degree of constitutional supercooling. It also resulted in balanced crystallization temperature, uniform diffusion, and refined the microstructure.

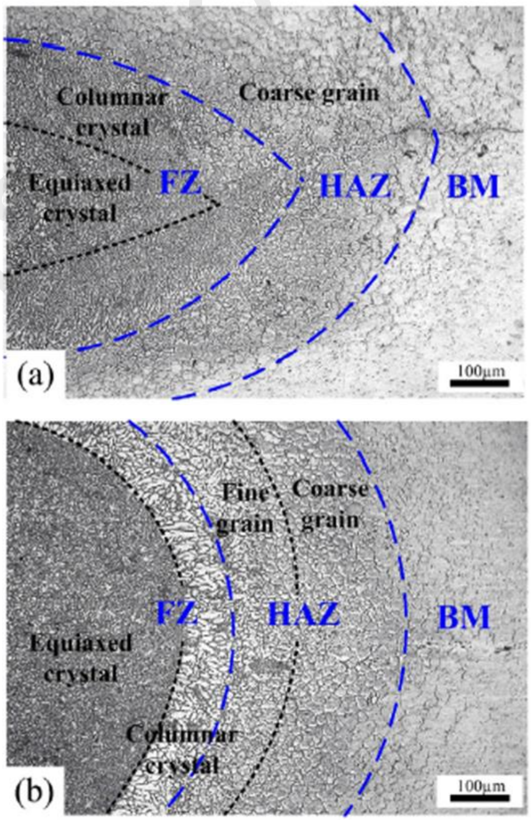

Figure 2.5: Microstructure of AZ31B Mg alloy weld produced by (a) Conventional RSW (b) RSW with electromagnetic stirring (Yao et al., 2014)

The HAZ of resistance spot welds of Mg alloys is characterized by recrystallization and grain growth (Babu et al., 2012; Behravesh et al., 2011; Niknejad et al., 2014). For instance, a grain size gradient (10-6μm), decreasing towards the BM, was observed in the HAZ of AZ31B-H24 Mg alloy spot welds. This was because in the HAZ, the regions which are closer to the BM experienced lower annealing temperature and time than regions which are closer to the PMZ. Moreover, much more higher twin band density was found in the HAZ than in the BM (Behravesh et al., 2011). Babu et al. (2012) reported that grain boundary melting occurred in the HAZ of AZ31 immediately adjacent to the nugget, and the grain boundaries became coarse compared to the unaffected base metal.

$Mg_{17}Al_{12}$ intermetallic compounds (IMC) were observed in the grain boundaries of PMZ of AZ31B-H24 Mg alloy RSW joint. The peak temperature attained in the PMZ, which is located around the nugget, is between the solidus and liquidus temperatures of the BM. As a result, grain boundary liquation might have occurred due to the lower melting point and higher aluminum content of the grain boundaries, thus promoting the formation of $Mg_{17}Al_{12}$ IMCs (Behravesh et al., 2011). Also, β-$Mg_{17}(Al,Zn)_{12}$ phases were observed in grain the boundaries of the HAZ of AZ31, AZ61, and AZ80 Mg alloys. The quantity of these phases was higher in AZ80 and AZ61 than in AZ31, due to their higher aluminum contents. Different mechanisms were proposed for the formation of these β-phases, depending on the alloy type. For AZ31 alloy, even though minute traces of the β-phase were found in microstructure of the BM, formation of the β-phases would suggest that liquation occurred in grain boundaries of the HAZ. For AZ61 and AZ80 alloys, the β-phases pre-existed in grain boundaries of the BM and they reacted with the surrounding α-matrix to form a liquid eutectic layer at the grain boundaries due to rapid heating at the HAZ (Niknejad et al., 2014). The existence of these particles was detrimental to the strength of the welds, especially in AZ61 and AZ80 alloys, which failed in the HAZ, along the FZ due to preferential micro-cracking at the interfaces of the β-phases and Mg matrix during tensile shear testing. Post-weld solutionizing heat treatment significantly reduced the quantity of these particles, and thus improved the strength of the joints (Niknejad et al., 2014; Niknejad et al., 2013).

2.2.4 Mechanical properties

2.2.4.1 Hardness

Generally, little variation in hardness has been reported across the BM, HAZ, and FZ of Mg alloy resistance spot welds (Behravesh et al., 2011; Niknejad et al., 2013). For AZ31B-H24 Mg alloy, the hardness in the weld area was found to be almost the same with that of the BM. This was due to the occurrence of two opposite phenomena which counteract each other, leading to uniform hardness distribution. The increase in the grain/dendrite size from the BM to the FZ decreased the hardness. On the other hand, IMCs present in the PMZ and FZ and twin bands in the HAZ increased the hardness. Even under cyclic loading, AZ31B-H24 Mg alloy did not show appreciable hardness variation across the BM, HAZ, and FZ, suggesting that both the BM and weld region did not undergo cyclic hardening (Behravesh et al., 2011). Similarly, a relatively uniform hardness distribution was observed across the BM, HAZ, and FZ of resistance spot welded AZ80 Mg alloy. After postweld heat treatment there was a reduction in hardness across these zones. This reduction in hardness was attributed to partial dissolution of β-$Mg_{17}Al_{12}$ phase and grain growth (Niknejad et al., 2013). Liu et al. (2010c) observed little hardness variation across the BM, HAZ, and FZ of resistance spot welded AZ31 (SA) and AZ31(SB) Mg alloys, with the BM having the highest value of 70 HV, as shown in Figure 2.6. This was attributed to the fact that the welding process resulted in the reduction of pre-existing deformed structures such as solution strengthening, dislocation density, and defects in the BM. The CDZ exhibited an average hardness value of about 69 HV in AZ31 (SA) and 60 HV in AZ31 (SB), whereas the average hardness value of the EDZ was 67 HV in AZ31 (SA) and 61 HV in AZ31 (SB) (Liu et al., 2010c).

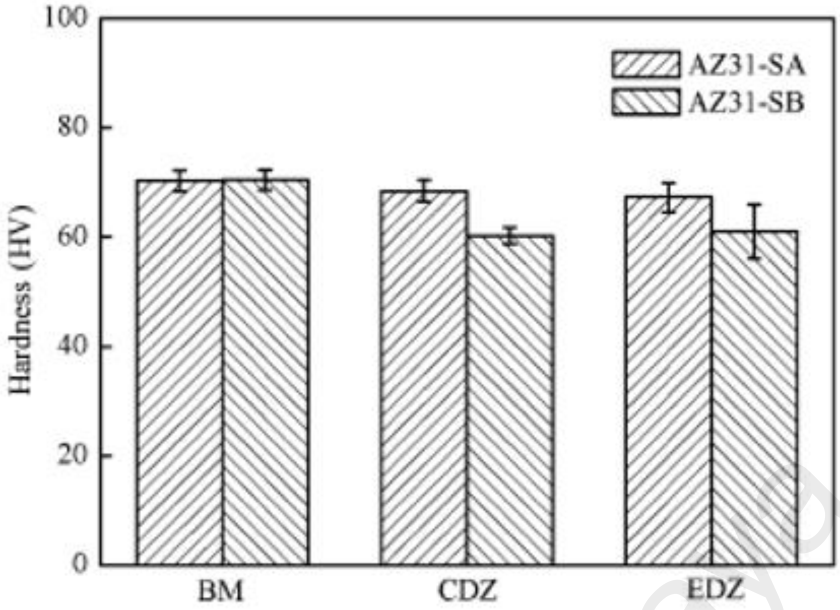

Figure 2.6 : Hardness profile across welds of two AZ31 alloys (Liu et al., 2010c)

Furthermore, Yao et al. (2014) reported an average hardness value of approximately 64, 55, 63, and 58 HV for the BM, HAZ, CDZ, and EDZ of AZ31 Mg alloy, respectively. Under the influence of EMS, the hardness of each zone increased due to grain size refinement. The hardness ratio of fusion zone to pullout failure location (usually is HAZ) was found to be 1.28 for EMS-RSW and 1.03 for traditional RSW, implying that the EMS-RSW joint is more likely to experience pullout failure. On the contrary, for continuous cast and rolled AZ31 Mg alloy resistance spot weld, Babu et al. (2012) observed a manifest hardness reduction in the weld nugget and HAZ compared to the BM, as shown in Figure 2.7. The reduction in hardness in the weld nugget and HAZ were due dendritic microstructure and coarse grains, respectively. The high hardness of the BM was due to fine grain size and cold working (Babu et al., 2012).

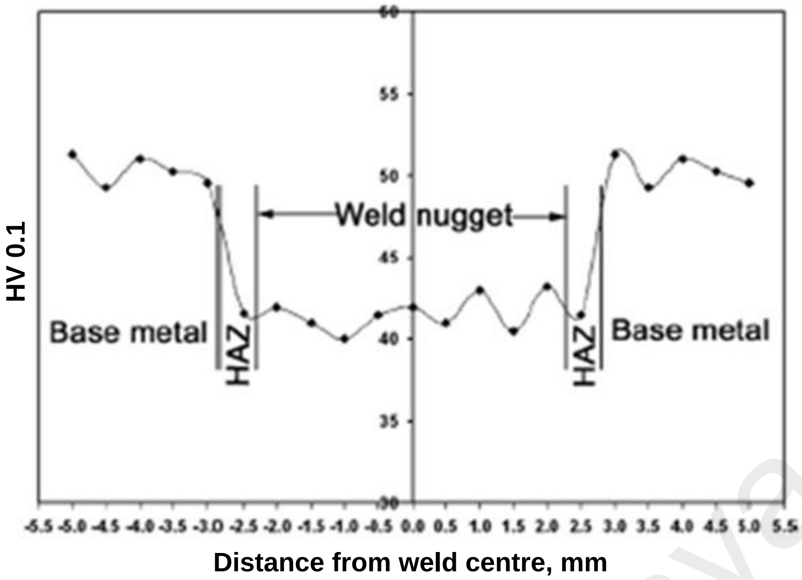

Figure 2.7: Hardness profiles across resistance spot welds in the as-welded condition (Babu et al., 2012)

2.2.4.2 Tensile shear properties and failure mode

The mechanical performance of spot welds is normally considered under quasi-static and dynamic loading conditions. Tensile-shear (TS), cross-tension (CT), and coach peel (CP) tests are examples of tests conducted under quasi-static loading conditions. Impact and fatigue tests are examples of tests conducted under dynamic loading conditions (Pouranvari & Marashi, 2013). Due to simplicity in preparing samples for TS test (Babu et al., 2012) coupled with the fact that many welded joints are designed to bear tensile-shear loads (Marashi et al., 2008b), TS test is widely used to determine the strength of resistance spot welds (Babu et al., 2012). In this test, load bearing capacity (peak load) and failure energy are the two most important parameters used to describe the performance of the joint (Pouranvari & Marashi, 2013). Three types of failure modes commonly occur during TS test of spot welds, i.e., interfacial (IF), partial interfacial (PIF), and pull out (PO) failure modes (Pouranvari & Marashi, 2013). In IF mode, cracking occurs through the nugget centerline, separating the sheets apart. It is accompanied by little plastic deformation. In PIF, a fraction of the weld nugget is removed. The crack first propagates in the weld nugget, then redirects perpendicularly to the centerline towards one of the sheets (Pouranvari & Marashi, 2013; Yao et al., 2014). PO mode occurs by complete or partial withdrawal of the nugget from one sheet. In this mode, crack does not propagate through the nugget. It is accompanied by more plastic deformation, thus leading to higher energy absorption and peak load and is, therefore, the most desirable mode (Babu et al., 2012; Pouranvari & Marashi, 2013). These failure modes are schematically illustrated in Figure 2.8.

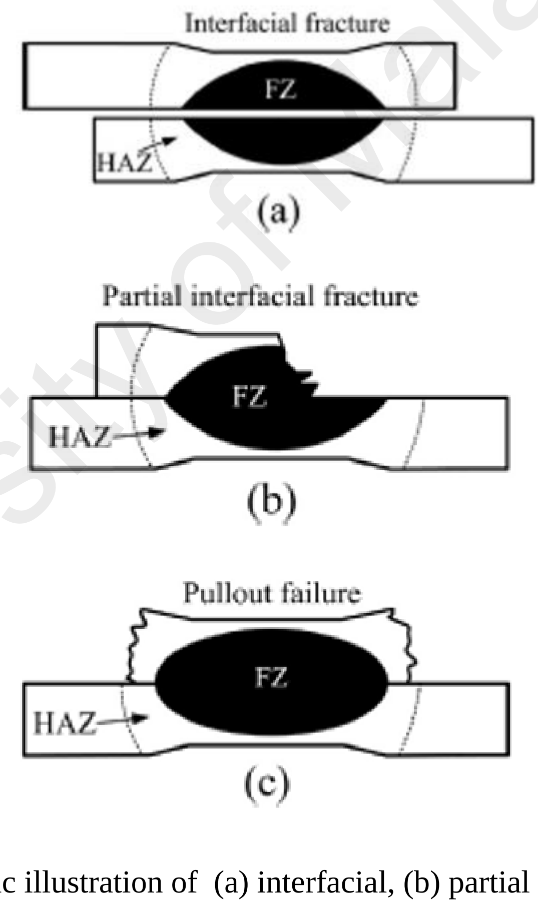

Figure 2.8: Schematic illustration of (a) interfacial, (b) partial interfacial, and (c) pullout failure modes (Yao et al., 2014)

Weld nugget size is the most important parameter determining the mechanical behavior of the spot welds. Quality and strength of the spot welds are defined by shape and size of weld nuggets (Moshayedi & Sattari-Far, 2012). Generally, the nugget size is considered as the main criterion that determines the mechanical performance of the welds (Feng et al., 2015; Karimi et al., 2015; Li et al., 2014; Li et al., 2015a; Pereira et al., 2010; Senkara et al., 2004). It has also been shown that for a stack of sheets of same base material, the thinnest sheet thickness, known as governing metal thickness (GMT), generally has the lowest tearing resistance and thus dictates the joint strength (Han et al., 2011a; Han et al., 2011b; Han et al., 2010). Radakovic and Tumuluru (2008) derived the following equations to predict PO and IF loads, F_{PO} and F_{IF}, respectively (Radakovic & Tumuluru, 2008):

$$F_{PO} = k_{PO} \,.\, \sigma_{UT} . d . t \qquad (2.2)$$

$$F_{IF} = k_{IF} . \sigma_{UT} . d^2 \qquad (2.3)$$

where k_{PO} (~2.2) and k_{IF} (~0.6) are constants, σ_{UT} is the ultimate tensile shear strength of the base material, d is nugget diameter, t is the sheet thickness.

Based on equations (2.2) and (2.3), PO failure load strongly depends on the nugget diameter and sheet thickness, while IF load depends primarily on the nugget diameter.

IF mode is common in Mg alloys spot welds (Babu et al., 2012; Behravesh et al., 2011), partly because hardness, and therefore strength, in the FZ is comparable or less than the BM (Behravesh et al., 2011). For example, Behravesh et al. (2011) conducted TS test on resistance spot welded AZ31B-H24 alloys. The samples failed predominantly in IF mode. An average ultimate tensile shear load (UTSL) of 6.67kN was obtained. Similarly, Babu et al. (2012) carried out TS test on AZ31 Mg alloy resistance spot welds at constant nugget diameter of $3.5\sqrt{t}$ (t = sheet thickness, 3 mm) for all samples. All samples failed in IF mode, with an average peak load of 4.7 kN. Xiao et al. (2012) studied the effect of titanium addition on the mechanical properties of AZ31 Mg alloy resistance spot welds. They found that the addition of titanium increased both the UTSL and displacement of the welds. For example, at a welding current of 26kA, the addition of titanium increased the UTSL of the joint by 38%, from 4.076kN to 5.169kN, while the displacement increased by 28%, from 1.09 to 1.40. For AZ80 Mg alloy, an average UTSL of 4.69kN was obtained with PO failure mode. Post weld solution heat treatment improved the strength to 6.63kN and changed the failure mode to through thickness (Niknejad et al., 2013). A comparison of the mechanical performance of AZ31, AZ61, and AZ80 Mg alloys resistance spot welds under the same conditions during TS test showed that AZ31 failed in IF mode while AZ61 and AZ80 alloys failed in nugget PO failure. After post weld solution heat treatment, the failure mode in AZ31 welds remained unchanged while that of AZ61 and AZ80 changed from PO mode to through-thickness. Moreover, the heat treatment increased the average strength of joints of AZ31, AZ61, and AZ80 by 3.1%, 11.7% and 37.2% respectively, as shown in Figure2.9.

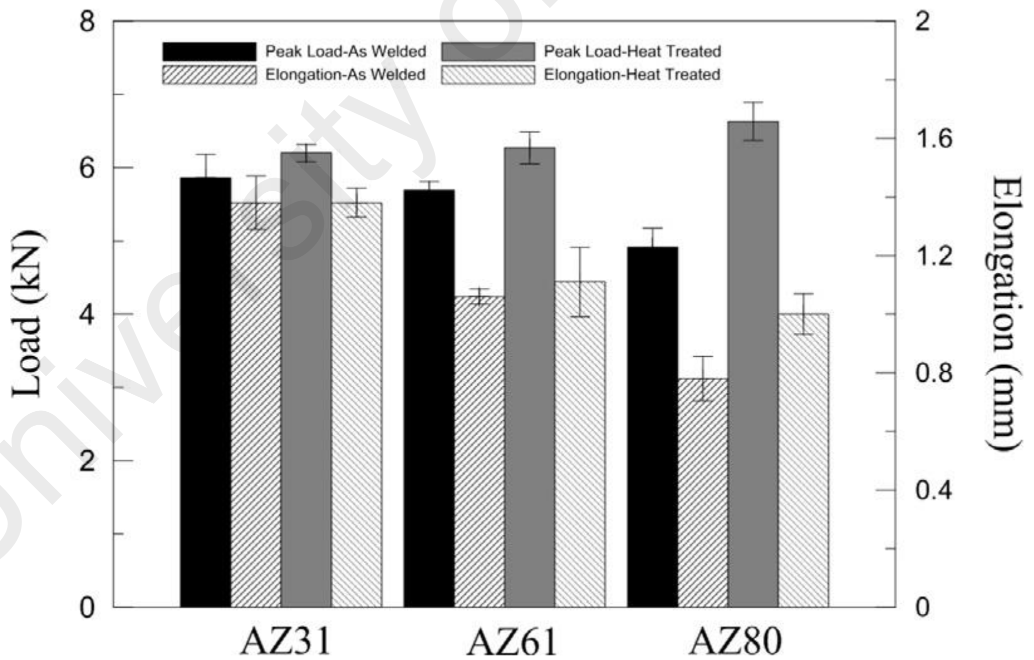

Figure 2.9: Peak load and elongation (at the peak load) of Mg alloy resistance spot welds in as-welded and heat treated conditions (Niknejad et al., 2014)

Recently, Yao et al. (2014) studied the effect of electromagnetic stirring on the properties of AZ31B Mg alloy resistance spot welds. The results showed that samples produced by EMS-RSW had larger nugget diameter, higher tensile shear force and energy absorption capacity, and thus higher probability of pullout failure mode than those produced by conventional RSW, at all welding currents.

2.2.4.3 Fatigue Behavior

Spot welds act as sites for stress concentration and are therefore susceptible to fatigue failure (Behravesh et al., 2011). Fatigue is the most critical failure mode of spot-welded and weld-bonded joints in automobiles (Pereira et al., 2014). As such a detailed understanding of the fatigue behavior of spot welded joints is required to ensure the integrity, durability, and safety of welded structures (Patel et al., 2014; Xiao et al., 2011). However, research on the fatigue behavior of Mg alloys spot welds is very limited.

Fatigue tests were carried out to investigate the behavior of resistance spot welds of AZ31B-H24 Mg alloys in tensile–shear configuration. The results showed that three different failure modes occurred, i.e. coupon, IF and PIF failure modes, with coupon failure being the most dominant (Behravesh et al., 2011; Behravesh et al., 2014). The coupon failure occurred in the intermediate and high cycle fatigue regimes, at lower loads. Since the crack did not propagate through the nugget in this failure mode, the fatigue life is independent of the nugget strength. It depends on the level of cyclic loading and coupon dimensions. The IF mode occurred when very high cyclic load was applied. Since crack propagated through the nugget in this failure mode, the fatigue strength depends largely on the nugget size and strength. On the other hand, PIF mode rarely occurs and was only observed between very low and low cycle regimes (for fatigue life between 3 $x10^3$ and 10^4 cycles) (Behravesh et al., 2011; Behravesh et al., 2014). The nugget size was found to have strong influence on fatigue resistance in the low cycle regime. This influence decreased gradually over fatigue life and eventually the fatigue resistance becomes almost independent of nugget size above 10^5 cycles (Behravesh et al., 2011). Figure 2.10 depicts the load–life curves for AZ31B-H24 Mg alloy joints, having different configurations and nugget diameters (Table 2.1). From the load–life curves of specimens sets A, C, and E, it can be seen that enlarging the nugget size has insignificant effect on fatigue strength (in terms of load range). Also, by comparing the curves for sets A–E and set F, it can be seen that increasing the coupon width and decreasing the mean load lead to improvement of fatigue strength for LCF, and that this effect gradually decreases for HCF. Furthermore, a comparison between the curves for sets G, E, and F, shows that the fatigue strength of CT specimen is significantly lower than that of TS specimens with the same nugget size. The endurance limit for specimen sets A, C, E, F, and G is 0.34 kN, 0.44 kN, 0.48 kN, 0.72 kN, and 0.16 kN, respectively (Behravesh et al., 2014).

Table 2.1 : AZ31B-H24 Mg alloy spot-welded specimens coding and nugget diameter (Behravesh et al., 2014)

Specimen set	Configuration	Average nugget diameter (mm)
A	TS[a]	8.2 (0.7)[d]
C	TS	9.5 (0.1)
E	TS	10.4 (0.2)
F	TS-W[b]	10.4 (0.2)
G	CT[c]	10.4 (0.2)

[a] Standard size TS test specimen

[b] Wide TS test specimen

[c] Standard size CT test specimen

[d] Values in parentheses are standard deviations

The load level was also found to have an effect on the location of crack initiation. High cyclic loading resulted in crack initiation close to the nugget edge and as the cyclic load decreased, the crack initiation location was farther away from the nugget. It was also noted that under cyclic loading, two cracks initiated at opposite sides of the nugget: Primary crack, which propagated until failure occurred and secondary crack, which propagated to a certain extent but did not result in failure, as shown in Figure 2.11 (Behravesh et al., 2011).

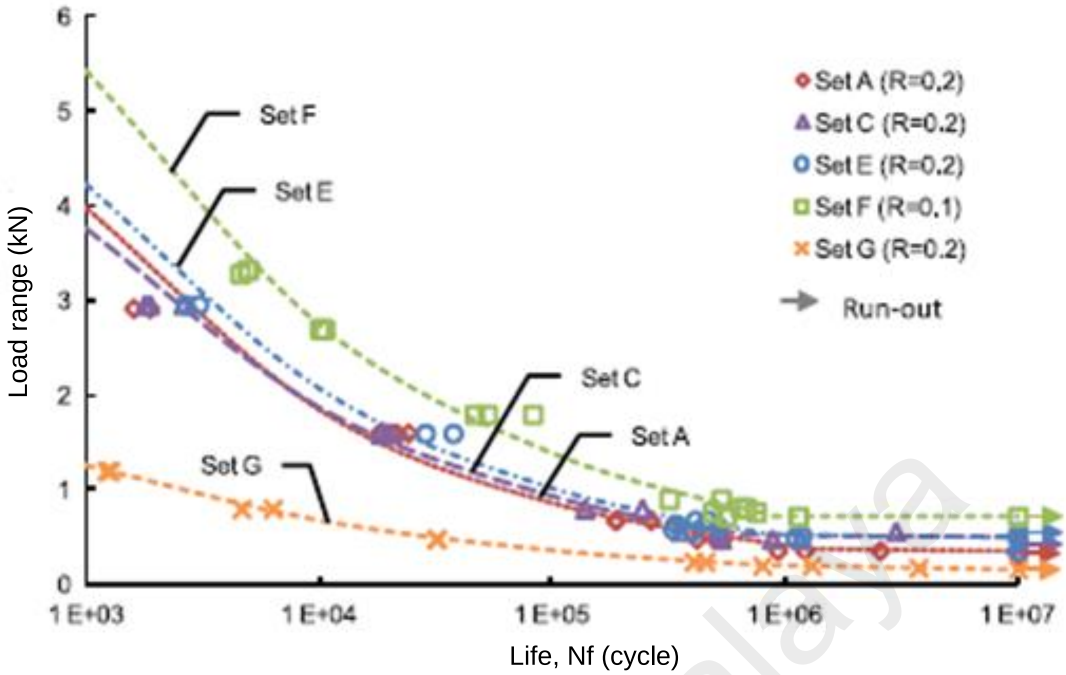

Figure 2.10: Load-life experimental data for A31B-H24 resistance spot-welded specimens (Behravesh et al., 2014)

The cyclic behavior of AZ31B Mg alloy spot-welds was studied using different specimen configurations, and compared with steel and aluminum spot-welds. It was found that the fatigue strength of Mg spot-welds was similar to aluminum but considerably less than that of steel spot welds, for the same $d/t^{\frac{1}{2}}$ ratio (Behravesh et al., 2014).

Xiao et al. (2011) studied the fatigue behavior of two different Mg alloys, AZ31B (SA) and AZ31B (SB), with similar composition but containing second-phase particles of different sizes, in the as-received material and consequently different fusion zone microstructure.

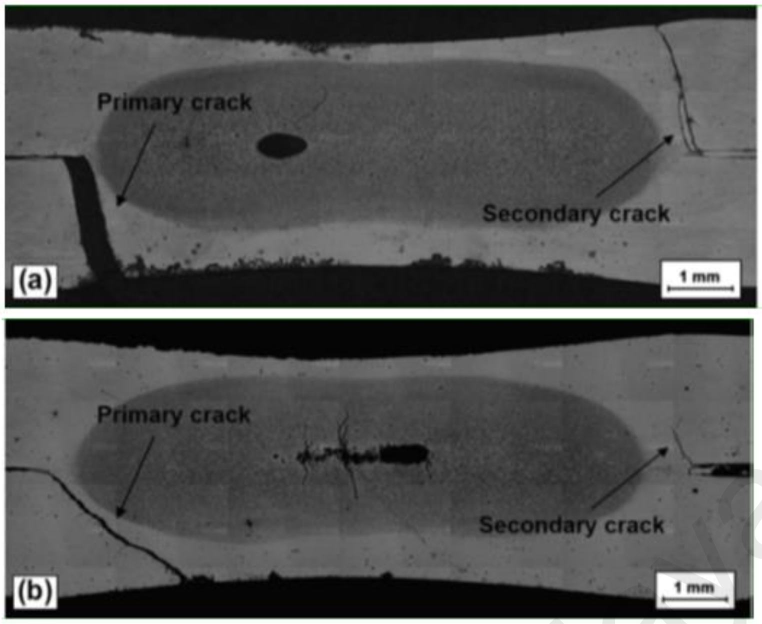

Figure 2.11: Primary and secondary cracks in AZ31B-H24 Mg alloy spot welds (a) in LCF and (b) in HCF (Behravesh et al., 2011)

When tested under identical conditions of higher cycle load range, both samples failed in IF mode. However, AZ31B Mg alloy (SA) with more refined microstructure (finer dendrite structure) had longer fatigue life than AZ31B Mg alloy (SB) welds, and thus better fatigue resistance. Figure 2.12 shows the fracture surfaces (IF mode) of SA and SB welds tested under the same cyclic load range of 3.12kN. As indicated by the arrows in Figure 2.12, typical fatigue striations are observed on both fracture surfaces, suggesting that the crack propagation was transgranular. Due to the finer dendritic structure in the fusion zone in SA welds compared to SB welds, the fatigue striations spacing for SA welds was smaller than that of SB welds, hence exhibiting slower crack propagation rate and longer fatigue life (Xiao et al., 2011). However, when the cyclic load was below 0.5kN, both SA and SB had similar fatigue lifes.

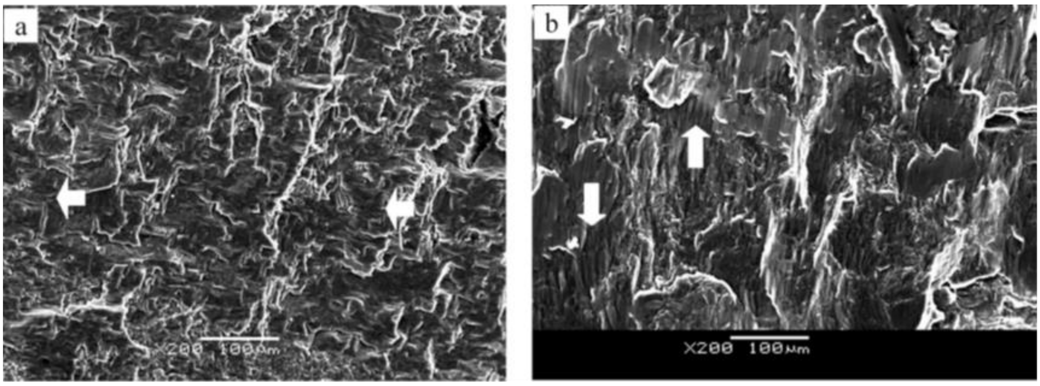

Figure 2.12 : A comparison of fatigue crack propagation zones at higher cyclic load ranges in : (a) SA and (b) SB welds (Xiao et al., 2011). Arrows indicate fatigue striations

2.3 RSW of Mg alloys with cover plates

Owing to the high thermal and electrical conductivities of Mg alloys, high electrical current is needed during RSW. However, this high current promotes electrode tip wear, blow holes, expulsion, and the need for larger-capacity machines (Qiu et al., 2009; Satonaka et al., 2012). To successfully weld Mg alloys under the condition of low welding current, Qiu et al. (2009) proposed the technique of RSW with cover plates. In this technique, the Mg alloy sheets were placed between two 1-mm-thick cover plates made of cold rolled steel. The choice of cold rolled steel was based on the need for a material with lower electrical conductivity than Mg alloy to ensure higher heat generation in the cover plate and subsequent conduction to the Mg alloy. Other major considerations were low cost and the ability of the cover plate to separate from the Mg alloy after welding (Qiu et al., 2009; Qiu et al., 2010; Shi et al., 2010). The technique proved advantageous and was able to produce joints in AZ31B Mg alloy with higher tensile shear-strength and larger nugget diameter than those produced by conventional RSW. Moreover, these joints were produced with lower welding currents, which are comparable to that for RSW of steel sheets (Qiu et al., 2009; Satonaka et al., 2012; Shi et al., 2010). For example, Shi et al. (2010) obtained a nugget diameter and tensile shear load of 9.5 mm and 4.7kN, respectively, at a welding current of 12kA by RSW with cover plates while a nugget diameter of 3mm and tensile shear load of less than 1kN were obtained by traditional RSW under the same welding conditions. Although pores were observed in the nugget of the joints produced by this technique, their formation was effectively suppressed by increasing the electrode force and extending down-sloping time (time of welding current reducing to zero) (Shi et al., 2010).

2.4 RSW of ASS

Generally, ASSs have better weldability than other grades of stainless steels. However, one major problem encountered when welding ASSs is the precipitation of Cr-rich carbide particles in the grain boundaries of the HAZ, which leads to intergranular corrosion. Two approaches are usually employed to solve this problem, namely, the use of low carbon grades and the use of rapid welding processes such as RSW (Kianersi et al., 2014a; Kianersi et al., 2014b). The main characteristics of different grades of stainless steels during RSW are listed in Table 2.2. The resistance spot weldability of a material is influenced by its physical properties. The typical physical properties of different grades of stainless steels and low carbon steels are listed in Table 2.3. It can be seen that stainless steels possess lower thermal conductivity, higher electrical resistivity, higher thermal expansion coefficient, and lower melting points than the carbon steel. Stainless steels are more susceptible to solidification cracking during welding due to their higher thermal expansion coefficient. Therefore, lower welding currents and shorter welding times should be applied during RSW of stainless steels to ensure that welds with acceptable physical attributes and mechanical performance are produced (Pouranvari et al., 2015a).

Table 2.2: Typical characteristics of stainless steels during RSW (Pouranvari et al., 2016)

Stainless steel grade	**Characteristics**
Martensitic stainless steel	• Very hard and brittle martensite formation in FZ and HAZ • Retention of undesirable delta ferrite in FZ • High susceptibility to IF with low failure energy
Ferritic stainless steel	• Significant grain growth in HAZ • Formation of martensite in grain boundaries of HAZ
Austenitic stainless steel	• Suppression of completion of ferrite–austenite post-solidification transformation due to rapid cooling rate • No corrosion sensitisation (Cr-carbide precipitation) in HAZ • High susceptibility to IF during tensile–shear loading
Duplex stainless steel	• Unbalanced microstructure in the FZ and HAZ • Higher ferrite content in the FZ compared to the BM

Table 2.3: Typical physical properties of low carbon steel and stainless steels (AWS, 1982; Pouranvari et al., 2015a)

Stainless steel grade	**Melting temperature range (°C)**	**Electrical resistivity (µΩm)**	**Thermal conductivity at 100 °C ($Wm^{-1}K^{-1}$)**	**Mean coefficient of thermal expansion 0-538 °C ($\mu m\ m^{-1}\ C^{-1}$)**
Martensitic stainless steel	1480-1530	550-720	28.7	11.6-12.1
Ferritic stainless steel	1480-1530	590-670	24.4-26.3	11.2-12.1
Austenitic stainless steel	1400-1450	690-1020	18.7-22.8	11.7-19.2
Duplex stainless steel	1430-1450	770-1000	16.2-19.0	13.3-13.7
Low carbon steel	1538	120	60	1.17

2.4.1 Nugget formation in RSW of ASS

The nugget formation during RSW of ASS has been studied using experimental investigation and finite element simulation (Moshayedi & Sattari-Far, 2012). As shown in Figure 2.13, it was found that the nugget begins to form at 5 cycles welding time and then grows rapidly in the next 3 cycles. Thereafter, the nugget growth rate decreases with further increase in welding time. This behavior has been attributed to fluctuations in heat generation at the faying interface. The decreased nugget growth rate at longer welding time is due to the increase in contact area between the sheets and the consequent reduction in current density. Moreover, the heat losses from the nugget through convection and conduction increase with longer welding times. This also leads to reduction in nugget growth rate (Moshayedi & Sattari-Far, 2012)

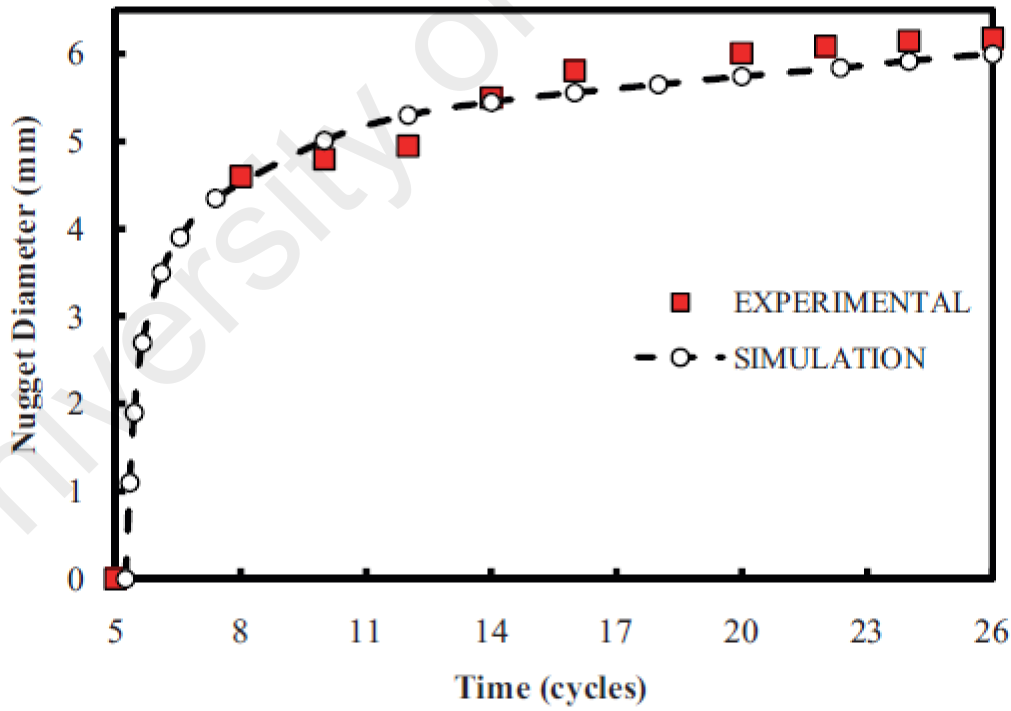

Figure 2.13: Nugget growth during RSW of 304L ASS (Moshayedi & Sattari-Far, 2012)

2.4.2 Phase transformations and hardness characteristics of ASS resistance spot welds

2.4.2.1 Phase transformations and microstructure

The phase transformations (including solidification and ferrite-austenite transformations) that occur during RSW of stainless steels are controlled by the ratio of Cr equivalent to Ni equivalent (Creq/Nieq) and the cooling rate. The cooling rates in RSW of stainless steels are generally lower than in the RSW of low carbon steels because of their lower thermal conductivity and diffusivity (Pouranvari et al., 2015a) . Nevertheless, the cooling rates encountered during RSW of stainless steels are extremely high due to the inherent high cooling rate characteristic of RSW.

Gould et al. (2006) developed an analytical model for calculating the cooling rates experienced in RSW, which is given by,

$$\frac{\partial\theta}{\partial t} = -\left(\frac{\propto\pi^2}{4\Delta x^2}\right)\left(\frac{\theta}{\theta_P}\right)\left[\theta_P - \frac{\theta}{1+\left(\frac{2}{\pi}\right)\left(\frac{k_E}{k_S}\right)\left(\frac{\Delta x}{\Delta x_E}\right)\cos\left(\frac{\pi}{2\Delta x}x\right)}\right] \quad (2.4)$$

Where, θ is temperature, t is time, α is thermal diffusivity, Δx is sheet thickness, Δx_E is electrode face thickness, θ_P is peak temperature in the FZ, k_E is the thermal conductivity of the electrode material, k_S is thermal conductivity of steel, and x is the position through the spot weld.

Pouranvari et al. (2015a) calculated the cooling rates for RSW of 1.2mm-thick low carbon steel and different grades of stainless steels in the temperature range of 400-1400 ^{o}C based on this model, and the results are compared in Figure 2.14. The cooling rate for low carbon steel in the martensitic transformation temperature range (800–500 ^{o}C) was found to be approximately in the range of 6000 – 8000 ^{o}C/s. On the other hand, for stainless steels, the cooling rate in the solidification and post-solidification transformations temperature range (1200–1400°C) was found to be approximately 6000-10000 °C/s. These very high cooling rates influence the phase transformations that occur in the FZ.

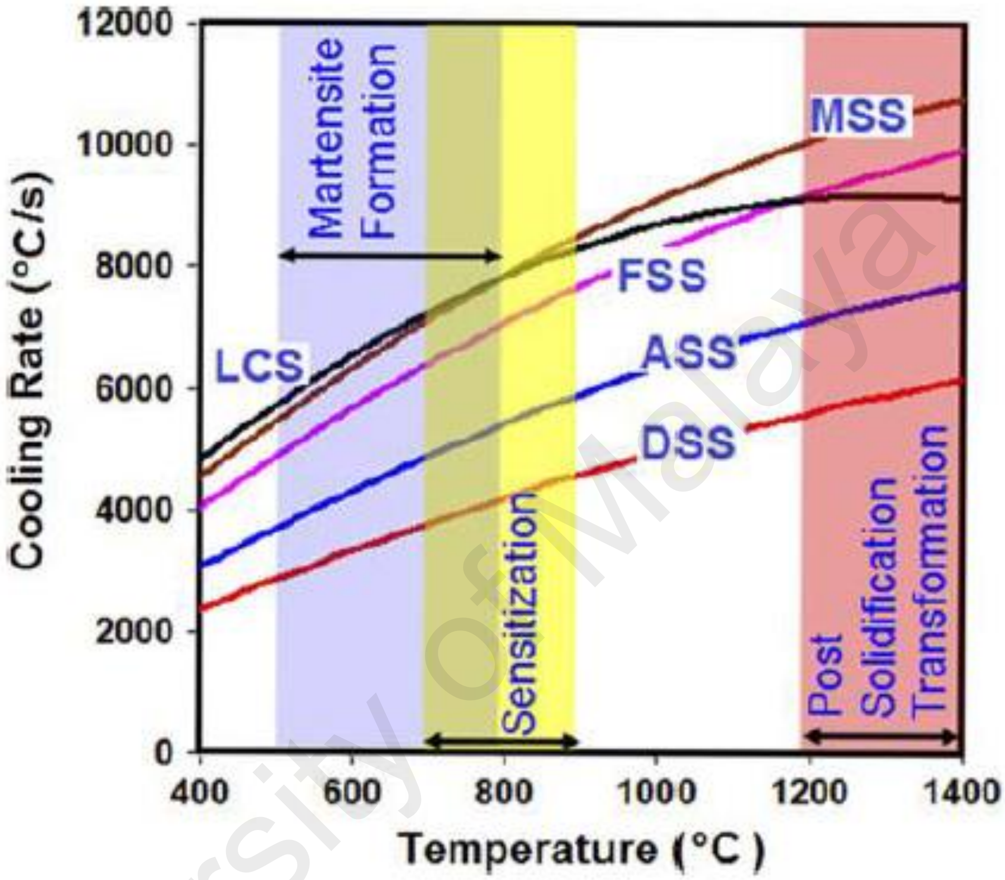

Figure 2.14: Calculated cooling rates during RSW of 1.2 mm thick low carbon steel and stainless steels (Pouranvari et al., 2015a)

Numerous researchers have studied the phase transformations and microstructural evolution that occur during RSW of ASS (Alizadeh-Sh et al., 2015; De Tiedra et al., 2011; Fukumoto et al., 2008a; Fukumoto et al., 2008b; Karcı et al., 2009; Kianersi et al., 2014a; Marashi et al., 2008b; Özyürek, 2008; Pouranvari et al., 2015a; Zhang et al., 2016).

It was observed during the RSW of 304L ASS (Özyürek, 2008) and 316L ASS (Kianersi et al., 2014a) that the nugget microstructure consisted of columnar structure, with grains elongated parallel to the electrode compression direction.

Figure 2.15 shows the typical macrostructure and microstructures that were observed during RSW of 304L ASS (Pouranvari et al., 2015a). The microstructure of the base metal, which was fully austenitic (Figure 2.15b), transformed into a dual phase microstructure (austenite and delta ferrite) in the FZ (Figure 2.15 d and e). As shown in Figure 2.15 c, two distinct zones were identified in the nugget, i.e., zone I at the center of the nugget and zone II at the periphery of the nugget. This type of two-nugget was also observed by Zhang et al. (2016) during RSW of three-sheet 304 ASS (Figure 2.16). However, the peripheral zone (FZ1 in Figure 2.16 a) is narrower than in the case of two-sheet RSW due to the addition of one extra sheet which would reduce the cooling rate (Zhang et al., 2016). The formation of two-zone nugget in ASS RSW has been attributed to the differences in volume fraction of delta ferrite between the periphery and the main nugget (Lippold & Kotecki, 2005; Pouranvari et al., 2015a; Zhang et al., 2016). During welding, the austenitic microstructure of the BM transforms into a mixture of austenite and delta ferrite (Lippold & Kotecki, 2005; Zhang et al., 2016), as shown in Figures 2.15 and 2.16. During this transformation, the ferrite is consumed by austenite through a diffusion controlled reaction. The cooling rate is higher at the periphery than at the center of the nugget because of its proximity to the water-cooled electrodes. Therefore, there is limited time for the diffusion controlled reaction to occur in the periphery, leading to a higher volume fraction of delta in the peripheral zone (Lippold & Kotecki, 2005; Pouranvari et al., 2015a; Zhang et al., 2016). For instance, the volume fraction of delta ferrite in the peripheral nugget zone of two-sheet 304L ASS resistance spot weld was found to be ~24% while that in nugget center was found to be ~14% (Pouranvari et al., 2015a).

It is important to note that, as observed by Kianersi et al. (2014a), during RSW of 316L ASS, the morphology of the delta ferrite present in the nugget depends on the heat input. Under low heat input conditions, lathy and skeletal delta ferrite morphologies are formed. However, under high heat input, in addition to skeletal and lathy delta ferrite, acicular delta ferrite was also observed (Kianersi et al., 2014a).

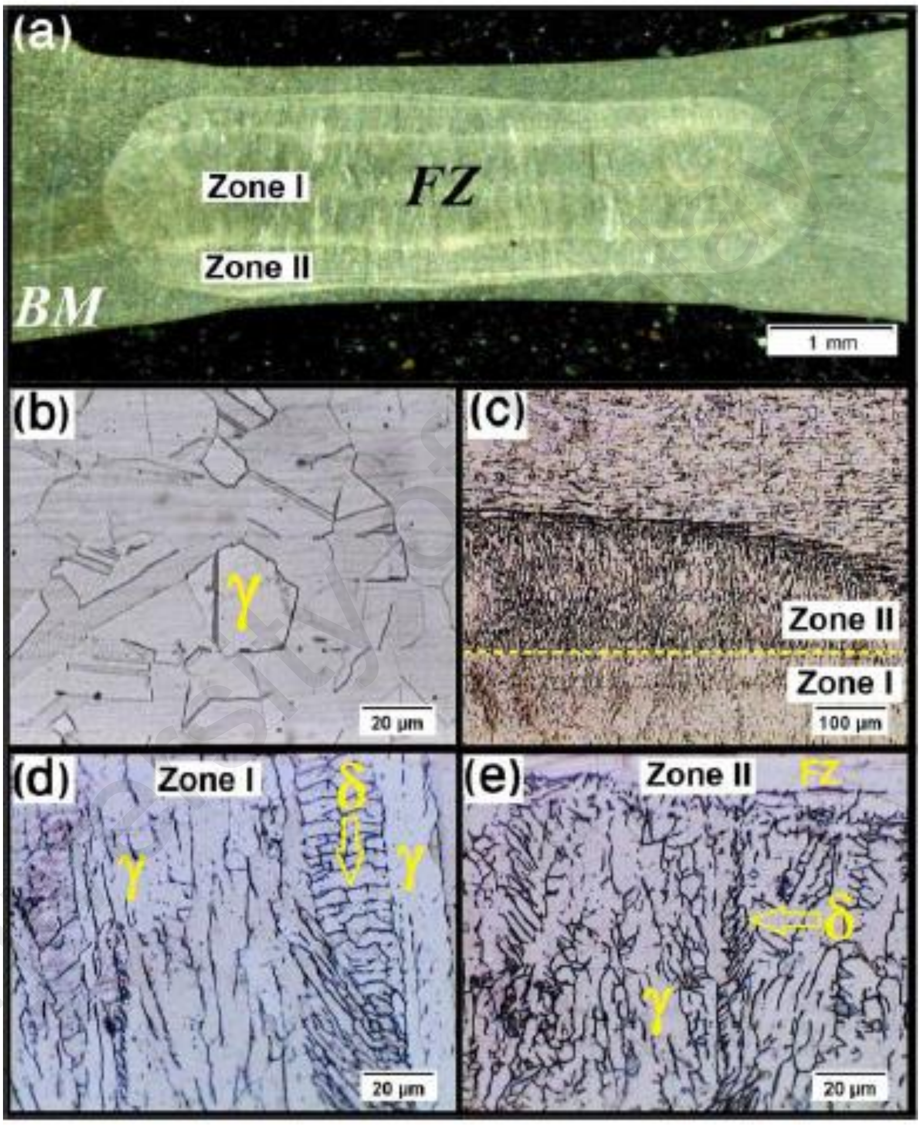

Figure 2.15 : (a) typical macrostructure of 304L ASS resistance spot weld (b) BM microstructure, (c) FZ microstructure , (d) microstructure center of the nugget and (e) microstructure of the nugget edge (Pouranvari et al., 2015a)

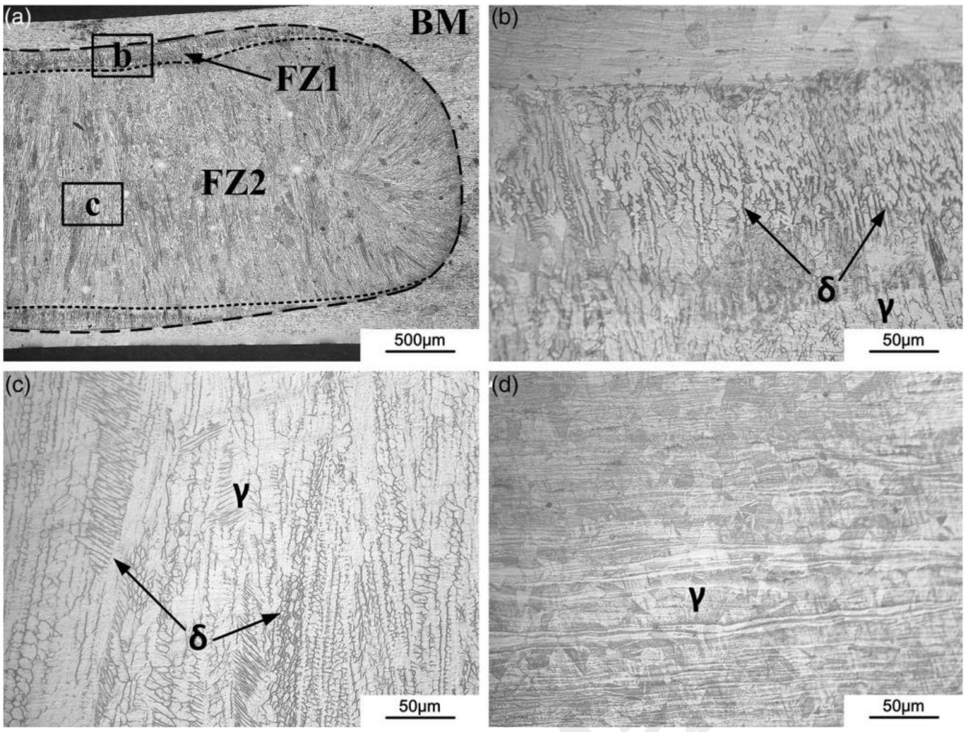

Figure 2.16 : Microstructures of three-sheet RSW of 304 ASS spot weld (a) Typical nugget microstructure; (b), (c) magnified regions in (a); (d) BM (Zhang et al., 2016)

For cold worked ASS resistance spot welds, while the BM microstructure consisted of austenite grains, elongated along the strain direction, the microstructure of the nugget consisted of austenite and lathy delta ferrite. The work hardening effect was lost completely in the nugget because of melting and re-solidification (Karcı et al., 2009)

The microstructural development during small scale RSW (SSRSW) of different types of ASSs has also been investigated (Fukumoto et al., 2008a; Fukumoto et al., 2008b). Figure 2.17 shows the optical microstructures of 316L, 302, 310S, and 347 ASSs welds produced by SSRSW. The nugget exhibited columnar structures, consisting of almost fully austenitic microstructure. Small amount of ferrite was also observed at the austenite grain boundaries (Fukumoto et al., 2008a). The presence of only small amount of delta has been attributed to the high cooling rate of SSRSW (about 6.2 x 10^4 to 6.5 x 10^5 K/s) (Fukumoto et al., 2008b). A similar observation was made during SSRW of high nitrogen, nickel-free ASS. However, in addition to the small amount of delta ferrite at the grain boundaries, chromium nitride was observed in the austenite grains and grain boundaries (Fukumoto et al., 2008b).

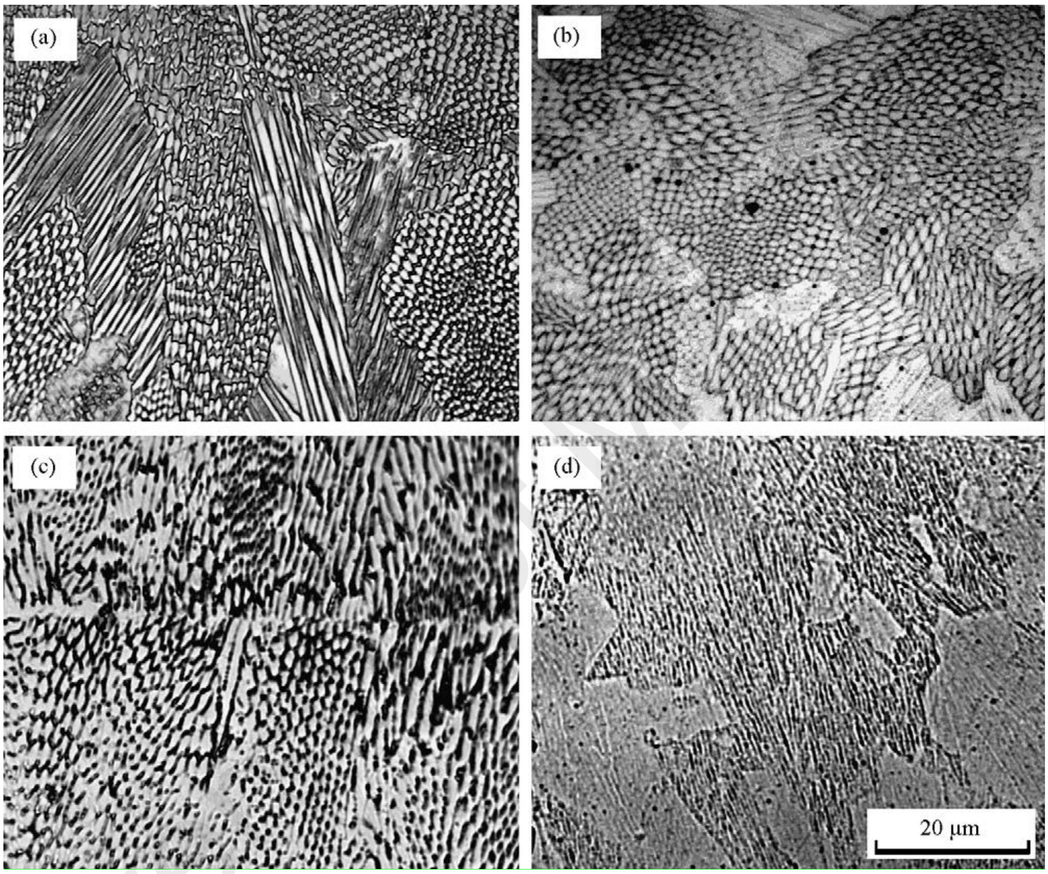

Figure 2.17: Microstructures in the nugget of types (a) 316L, (b) 302, (c) 310S, and (d) 347 ASS produced by SSRSW (Fukumoto et al., 2008a)

The microstructure in the HAZ of ASS resistance spot welds has also been studied (Alizadeh-Sh et al., 2015; De Tiedra et al., 2011; Karcı et al., 2009; Kianersi et al., 2014a; Marashi et al., 2008b; Özyürek, 2008). It has been reported that ASSs resistance spot welds exhibit narrow HAZ due to the combined effect of the low thermal conductivity and thermal diffusivity of ASSs and the high heat intensity of RSW (Alizadeh-Sh et al., 2015). Although phase transformation does not occur in the HAZ because ASSs are untransformable, the grain structure of the HAZ could be affected (Marashi et al., 2008b), and, depending on the heat input, any prior cold work may be lost because of recrystallization (De Tiedra et al., 2011; Karcı et al., 2009). Generally, some grain growth has been observed in the HAZ (Alizadeh-Sh et al., 2015; Karcı et al., 2009; Kianersi et al., 2014a; Marashi et al., 2008b; Özyürek, 2008). For example, it has been observed in the HAZ of 316L ASS (Alizadeh-Sh et al., 2015) and cold worked 304 ASS (Karcı et al., 2009) resistance spot welds. It was found that the extent of the grain growth depends on the distance from the fusion boundary. The shorter the distance from the fusion boundary, the higher the peak temperature and the greater the extent of grain growth (Karcı et al., 2009).

2.4.2.2 Hardness characteristics

Hardness variation across a weldment is important in determining the ductility of the joint and the failure location. The hardness of the FZ of ASS spot welds is influenced by grain size and ferrite content (Pouranvari et al., 2015a).

Generally, the hardness of the FZ and HAZ are lower than that of the BM (Marashi et al., 2008b; Pouranvari et al., 2015a). Figure 2.18 shows the typical hardness profile of 304L ASS resistance spot weld. It is clearly seen that the hardness of the FZ is less than that of the BM. Although the FZ exhibited dual phase structure, which should increase its hardness relative to that of the BM, the combined effect of cast structure, with coarse columnar grains, and the loss of any prior cold work in the FZ would result in under-matched FZ hardness (Marashi et al., 2008b; Pouranvari et al., 2015a). Moreover, as shown in Figure 2.18, compared with that of the BM, hardness reduction occurred in the HAZ. The hardness of the HAZ of ASSs is influenced by recrystallization, grain growth and carbide precipitation (Alizadeh-Sh et al., 2015; Marashi et al., 2008b). However, the as-received BM was in annealed condition and therefore recrystallization could not have occurred in the HAZ. Furthermore, 304L ASS is a low carbon grade, implying that Cr carbide precipitation would not occur. Therefore, the observed hardness reduction in the HAZ was attributed to grain growth (Alizadeh-Sh et al., 2015).

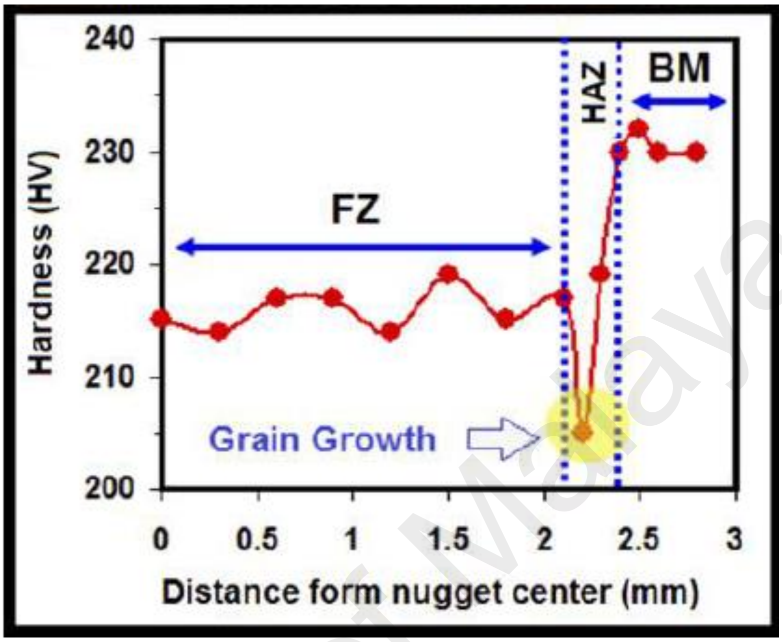

Figure 2.18: Hardness profile of 304L ASS resistance spot weld (Alizadeh-Sh et al., 2015)

Kianersi et al. (2014a) studied the hardness variation across 316L ASS spot welds produced at different welding currents, and the results are shown in Figure 2.19. Irrespective of the welding current, the nugget had the lowest hardness followed by the HAZ. The hardness reduction in the HAZ was likely due to the occurrence of grain growth. The hardness gradually increased in the HAZ, from the edge of the FZ to that of the BM. This behavior was attributed to the occurrence of grain growth near the FZ as a result of slower cooling rate and to the presence of finer grains near the BM due to faster cooling rate (Kianersi et al., 2014a). Karcı et al. (2009) investigated the effect of RSW on the hardness of cold worked 304 ASS joints welded in air and in nitrogen environment. For the both environments, the joints were found to exhibit similar hardness profiles. However, the nugget hardness of the joints welded in nitrogen was about 30–35 HV higher than that of those welded in air because of the presence of nitrogen enriched austenite in the nugget. Furthermore, for both environments, the HAZ hardness decreased with increase in the degree of cold work because severe deformation would decrease the recrystallization temperature, leading to grain coarsening. The nugget hardness of the cold worked samples welded in air was found to be 20HV higher than that of the welded undeformed (not subjected to cold working) samples. This was attributed to finer grain size of the cold worked samples. Irrespective of the environment and sample condition, it was found that the HAZ hardness decreased with increased welding time due to grain size enlargement.

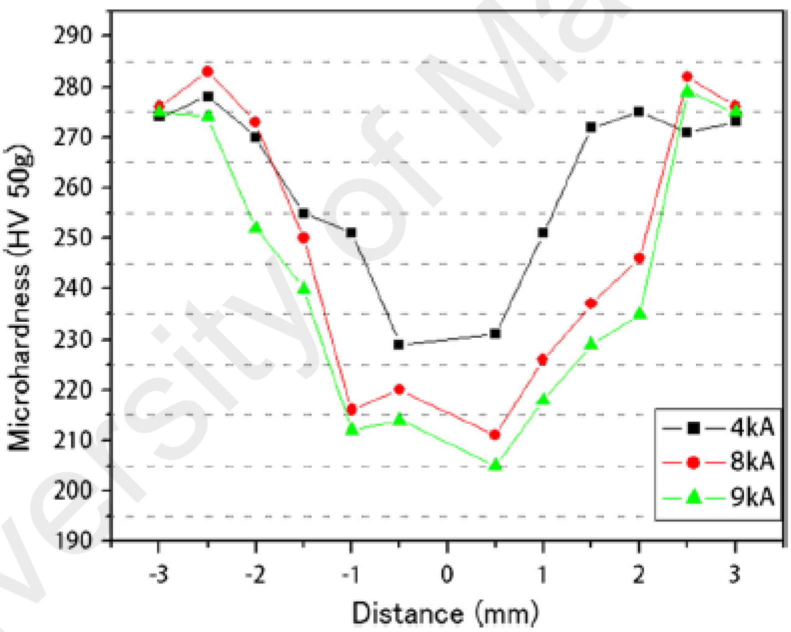

Figure 2.19 : Hardness profile of 316L ASS resistance spot welds produced at different welding currents (Kianersi et al., 2014a)

Zhang et al. (2016) compared the hardness variation of three-sheet resistance spot welds of 304 ASS and DQSK steel (Figure 2.20). The 304 ASS welds exhibited smaller hardness variation, which was attributed to the fact ASSs are not transformable. The hardness of the ASS nugget was found to be lower than that of the BM, and some softening was also observed in the HAZ, close to the edges of the nugget. On the other hand, the hardness in the nugget of DQSK steel was significantly higher than that of the BM due to martensitic transformation.

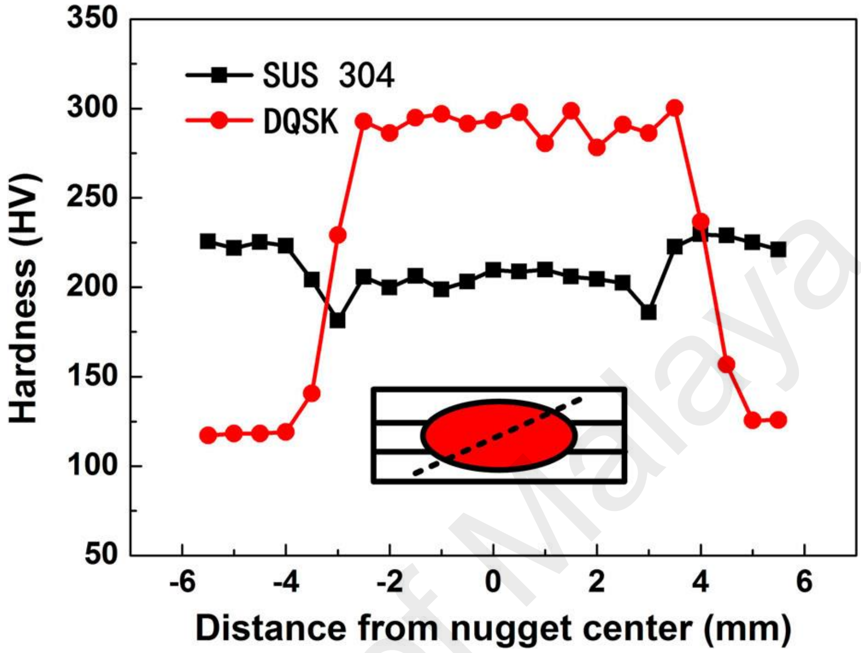

Figure 2.20 : Vickers hardness distribution of ASS and DQSK RSW joint (Zhang et al., 2016)

2.5 Joining Mg alloy to steel by RSW techniques

2.5.1 Conventional RSW

Steel is a primary structural material in the automotive industry. With the increased use of Mg alloys, the dissimilar joining of Mg alloys to steel is inevitable. The research conducted so far on RSW of Mg to steel is limited.

As shown in Table 2.4, large differences exist between the physical and metallurgical properties of Mg alloys and steel. During RSW, much more heat would be generated on the steel side because of its higher electrical resistivity than on the Mg side. This might cause melting of the steel and the evaporation of Mg alloy.

Table 2.4 : Comparison between properties of Mg, aluminum and iron (Cao et al., 2006)

Properties	Mg	Aluminum	Iron
Ionization energy (eV)	7.6	6	7.8
Specific heat ($Jkg^{-1}k^{-1}$)	1360	1080	795
Specific heat of fusion(J/kg)	3.7×10^{5}	4×10^{5}	2.7×10^{5}
Melting point (ºC)	650	660	1536
Boiling point (ºC)	1090	2520	2860
Viscosity ($kgm^{-1}s^{-1}$)	0.00125	0.0013	0.0055
Surface tension (Nm^{-1})	0.559	0.914	1.872
Thermal conductivity ($Wm^{-1}k^{-1}$)	78	94.03	38
Thermal diffusivity ($m^{2}s^{-1}$)	3.73×10^{-5}	3.65×10^{-5}	6.80×10^{-6}
Coefficient of thermal expansion (1/k)	25×10^{-6}	24×10^{-6}	10×10^{-6}
Density (kg/m^{3})	1590	2385	7015
Elastic modulus (N/m^{3})	4.47×10^{10}	7.06×10^{10}	21×10^{10}
Elastic resistivity (μΩm)	0.274	0.2425	1.386
Vapor pressure (Pa)	360	10^{-6}	2.3

Liu et al. (2010b) proposed the use of flat electrode and domed-shaped electrode against the steel and Mg sides, respectively. This would reduce the current density, increase the cooling rate of the steel side and, thus, balance the heating. Using this technique, AZ31B Mg alloy was welded to zinc-coated DP600 steel and a joint with strength of 5 kN (which is about 95 percent of the strength of an optimized Mg/Mg joint) was obtained. In another work, AZ31B Mg alloy and hot-dip galvanized HSLA steel were joined using same technique of asymmetric electrodes (Liu et al., 2013). Both studies showed that Mg alloy was joined to zinc coated steel by three different mechanisms, i.e. soldering with zinc based filler material (zinc coating), solid state bonding of Mg to steel and weld brazing in the center of the weld (Liu et al., 2013; Liu et al., 2010b). It was found that no continuous IMC layer was formed at the Mg/steel interface in the solid state and weld brazing regions, and that zinc penetrated into the Mg BM along the grain boundaries in the soldered region. These resulted in the formation of a joint with a strength similar to that of Mg/Mg joint. Min et al. (2015) joined AZ31B Mg alloy and 443 ferritic stainless steel sheets, each 0.4mm thick, by RSW. The joint formation mechanism involved the melting and wetting of the steel by the Mg alloy. Cracks were observed in the nugget, which was attributed to the thermal behavior of various elements in the nugget.

The feasibility of using interlayers during RSW of Mg alloy to steel was investigated (Feng et al., 2016b; Jiang et al., 2015; Zhang et al., 2014a). Jiang et al. (2015) investigated the effect of adding Cu-Zn interlayer on the mechanical properties of resistance spot welded joints between AZ31B Mg alloy and Q235 steel. The average tensile strength of the joint obtained at optimum welding parameters without interlayer was 30 MPa. The addition of Cu-Zn interlayer had an influence on the strength of the joint. Average tensile strength of 44MPa was obtained when 0.05mm thick Cu-Zn interlayer was used. The strength increased to 62 MPa as the interlayer thickness was increased to 0.1mm. However, the strength decreased to 27 MPa when the interlayer thickness was in the range of 0.2 mm to 0.3 mm. This decrease in strength with increased interlayer thickness was attributed to the high thermal conductance of Cu-Zn interlayer, which would result in higher heat input, volatilization of Mg alloy, and consequently pores formation. It was found that the metallurgical bonding between the Mg alloy and steel, with the addition of Cu-Zn interlayer, was due to the formation of CuMgZn intermetallic compounds and solid solutions of Cu in Fe. In another study, Zhang et al. (2014a) used Ni interlayer to join AZ31B Mg alloy and Q235 steel by RSW, and they obtained an average tensile shear strength 75MPa. The bonding was found to be enhanced by the formation of Mg_2Ni IMC and a solid solution of Ni in Fe at the interface of the center of the nugget zone. More recently, Feng et al. (2016b) joined 2-mm-thick AZ31B Mg alloy and 1.2-mm-thick electro-galvanized DP600 steel using a 0.6-mm-thick hot-dip galvanized Q235 steel interlayer. The joints obtained possessed 30% higher peak load and two times higher energy absorption than those produced without interlayer. For both cases, asymmetrical electrodes were used in order to improve the heat balance.

The fatigue behaviour of Mg alloy/steel resistance spot welds was also studied (Liu et al., 2013). It was found that the crack initiated at the notch root of both steel and Mg sides. However, the cracks propagated along different directions, as shown in Figure 2.21.

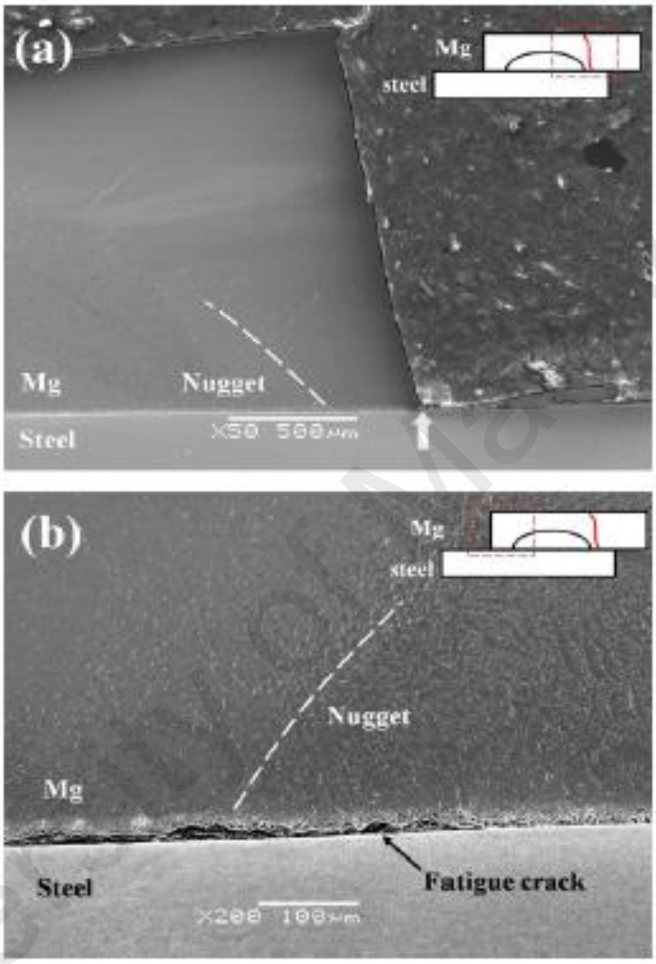

Figure 2.21: Mg/steel spot weld after fatigue test at a maximum load of 2.0 kN: (a) Mg end and (b) steel end (Liu et al., 2013)

The crack at the Mg side, propagated through the Mg base metal, leading to fracture. However, the crack at the steel side propagated along the Mg/steel interface and moved only a distance of 400-500 µm, which is extremely small compared to the nugget size (9.4mm). This shows that the crack propagation rate of the Mg/steel interface was much lower than that of the Mg base metal. It was also shown that Mg/Mg similar and Mg/steel dissimilar joints had equivalent fatigue resistance; they both exhibited similar crack propagation behaviour, and both failed through thickness in the Mg side. However, the cause of crack initiation was different. For Mg/steel dissimilar joint, the crack initiation was attributed to the penetration of zinc into the Mg base metal as a result of liquid metal induced embrittlement. For Mg/Mg joint, stress concentration, grain growth, and the existence of Al-rich phases in the grain boundaries of HAZ were responsible for crack initiation (Liu et al., 2013).

2.5.2 RSWB

RSWB is an innovative and advanced hybrid joining technology which combines the advantages of RSW and adhesive bonding. It is now widely used in automobile, railway carriages, and aircraft manufacturing industries (Liu et al., 2011; Tao et al., 2014). It produces more desirable joints than either RSW or adhesive bonding. In addition to reducing the number of welds required in a vehicle, it offers the following advantages, among others: reduced manufacturing costs, improved stiffness and load –bearing capacity, enhanced stress distribution, fatigue resistance and crashworthiness, better corrosion resistance and elimination of the need for sealants (Khan et al., 2015; Liu et al., 2011; Sam & Shome, 2010; Shen et al., 2012; Zhang et al., 2014b). The structural adhesives are applied on the surface of the sheets, followed by RSW and then curing at a suitable temperature for a suitable period of time (Sam & Shome, 2010; Zhang et al., 2014b). The stages of RSWB are illustrated in Figure 2.22.

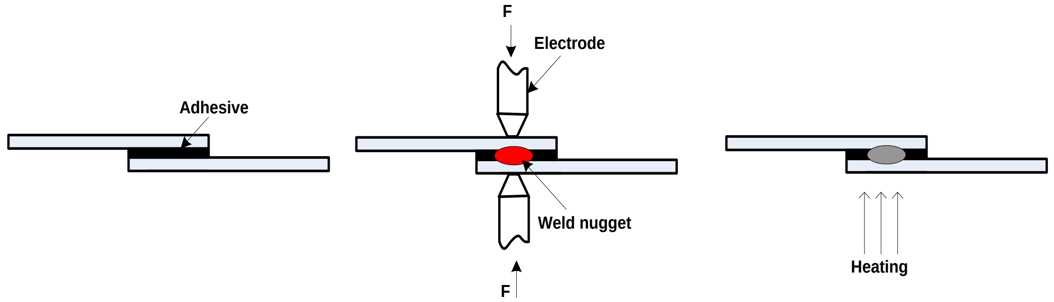

Figure 2.22 : Stages of weld-bonding: (a) applying adhesives, (b) RSW, and (c) curing in an oven (Manladan et al., 2016)

Xu et al. (2012) studied the microstructure and mechanical behavior of weld-bonded Mg-to-Mg joints (WB Mg/Mg) and Mg-to-steel joints (WB Mg/steel) in comparison with resistance spot welded Mg-to-steel joints (RSW Mg/steel). The Mg alloy, steel, and adhesives used were 2 mm AZ31B Mg alloy, 0.7 mm hot-dip galvanized HSLA, and Terokal® 5087-02P, respectively. The weld-bonded samples were cured at a temperature of 180 ^{o}C for 30 min. Equiaxed dendritic and divorced eutectic structures were observed in the FZ of the WB Mg/Mg joint. In both the RSW Mg/steel and WB Mg/steel joints, the FZ formed on the Mg side and its microstructure consisted of equiaxed dendritic and columnar dendritic structures. However, the steel side of RSW Mg/steel underwent microstructural changes, forming a mixture of lath martensite, bainite, pearlite, and retained austenite. Consequently, significant increase in microhardness was observed, while the microstructure of the WB Mg/steel did not change due to relatively slower cooling rate. Shrinkage cracks were observed in RSW Mg/steel joint in the FZ, adjacent to the steel. Such cracks were not observed in the WB Mg/steel due to relatively lower cooling rate which resulted from the use of adhesive. However, thicker layer of IMC, consisting of $MgZn_2$ and Mg_7Zn_3 formed in WB Mg/steel joints while thinner IMC layer, consisting of $MgZn_2$ formed in RSW Mg/steel. Generally, the use of adhesive led to significant improvement in mechanical properties. The maximum tensile shear load and energy absorption of the WB Mg/Mg and WB Mg/steel were greatly higher than for RSW Mg/steel joints, as shown in Figure 2.23. Furthermore, the use of adhesive reduced the stress concentration around the nugget which improved the fatigue behavior. For a given number of cycles, the fatigue strength of WB Mg/Mg and WB Mg/steel was three times higher than that of RSW Mg/steel joints.

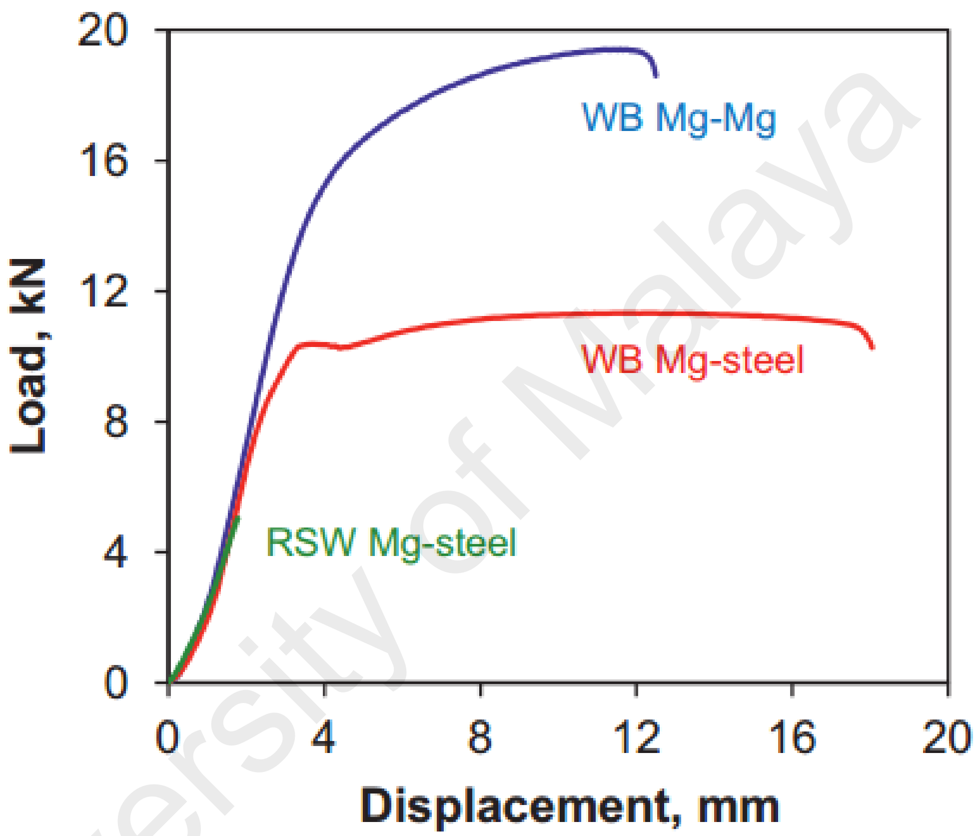

Figure 2.23: Tensile load versus displacement for the WB Mg/Mg similar joint, WB Mg/steel dissimilar joint, and RSW Mg/steel dissimilar joint (Xu et al., 2012)

In another study, Xu et al. (2013) studied the influence of the size of overlap bonding area on the microstructures, tensile, and fatigue strengths of RSWB 2-mm-thick AZ31B-H24 Mg alloy similar joints. Terokal® 5087-02P (cured at a temperature of 180°C for 30 min) adhesive was also used in this study. Two types of joints with different size of bonding areas were produced: WB-1, which had a bonding area of 35mm x35 mm and WB-0.5, which had a bonding area of 17.5mm x35 mm. It was observed that the FZ of both WB-1 and WB-0.5 consisted of typical equiaxed dendritic structures with $Mg_{17}Al_{12}$ particles at the interdendritic and intergranular regions. Also, for both types of joint, the HAZ was characterized by equiaxed recrystallized grains. However, less solidification cracking or shrinkage was observed in WB-0.5 than in WB-1 joints. This was attributed to slower cooling rate caused by the reduced bonding overlap area. It was also found that, due its larger bonding area, the WB-1 joint was stronger than WB-0.5 joint. The tensile shear load of WB-1 joint and WB-0.5 joint was about 18 kN and 9kN, respectively. A study of the fatigue behavior of the joints showed that both WB-1 and WB-0.5 joints had equivalent fatigue life at low cycle fatigue regime (higher cyclic stress level). At high cycle fatigue regime (lower cyclic stress levels), however, WB-0.5 joints exhibited longer fatigue life than WB-1 joints due to less solidification or shrinkage cracks in the nugget of WB-0.5 joints. Moreover, at higher cyclic load levels, cohesive failure within the adhesive layer in combination with partial nugget pull out was observed while failure occurred in the BM at lower cyclic load levels.

2.6 REW

REW is a novel joining technology that combines both thermal (RSW) and mechanical (rivet) joining principles. The technique was developed to address the challenges of joining Al alloys to steels. As illustrated in Figure 2.24, a hole is pre-punched in the Al alloy, and an auxiliary element (a steel rivet) is inserted into the hole, followed by RSW on the rivet/steel. Meschut et al. (2014a) compared the mechanical performance of 2mm 6016 Al alloy/1.5mm 22MnB5 boron steel joints produced by REW (using S355 steel rivet as the auxiliary element), friction element welding (FEW), and self-piercing rivet (SPR). The failure load of the joints produced by FEW, REW, and SPR was in the range of approximately 7.2– 9.0 kN, 4.5–5.0 kN, and 3.9–4.4 kN, respectively. Qiu et al. (2015) found that the peak load of A6061 Al alloy/ Q235 steel joints produced by REW was 37% higher than that produced by RSW. Ling et al. (2016) compared the mechanical performance of 2mm 6061 Al alloy/1.8mm uncoated 22MnMoB boron steel joints produced by RSW and REW. The RSW produced a weak joint, with a peak load of 0.96 kN and energy absorption of 0.09J, while REW produced a strong joint, with a peak load of 7 kN and energy absorption of 11.38J. Recently, Meschut et al. (2017) have shown that REW and FEW can be used in combination with adhesive bonding to produce Al alloys/ultra-high-strength steel joints with outstanding load-bearing capacity. Therefore, REW is a promising technique to join Al alloys to steels, and according to Innojoin (2017), it has already been implemented in series production line of Volkswagen Passat B8 model for joining Al alloy to steel components. Holtschke and Jüttner (2016) have shown that the technique can also be used to join a thermally sensitive sandwich material, such as LITECOR®, to a high-strength steel. However, to realize the full potentials of this technique, it needs to be studied extensively and applied to a wide range of light alloys/steel combinations.

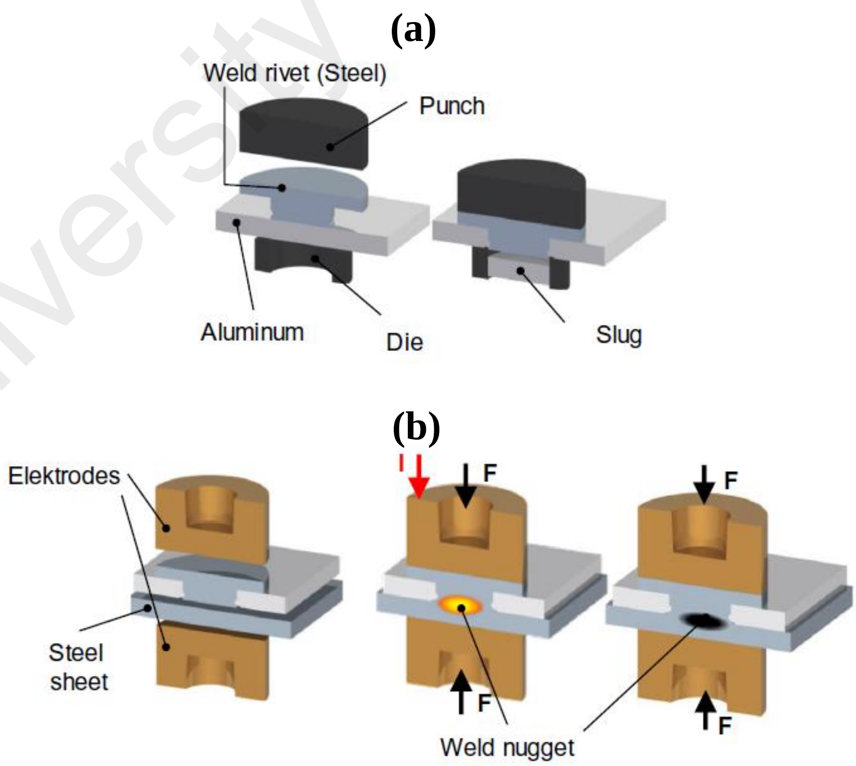

Figure 2.24 : Stages of REW process (a) pre-punching of rivet hole; (b) RSW (Meschut et al., 2017)

2.7 Summary

RSW is a widely used sheet joining process. The RSW of Mg alloys usually results in the formation of a columnar dendritic structure and equiaxed dendritic structure in the edge and center of the nugget, respectively. Generally, minimal hardness variation has been observed across the BM, HAZ, and FZ of Mg alloy spot welds.

During RSW of ASS, a two-zone FZ is normally observed, comprising of a peripheral FZ at the edges of both sheets and the main FZ. The austenitic microstructure of the BM transforms into a mixture of austenite and delta ferrite in the FZ via a diffusion controlled reaction. The cooling rate is higher at the periphery than at the center of the nugget because of its closeness to the water-cooled electrodes. Therefore, there is limited time for the diffusion controlled reaction to occur in the periphery. Consequently, the peripheral FZ has a higher volume fraction of delta. Generally, the hardness of the FZ is lower than that of the BM. Furthermore, although ASSs are untransformable, some grain growth has been observed in the FZ, leading to hardness reduction.

The combination of adhesive bonding and RSW techniques results in significant improvement of joint performance. REW is found to be a promising technique for joining Al alloy/steel. However, it needs to be applied to various materials combinations for it to be widely accepted in the transportation industry.

So, far the work conducted on RSW of Mg alloy/steel is limited, and most of the work focused on Mg alloy/zinc-coated steel. The zinc-coating facilitates the joining mechanism. No work has been reported on joining Mg alloy/ASS by any RSW technique, despite their increased application in the transportation industry.

CHAPTER 3: MATERIALS AND METHODS

3.1 Materials

The materials used as base metals in this study were AZ31 Mg alloy and AISI 316L ASS, with a thickness of 1.5 mm and 0.7mm, respectively. ASSs possess unique work-hardening behavior and excellent energy absorption capability. Therefore, various sections of a vehicle can be made with thin ASS sheets in order to reduce weight without compromising crash energy absorption. Furthermore, the use of thinner ASS sheet would reduce the heat generation and increase the heat dissipation of the steel side because of its higher electrical resistivity and lower thermal conductivity than Mg alloys, as recommended by Liu et al. (2013). The chemical compositions of the Mg alloy and ASS are listed in Table 3.1.

Table 3.1: Materials compositions (wt. %)

	AZ31 Mg alloy	316L ASS	Q235 Steel
Si	0.1	0.37	0.4
Mn	0.2-0.5	1.65	1.0
C	-	0.029	0.14
Co	-	0.210	-
Mo	-	2.050	-
Ni	-	10.02	-
Cr	-	16.67	-
Zn	0.5-1.5	-	-
Fe	0.005	balance	balance
Al	2.5-3.5	0.002	-
P	0.015	0.034	0.04
S	0.005	-	0.02
Mg	balance	-	-

The auxiliary element used in the REW and REWB processes was a Q235 steel solid rivet, with a diameter of 5 mm. The chemical composition of this steel is listed in Table 3.1.

The adhesive used for the RSWB and REWB processes was Loctite® Hysol E-60HP™ epoxy structural adhesive. It is a two-component (resin and hardener), industrial grade, medium-viscosity, and toughened epoxy adhesive. The fully cured epoxy is resistant to a wide range of chemicals and solvents, and acts as an excellent electrical insulator. The properties of the adhesive, based on the manufacturer's specification, are shown in Tables 3.2-3.4.

Table 3.2: Properties of uncured adhesive (Henkel, 2017)

	Chemical Type	**Mix ratio by volume (R:H)**	**Appearance**	**Specific Gravity at 25°C**	**Viscosity at 25 °C (mPa.s)**	**Flash point (°C)**
Resin (R)	Epoxy	-	Pale yellow liquid	1.00	67,500	>93
Hardener (H)	Amine	-	Yellow liquid	1.00	7,000	>93
Mixture		2:1	Off-white	1.00	-	-

Table 3.3: Curing properties of the adhesive at 25°C (Henkel, 2017)

Properties	**Typical Value**
Working Life (minutes)	60
Tack Free time (minutes)	120

Table 3.4: Typical properties of cured adhesive at 25°C (Henkel, 2017)

Properties	**Typical Value**
Dielectric Strength, (Volts/Mil)	500
Tensile Strength ASTM D-638 (psi)	5,100
Tensile Elongation ASTM D-638 (%)	9
Hardness ASTM D-1706 (Shore D)	80
Glass Transition Temperature, Tg, (°C)	70

3.2 Experimental methods

The experimental methods are summarized in Figure 3.1. They include samples preparation, joining, metallographic examination, mechanical testing, and fracture surface analysis

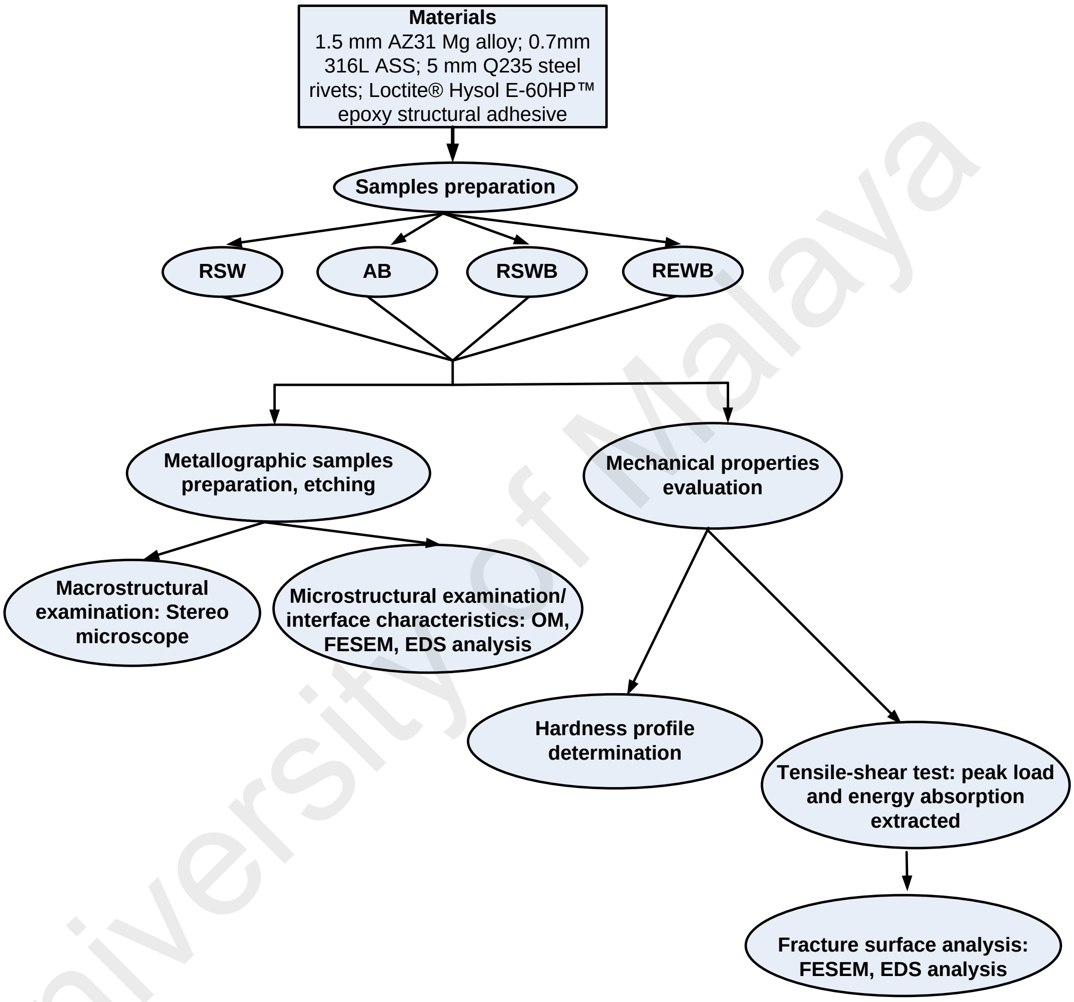

Figure 3.1: Flowchart of experimental methods

3.2.1 Sample preparation

The Mg alloy and ASS sheets were cut into specimens with a width and length of 25 mm and 100 mm, respectively, according to AWS D17.2 Standard (AWS, 2007). Prior to welding, all the specimens were cleaned with alcohol. The surfaces of the Mg alloy specimens were further ground with abrasive paper to clean surface oxides

3.2.2 Joining processes

3.2.2.1 RSW

All the joining processes (RSW, REW, RSWB, and REWB) were conducted on a 220 kW, medium-frequency direct current (MFDC) RSW machine that is controlled by a programmable logic controller. The machine is capable of providing 2–22 kA welding current. The MFDC machine has numerous advantages over traditional industrial frequency (IF) RSW machine. The IF RSW machine generally supplies alternating current (AC) with a frequency of 50 or 60 Hz. It has inherent poor power factor (0.4-0.5) and low energy efficiency because of the existence of zero current state during welding. The MFDC RSW machine takes in 3-phase current, rectifies it to DC, and then uses an inverter to create a single phase AC at a frequency of 1000 Hz in the secondary circuit. This is finally rectified using a single phase full wave rectifier to provide DC. This allows for significant reduction in the size of transformer, while providing higher welding current. Furthermore, the MFDC has higher power factor (nearly 1.0), extremely stable welding current, and high energy efficiency due to the absence of zero current state. Thus, it is a suitable machine, especially for dissimilar materials combinations and weld-bonding (Gould, 2012; Shen et al., 2012; Zhang et al., 2011).

The electrodes used were made of copper alloy (RWMA class II, UNS C18150). The schematic illustration of the samples and electrodes configuration for the RSW process is shown in Figure 3.2. Lap shear specimens were assembled with an overlap distance of 25 mm, according to AWS D17.2 Standard (AWS, 2007). The use of symmetric electrode would result in much higher heat generation and melting of the steel side because of its higher bulk resistance. Therefore, asymmetrical electrodes geometry was used in order to improve the heat balance (Liu et al., 2010b). A spherical electrode, with 50 mm sphere radius and 20 mm face diameter, was used on the Mg alloy side, while a conical electrode with a tip diameter of 10 mm was used against the steel side (Feng et al., 2016b).

After a series of preliminary tests, a welding time of 200 ms, an electrode force of 3.6 kN, and a welding current of 6-18 kA in 2 kA increment were selected for the RSW. The complete welding schedule for the RSW is shown in Figure 3.3.

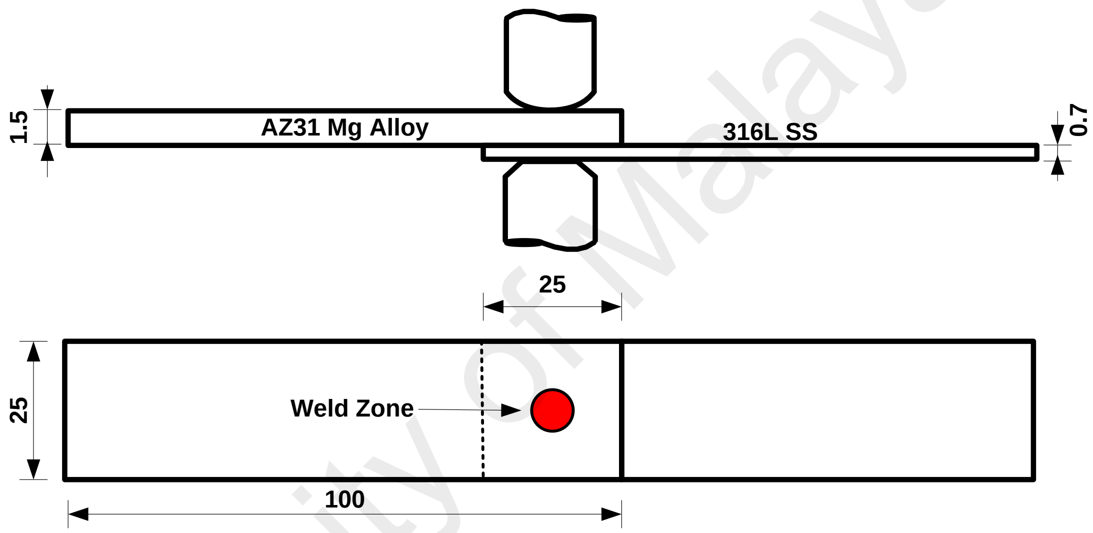

Figure 3.2: Schematic illustration of RSW process

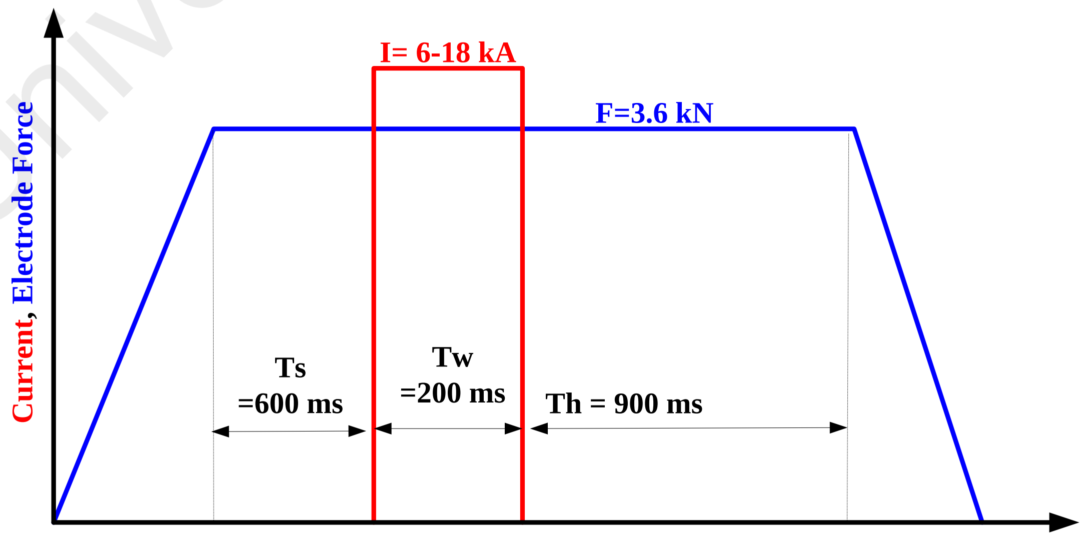

Figure 3.3: Schematic of welding schedule for RSW. Ts is squeezing time, Tw is welding time, Th is holding time, I is welding current, and F is electrode force.

3.2.2.2 RSWB

It has been established in the literature that grinding the surfaces of the base metals is a good pre-treatment for adhesive-bonded and weld-bonded joints, as it enhances the formation of micro-connection points at the metal/adhesive interface (Feng et al., 2016a; Pereira et al., 2009; Pereira et al., 2014). Therefore, prior to RSWB, the surfaces of both Mg alloy and ASS steels were ground with abrasive paper and then cleaned with acetone.

The stages of the RSWB process are illustrated in Figure 3.4. The adhesive was first applied uniformly on the overlap area of the ASS sheet and then the Mg alloy was placed over it under light pressure. RSW was conducted immediately in order not to exceed the working time of the adhesive. After welding, the assembly was cured in furnace at a temperature of 140^{o}C for 30 minutes. The electrodes configuration used for the RSWB is the same as that of RSW. Based on series of preliminary tests, a welding time of 100 ms and welding current of 6-18 kA (in 2 kA increment) were selected. The complete welding schedule for the RSWB is shown in Figure 3.5.

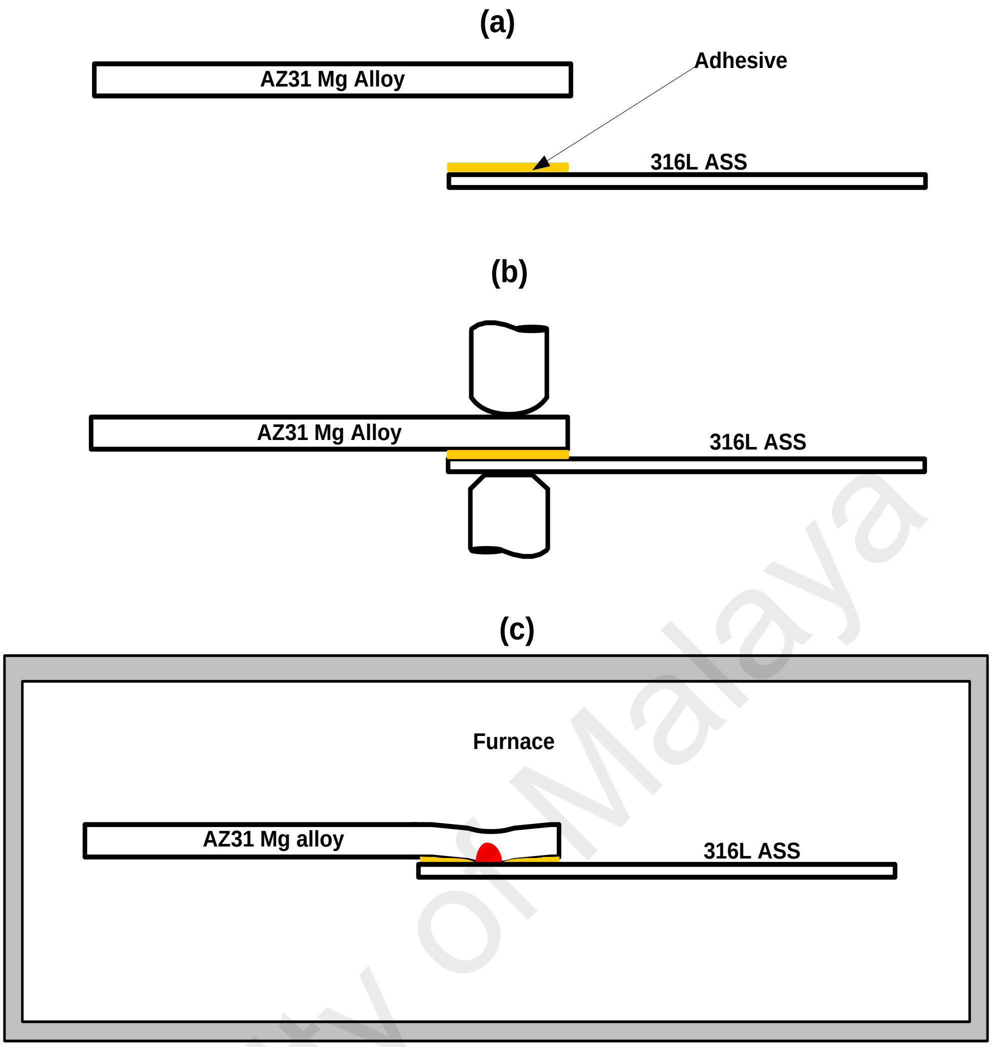

Figure 3.4: Stages of RSWB process: (a) adhesive application; (b) assembly and welding; (c) curing

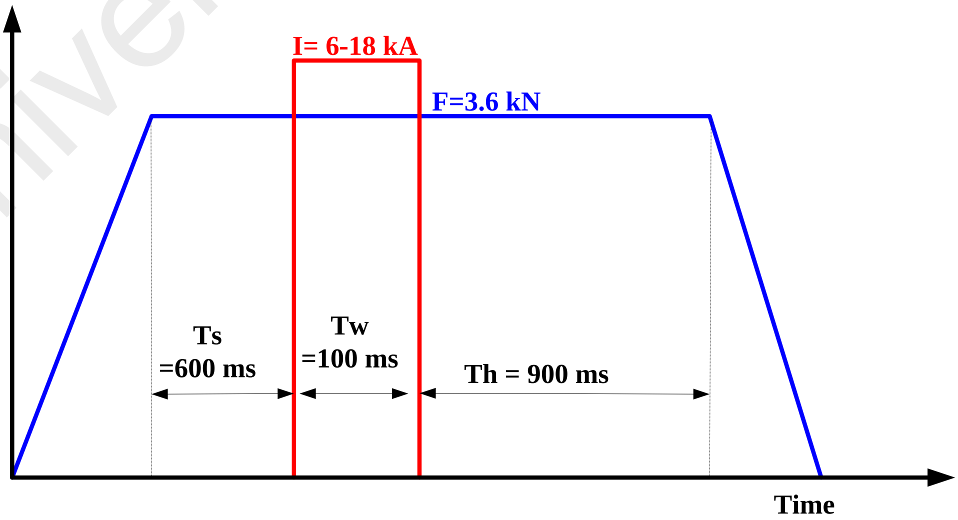

Figure 3.5: Schematic of welding schedule for RSWB

For the purpose of comparison, AB joints were also prepared. The stages of the AB process are illustrated in Figure 3.6. It involves adhesive application, assembly, and curing under the same conditions as the RSWB joints.

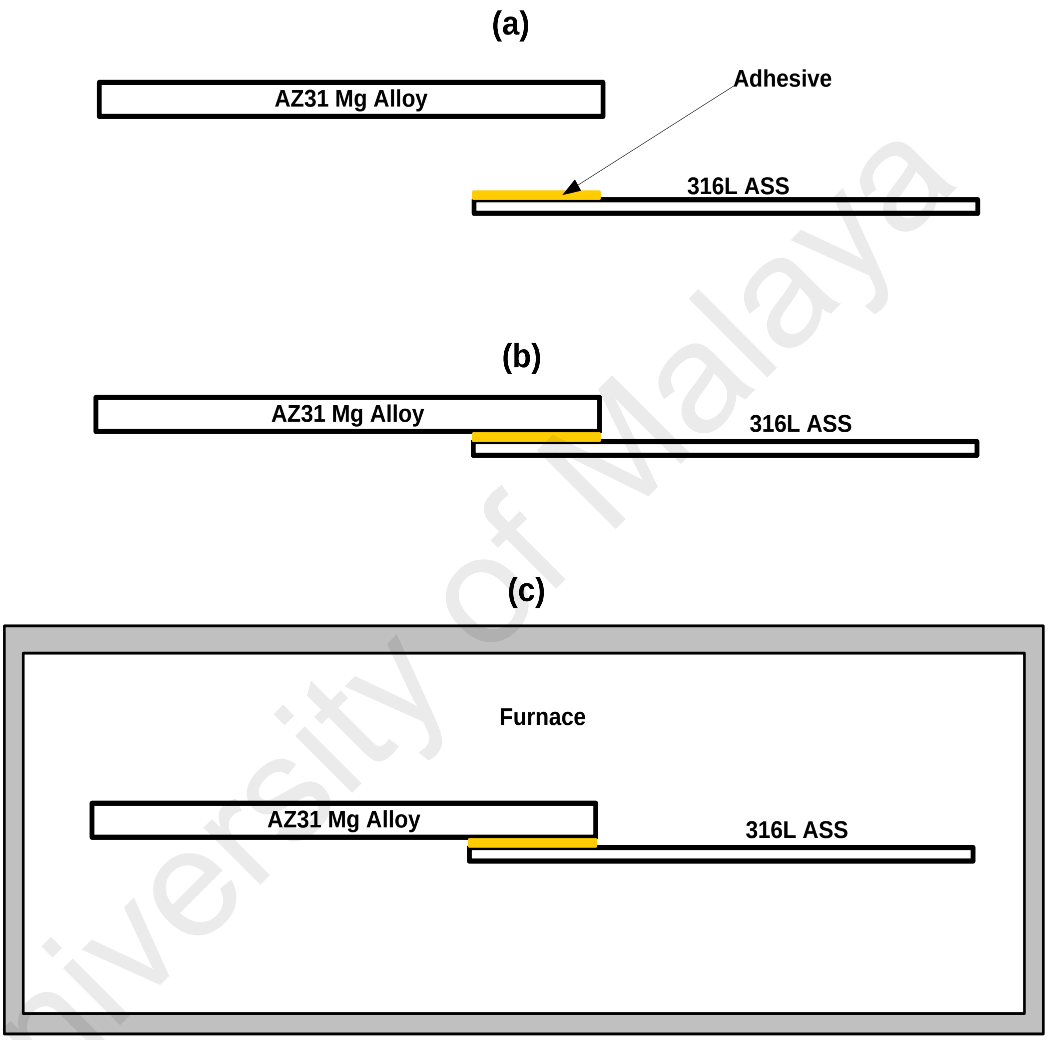

Figure 3.6: Stages of AB: (a) adhesive application; (b) assembly; (c) curing

3.2.2.3 REW

For the REW process, a technological hole, with a diameter of 5mm, was pre-drilled at the center of the overlap area of the Mg alloy, and the Q235 steel rivet was inserted in to the hole. Thereafter, RSW was conducted on the rivet. As shown in Figure 3.7, the domed electrode was used against the Q235 rivet side, with the aim of reducing the current density of the Q235 side. Melting of the Q235 would result in evaporation of the Mg alloy around the rivet sides and consequent widening of the rivet hole. For the REW, a welding time of 250 ms, an electrode force of 3.6 kN, and a welding current of 5-9 kA in 1 kA increment were selected based on preilimary investigation. The complete welding schedule is summarized in Figure 3.8.

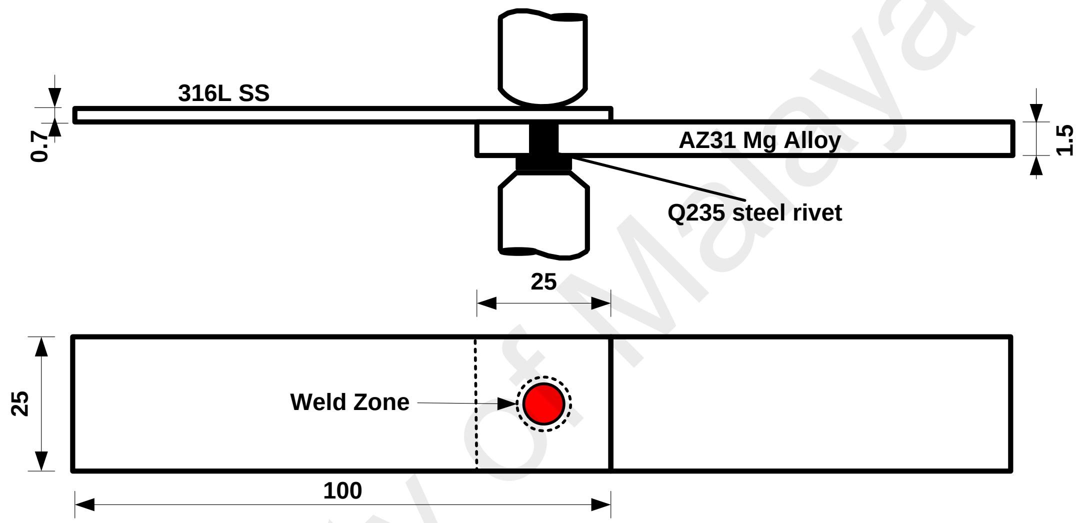

Figure 3.7: Schematic illustration of the REW process

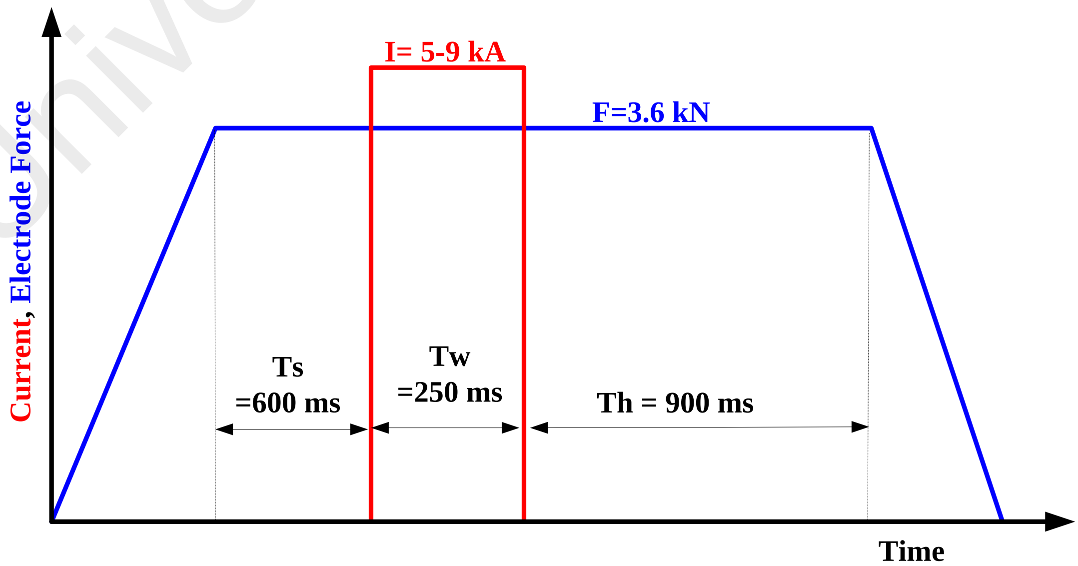

Figure 3.8: Schematic of welding schedule for REW

3.2.2.4 REWB

The stages of the REWB process are illustrated in Figure 3.9. Similar to the REW process, a technological hole, with a diameter of 5mm, was pre-drilled at the center of the overlap area of the Mg alloy, and the Q235 steel rivet was inserted in to the hole. The overlap area of both the sheets were ground with abrasive paper. As illustrated in Figure 3.9, the adhesive was applied on the Mg alloy sheet and the ASS sheet was placed over it, followed by RSW. The electrode configurations are the same as that for REW. A welding time of 150 ms, an electrode force of 3.6 kN, and a welding current of 5-9 kA in 1 kA increment were selected (Figure 3.10). After the welding process, the assembly was cured in a furnace at a temperature of 140^{o}C for 30 minutes.

Note that for all the joining processes, four samples were produced for each set of parameters; three for tensile-sheat test, one for metallographic examination and hardness test.

3.2.3 Metallographic investigations

Samples for metallographic investigation were cut across the center line of the joints, ground, and polished based on standard metallographic procedures. A solution of 5 g picric acid, 5 ml acetic acid, 10 ml H_2O, and 100 ml ethanol was used to etch the Mg side. A solution 4% nital and a solution of 10g $FeCl_3$, 30 ml HCl, and 120 ml H_2O was used to etch the Q235 steel and ASS sides, respectively. The macrostructures (including nugget size measurement) and microstructures of the joints were observed using an Olympus SZX12 stereomicroscope and Olympus GX51 microscope, respectively. Higher magnification microstructural examination was conducted using JOEL JSM7600F field emission scanning electron (FESEM).

The interface characteristics and inter-diffusion of alloying elements across the joints were analyzed using energy dispersive spectroscopy (EDS) line scan and elemental mapping on JOEL JSM7600F FESEM.

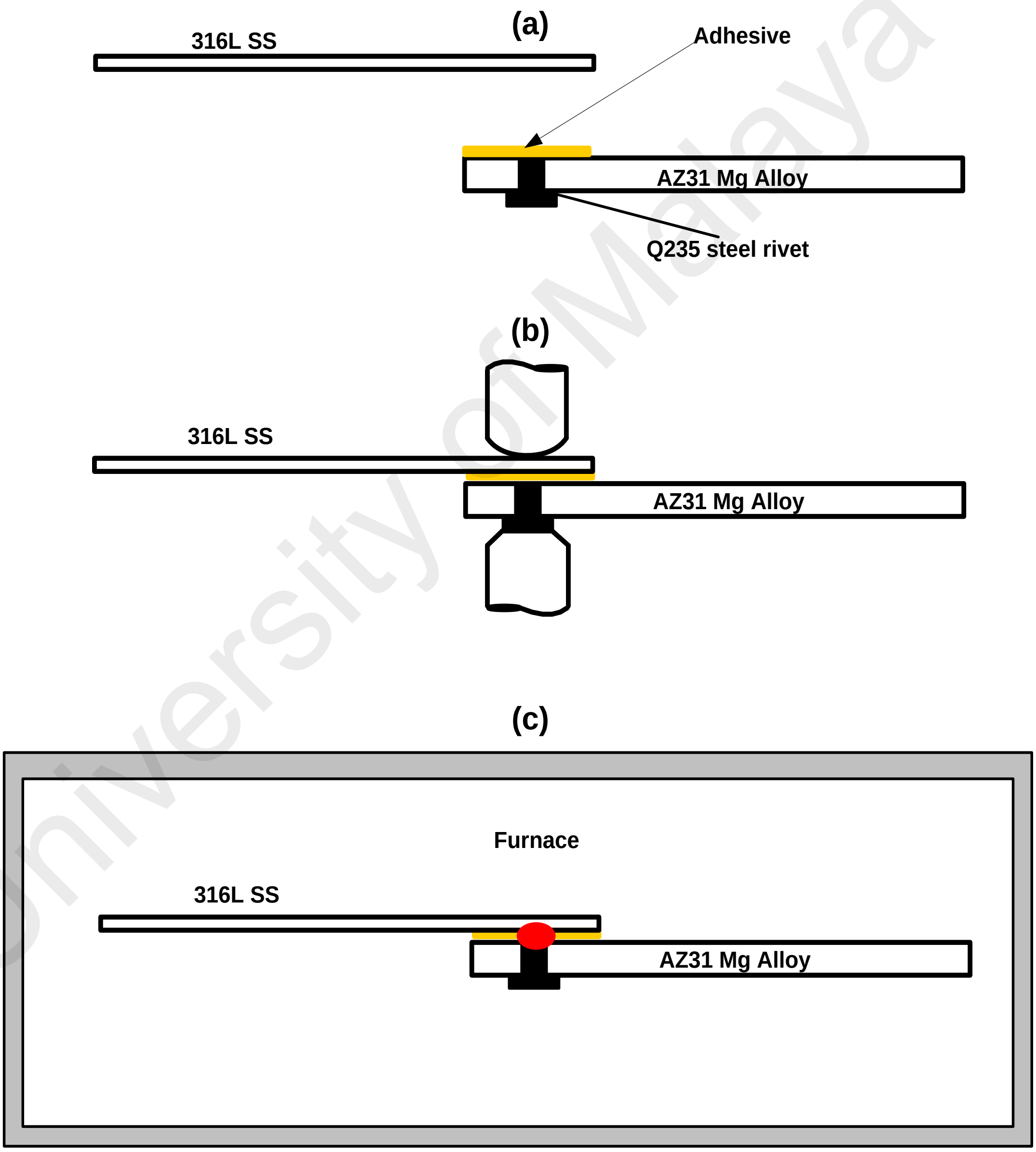

Figure 3.9: Stages of REWB process: (a) adhesive application; (b) assembly and welding; (c) curing

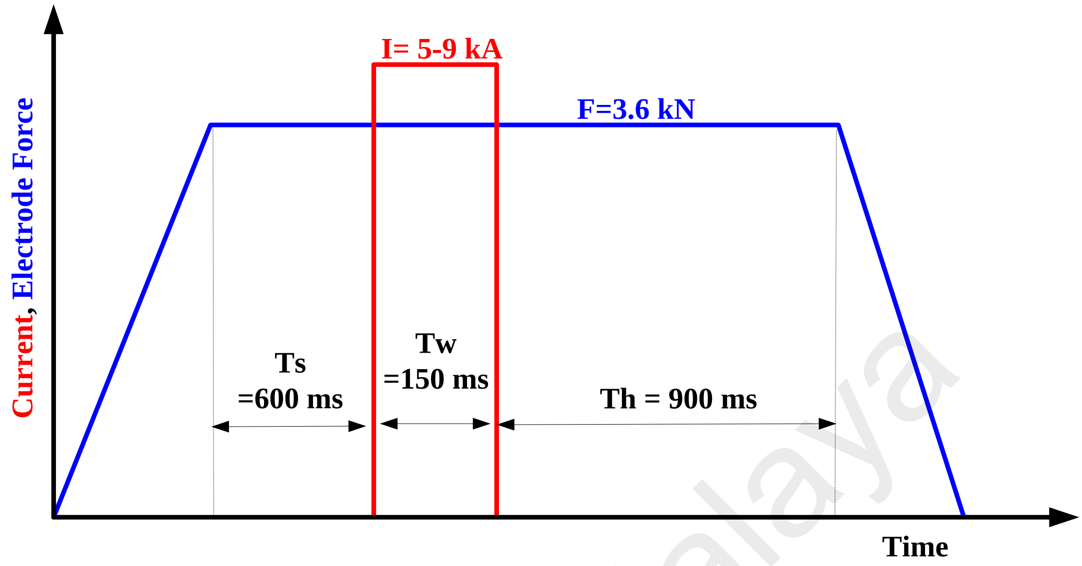

Figure 3.10: Schematic of welding schedule for REWB

3.2.4 Mechanical testing

3.2.4.1 Hardness test

Micro-hardness test is proven to be an effective technique for studying the microstructural gradient across a weldment. Vickers micro-hardness technique was used in this work. The tests were conducted on polished and etched specimens on a Huayin HV-1000A micro-Vickers hardness tester, with a load of 200 g and a dwell time of 15 s using a pyramidal diamond indenter.

For the RSW and RSWB joints, the nugget was found to be formed only in the Mg alloy. Therefore, the hardness indentation path was taken across the Mg nugget, parallel to the Mg alloy/steel interface, as illustrated in Figure 3.11. On the other hand, the nugget was formed at the rivet/ASS interface in REW and REWB processes. Therefore, to better characterize the harness variation of the joints, vertical hardness indentation path was taken, as shown in Figure 3.12. All indentations were spaced adequately in order to prevent any potential effect of strain fields produced by adjacent indentations.

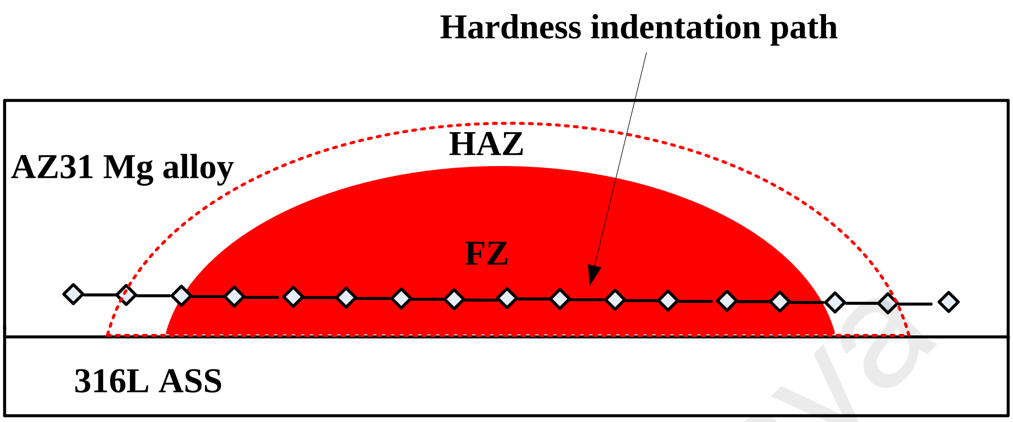

Figure 3.11: Schematic illustration of cross-section and hardness indentation path for RSW and RSWB joints

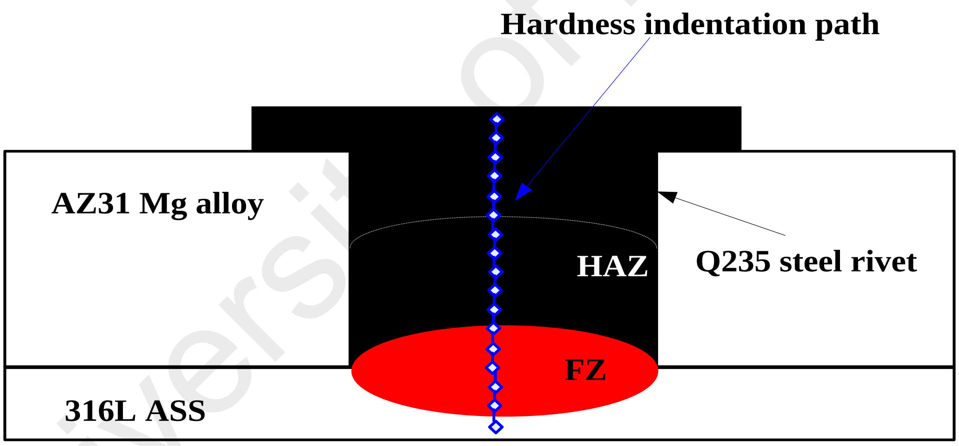

Figure 3.12: Schematic illustration of cross-section and hardness indentation path for REW and REWB joints

In Vickers test, as clearly defined in ASTM E384 Standard (ASTM, 2000), the physical quality of the indenter and the accuracy of the applied load must be controlled to get the correct result. Generally, the impression appears to be square, and the two diagonals have similar lengths. After the load is removed, the two impression diagonals,

d_1 and d_2, as shown in Figure 3.13, were measured with a micrometer built in the attached microscope on the Vickers machine to the nearest 0.1 μm, and then averaged.

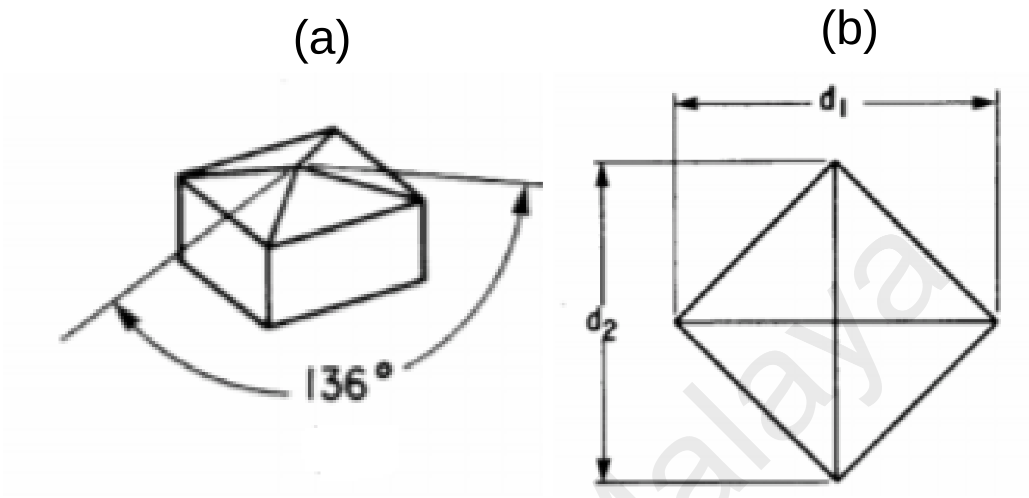

Figure 3.13: Illustration of (a) Vickers indenter; (b) a typical Vickers hardness indentation (Yovanovich, 2006)

The Vickers hardness (H_v) is calculated based on the surface area of the indent using equation 3.1:

$$H_v = \frac{1.854P}{D^2} \quad (3.1)$$

where

P = Applied load

D = Average of the diagonals = $\frac{d_1+d_2}{2}$

3.2.4.2 Tensile shear test

Spot welds are generally designed to bear tensile-shear loads (Marashi et al., 2008b). Therefore, tensile-shear test (TS) is widely used to determine the mechanical performance of spot welds. In this study, the TS test was conducted on a CSS-44100 material test system at a cross-head speed of 2 mm/min. The samples configurations for the test are shown in Figure 3.14. During the test, the gripped zones at the end of the sheets were shimmed in order to avoid the effects of bending moments, as shown in Figure 3.15.

Peak load and the energy absorption were extracted from the load–displacement curves obtained from the test, and the average of three samples was taken for each condition. As illustrated in Figure 3.16, the peak load (the peak point in the load displacement curve) is the maximum load sustained by the joint. The energy absorption is a measure of the ductility of the joint, and is defined as the area of the load-displacement curve up to the peak load. It was calculated using equation 3.2 shown below (Pouranvari et al., 2011) :

$$\text{Energy absorption} = \int_0^{\mathrm{X_{max}}} \mathrm{Pdx} = \sum_{n=1}^{P_{peak}} P\ (n).\,[X(n) - X(n-1)] \qquad (3.2)$$

Where X is displacement, $\mathrm{X_{max}}$ is the displacement at peak load , P is load, $\mathrm{P_{peak}}$ is peak load, and n is the sampled data.

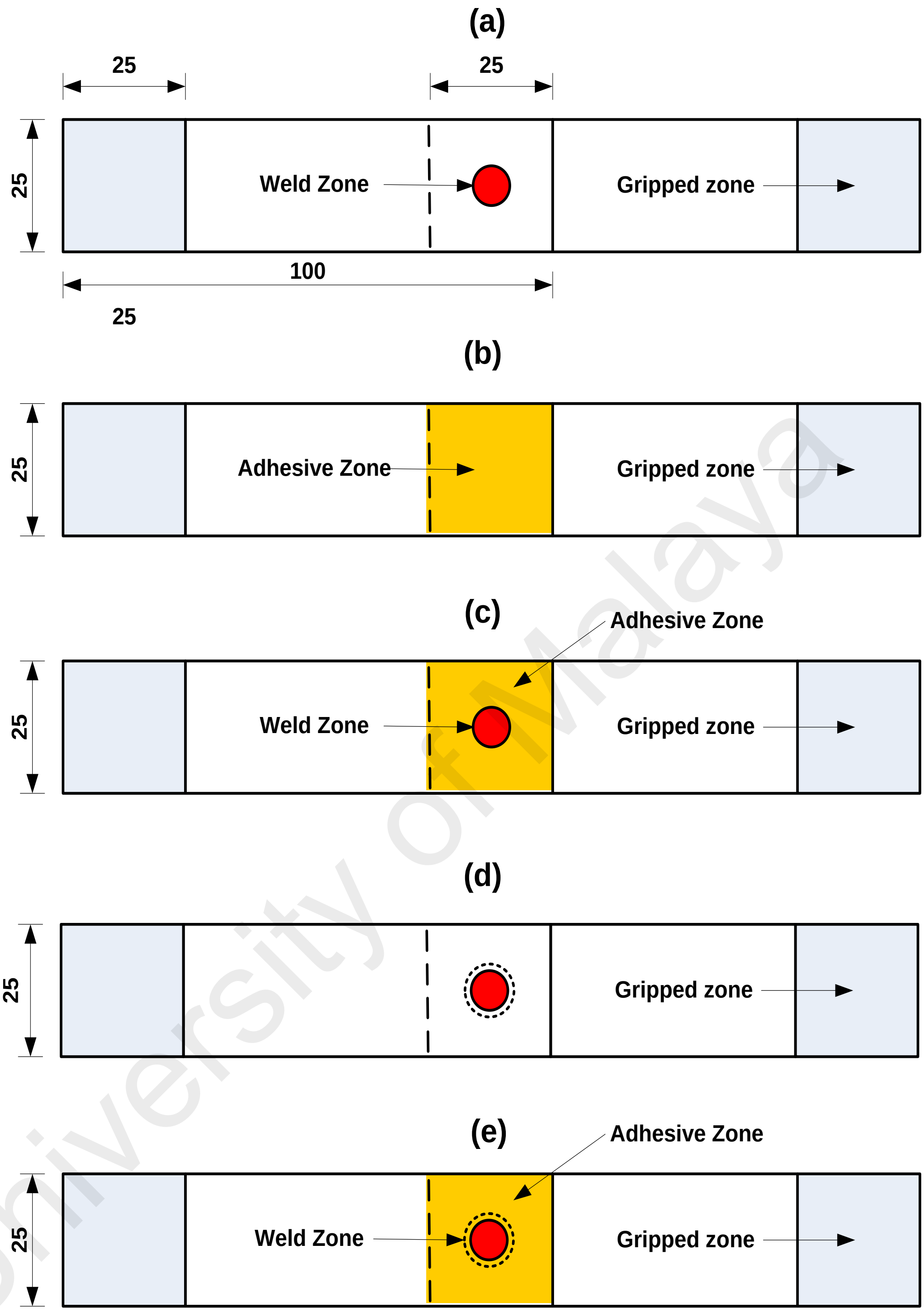

Figure 3.14: Schematic illustration of tensile shear test specimens (a) RSW; (b) AB; (c) RSWB; (d) REW; (e) REWB joints

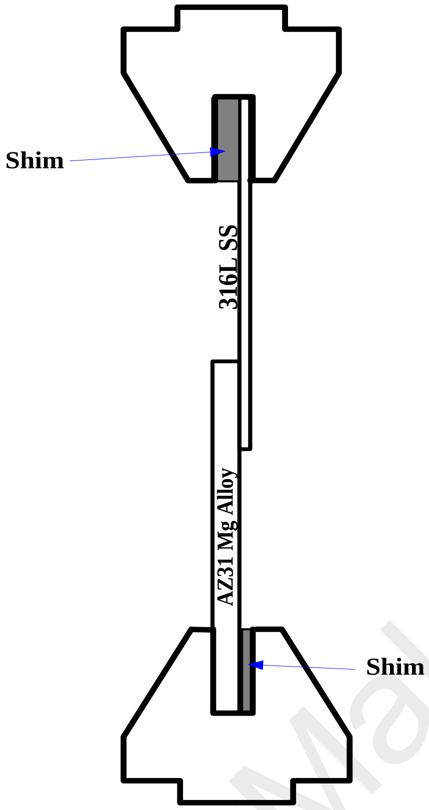

Figure 3.15: Tensile shear test set up

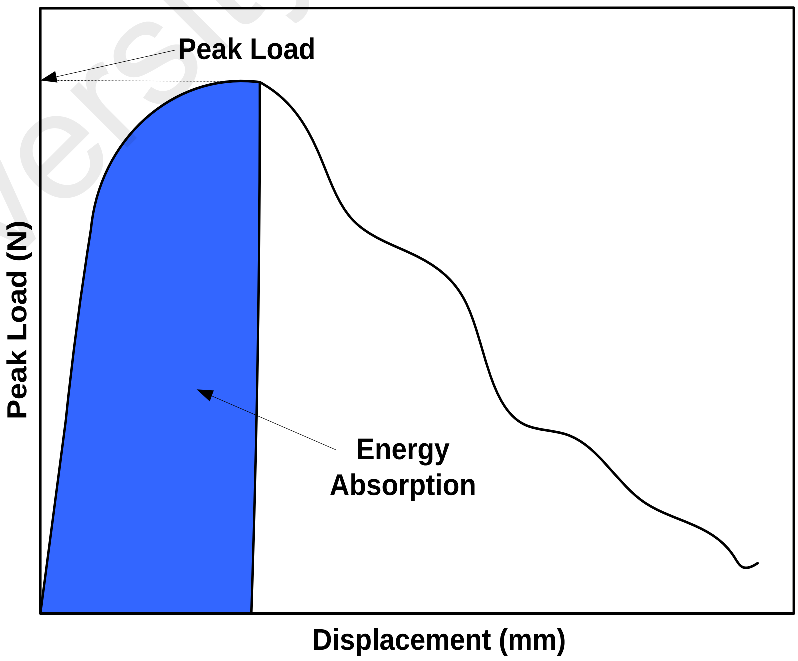

Figure 3.16: Schematic diagram of a load-displacement curve indicating peak load and energy absorption

3.2.5 Fracture surface analysis

Examination of the surfaces of the failed samples after the TS test was conducted using a Hitachi SU1510 scanning electron microscope (SEM) and JOEL JSM7600F FESEM. Furthermore, the fracture surfaces were characterized using EDS point analysis and elemental mapping.

CHAPTER 4: RESULTS AND DISCUSSION

4.1 RSW joints

4.1.1 Microstructural evolution

The typical macrostructure and microstructure of the joints produced by traditional RSW process are shown in Figure 4.1. The joint was found to be produced through welding-brazing mode (Li et al., 2015c), in which the Mg alloy melted and spread on the solid steel. Thus, upon solidification, a nugget was formed only on the Mg side, as indicated by white dotted line in Figure 4.1 a. This is attributable to differences in heat generation and dissipation. Because of its higher electrical resistivity, greater amount of heat would be generated in the steel, which served as a hot anvil to heat the Mg alloy (Xu et al., 2012). As a result of the combined heat flow from the steel side and its own Joule heating, coupled with the fact that it has a lower melting point, the Mg alloy began to melt. Conversely, because of its high thermal conductivity, the Mg alloy would act as a heat sink to the steel. Owing to the heat losses both through the Mg alloy and the water-cooled electrode, the peak temperature reached on the steel side was kept below its melting point (Xu et al., 2012). A similar phenomenon was observed during RSW of Al-5052 alloy/ low carbon galvanized steel (Arghavani et al., 2016), 6008-T6 Al alloy/ H220YDZ100 galvanized high strength steel (Zhang et al., 2011), and 6061-T6 Al alloy/TA1 commercial pure titanium (Li et al., 2015b), with the nugget forming only on the Al side.

As can be seen in Figure 4.1 a, shrinkage pores/cavities are formed in the Mg nugget, close to the Mg/steel interface. The formation of shrinkage porosity and cavities in AZ31 Mg alloy nugget is as a result of its relatively high volume expansion coefficient in liquid at its melting point (Xu et al., 2012). It is influenced by factors such as shrinkage strain, expulsion (Qiu et al., 2014), and hydrogen rejection during solidification (Babu et al., 2012).

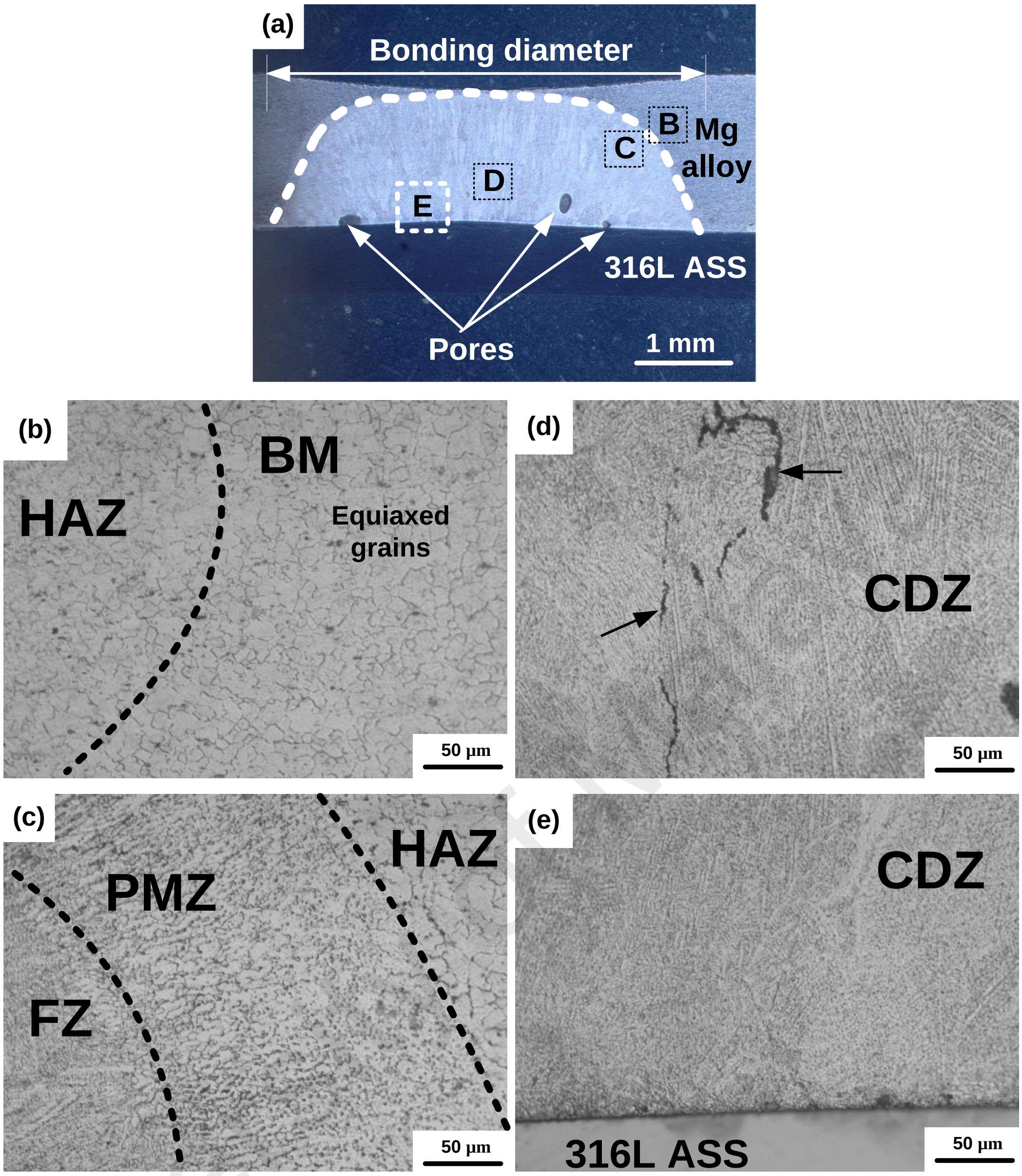

Figure 4.1: Typical macrostructure and microstructures of RSW joint: (a) Macrostructure; and microstructure of (b) region B in (a); (c) region C in (a); (d) region D in (a); (e) region E in (a). The arrows in (d) indicate solidification cracking

As shown in Figure 4.1 d, solidification cracking (indicated by arrows) also occurred in the Mg nugget. High resolution FESEM images taken in the vicinity of the crack revealed the presence of white particles in the inter-dendiritic regions (Figure 4.2). EDS analysis indicate that the composition of point 1 is 97.98 wt. %Mg and 2.02wt %Al and that of point 2 is 82.09 wt. % Mg, 14.34 wt. % Al, and 3.57 wt. % Zn. Based on Mg-Al phase diagram, point 1 is α-Mg while point 2 is basically α-Mg + β-$Mg_{12}Al_{17}$. Thus, the white particles are likely β-$Mg_{12}Al_{17}$ particles. This is in agreement with the observations of Zhu et al. (2010) and Niknejad et al. (2014). These particles were formed by eutectic reaction as a result of non-equilibrium solidification (Niknejad et al., 2014). Because of the low eutectic temperature (Yuan et al., 2015), liquid films are formed between the dendrites during solidification, which weaken the nugget and lead to cracking under the stresses developed during cooling.

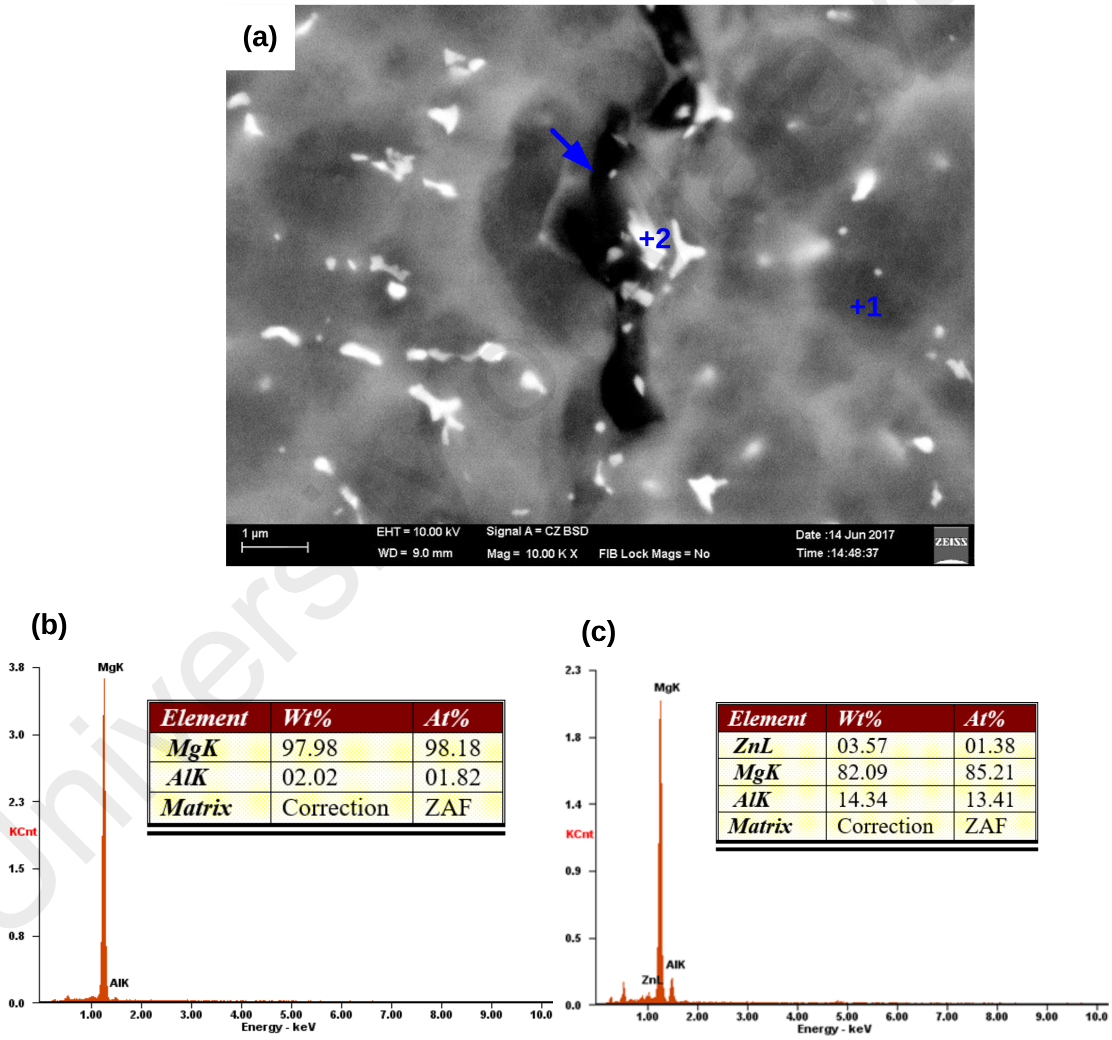

Figure 4.2: Solidification cracking (a) FESEM images in the crack vicinity; (b) EDS spectrum of point 1 in (a); (d) EDS spectrum of point 2 in (a). Arrow in (a) indicate solidification cracking

Referring to Figures 4.1 b and c, the microstructure of the joint can be divided into four zones, namely, the base metal (BM), heat affected zone (HAZ), partially melted zone (PMZ), and the fusion zone (FZ). These four zones were also identified by Behravesh et al. (2011) while studying the RSW of similar AZ31-H24 Mg alloy. The microstructure of the BM, as shown in Figure 4.1b, consisted of equiaxed grains. The PMZ, which is located adjacent to the FZ (Figure 4.1 c), reached a peak temperature that is between the solidus and liquidus temperatures of the AZ31 Mg alloy. Therefore, the grain boundaries would undergo liquation because of their higher Al content and lower melting point (Behravesh et al., 2011).

The solidification mode of an alloy could change from columnar dendritic to equiaxed dendritic (columnar-to-equiaxed transition, CET), depending on the ratio of temperature gradient (G) to solidification growth rate (R). A low G/R value implies a higher degree of constitutional supercooling and enhanced CET (Kou, 1987). During RSW, solidification begins epitaxially at the nugget edges because of their proximity to the water-cooled electrodes, leading to the formation of CDZ at the edges. However, as the solidification continues, the value of G/R drops because of the movement of the solid–liquid interface away from the electrodes, the release of fusion heat from weld pool as well as the reduced cooling effect of the electrodes (Pouranvari et al., 2015a). The microstructure at the edges (Figures 4.1 c and e) and center (Figure 4.1 d) of the FZ consisted of columnar dentric zone structure (CDZ). This is different from what was observed during RSW of AZ31Mg alloy/ hot-dip galvanized HSLA (Xu et al., 2012), in which a columnar dendritic zone (CDZ) and an equiaxed dendritic zone (EDZ) were obtained. This could be attributed to the fact that the stainless steel (which possesses lower thermal conductivity and higher electrical resisistivity than carbon steel) restrained heat loss from the nugget and lowered the cooling rate, keeping G/R ratio in the liquid nugget relatively high level. A similar phenomenon was observed by Li et al. (2015c) while studying Al/Ti dissimilar RSW.

4.1.2 Joint interface characteristics

To further understand the joining mechanism and to determine whether inter-diffusion of the alloying elements across the interface has occurred, EDS line scan of the main alloying elements was conducted across the interface, and the results are shown in Figure 4.3.

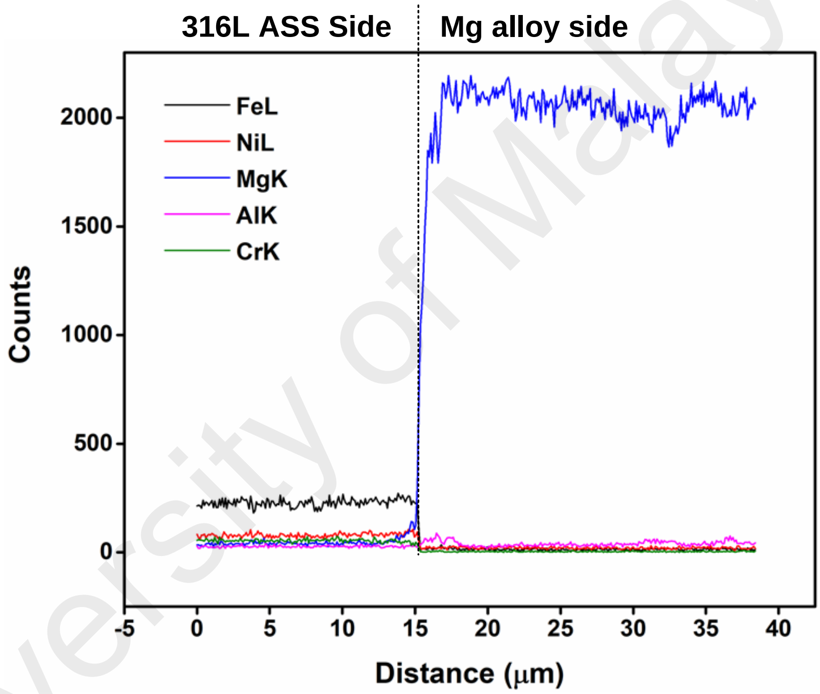

Figure 4.3: Results of EDS line scan across the RSW joints interface

Referring to Figure 4.3, from the steel side to the Mg alloy side, the concentration of Fe, Ni, and Cr decreased sharply across the interface while that of Mg increased sharply. However, some Al diffused from the Mg alloy into the steel side. This is seen more clearly in the EDS elemental mapping conducted across the interface (Figure 4.4). This suggests that there was no interfacial reaction between the Mg and Fe, despite the fact that the Mg alloy melted during the welding process. This can be explained on the basis of the Fe-Mg phase diagram (Figure 4.5), which clearly shows that Mg and Fe could not react with each other to form a reaction layer or IMC. Thus, the RSW joint is not a metallurgical joint. It is a mechanical joint formed through welding-brazing, involving a reaction between liquid Mg alloy and solid ASS.

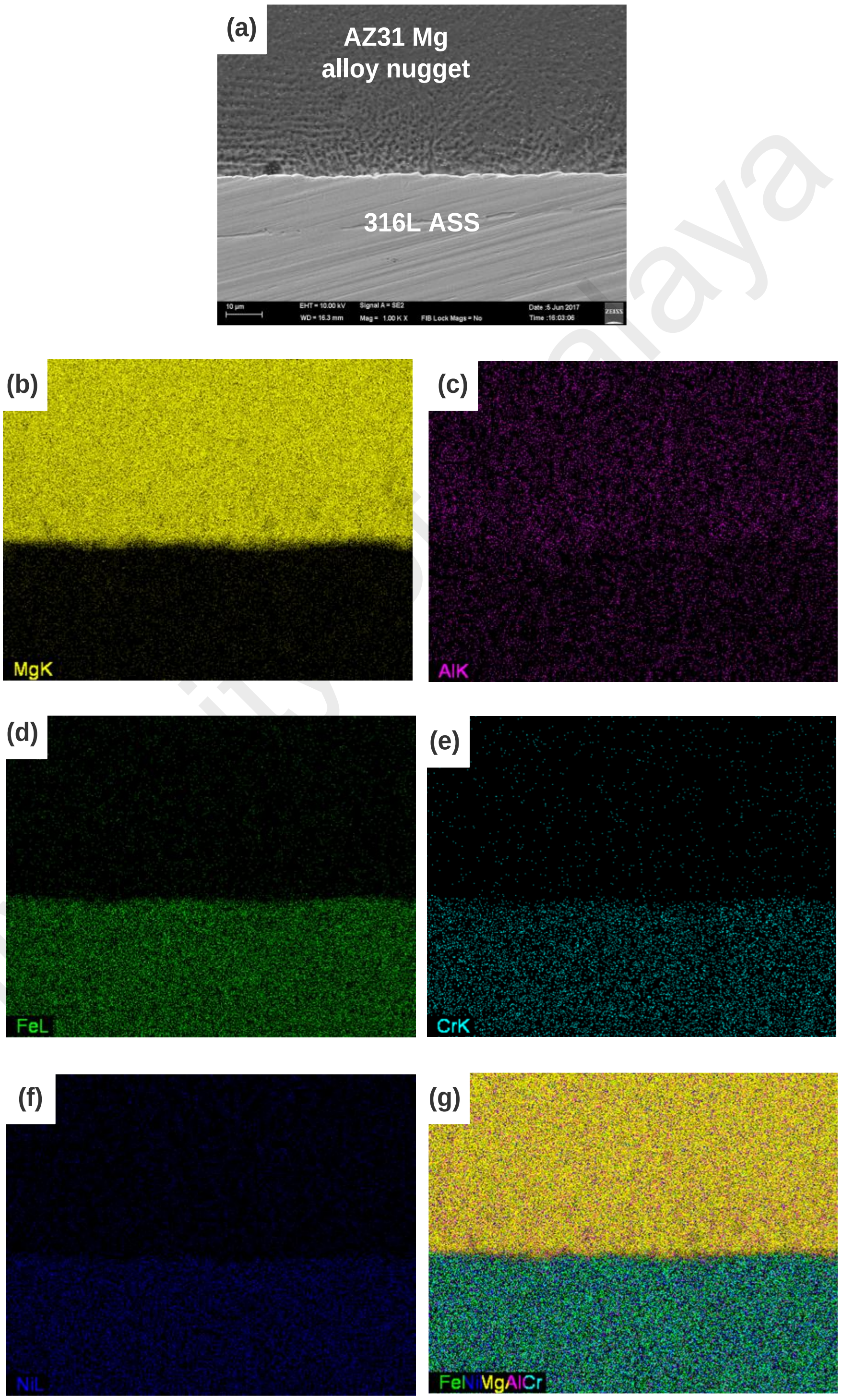

Figure 4.4: EDS mapping across RSW the joint interface (a) secondary image ; (b) Mg; (c) Al; (d) Fe; (e) Cr; (f) Ni elements; and (g) overlay

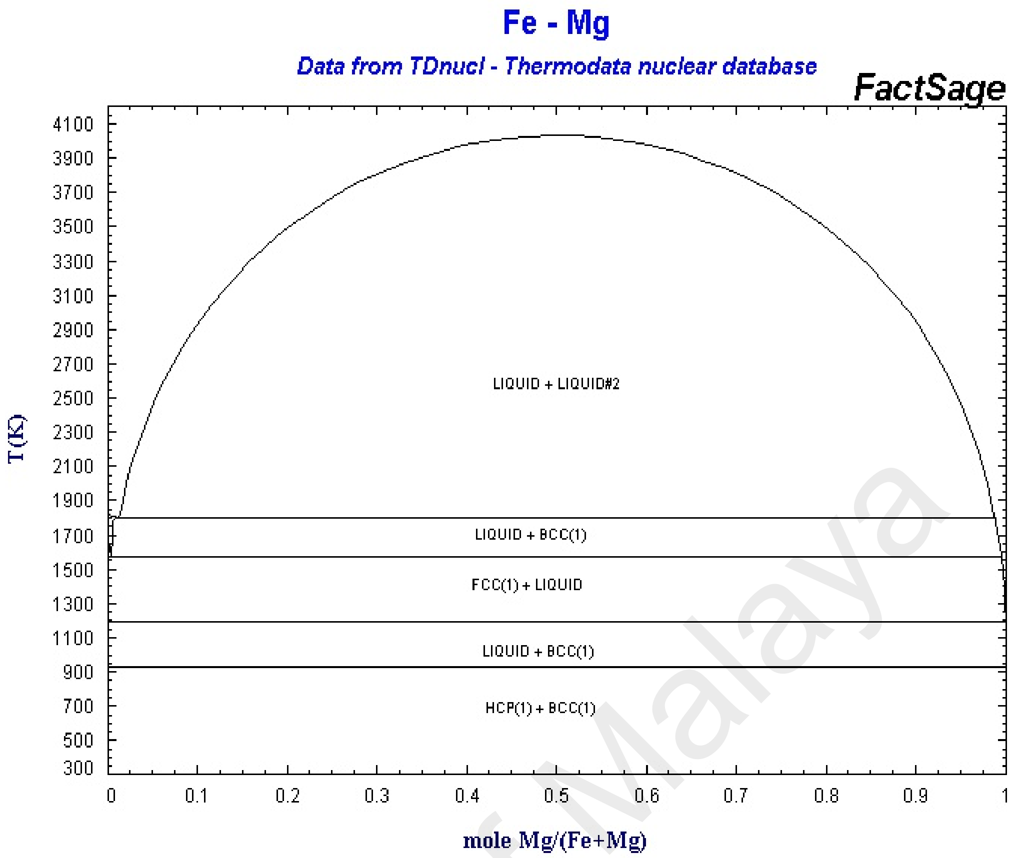

Figure 4.5: Fe-Mg phase diagram
(http://www.crct.polymtl.ca/fact/phase_diagram.php?file=Fe-Mg.jpg&dir=TDnucl)

4.1.3 Hardness characteristics

The typical hardness profile of the RSW joint (Figure 4.6) indicates that there is minimal hardness variation across the weldment. The average hardness of the BM and FZ was found to be 58 HV and 60V, respectively. Behravesh et al. (2011) also reported that the hardness in the FZ and BM of AZ31 Mg alloy spot welds are almost the same. The slightly higher hardness of the FZ is likely due to the formation of fine columnar crystals, as shown in Figures 4.1 c-e. Compared with the BM, a slight hardness reduction occurred in the HAZ, which is attributed to the occurrence of slight grain growth, as shown in Figure 4.1 b.

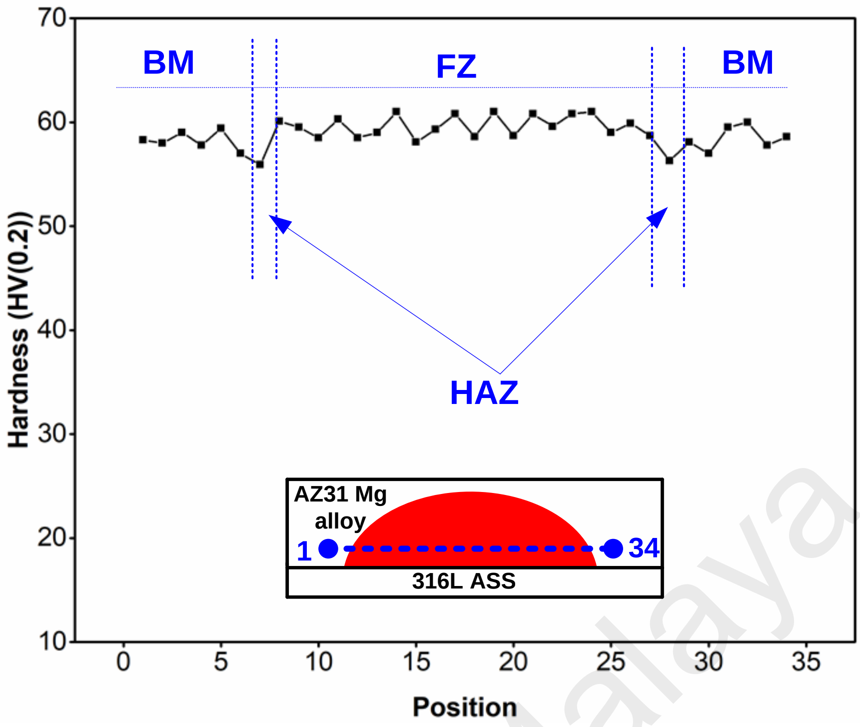

Figure 4.6 : Hardness profile of RSW joint

4.1.4 Tensile-shear performance

The mechanical properties of spot welds depends largely on the nugget size (width of the FZ across the sheet/sheet interface) (Goodarzi et al., 2009). Referring to Figure 4.1a, since the RSW joint was produced through welding-brazing mode, the term "bonding diameter" is used to describe the nugget size, as suggested by Li et al. (2015c). The bonding diameter was measured from the fracture surfaces after tensile-shear test.

Figure 4.7 shows the bonding diameter, peak load, and energy absorption of the RSW joint as a function of welding current. By increasing the welding current from 6 to 18 kA, the bonding diameter increased continuously from 4.1 to 9.1 mm due to increase in volume of melted metal. The average peak load and energy absorption increased from 0.65 kN and 0.09214 J, respectively, at a welding current of 6 kA to a maximum of 2.23

kN and 1.1367 J, respectively, at welding current of 14 kA. This is as a result of increase in bonding diameter.

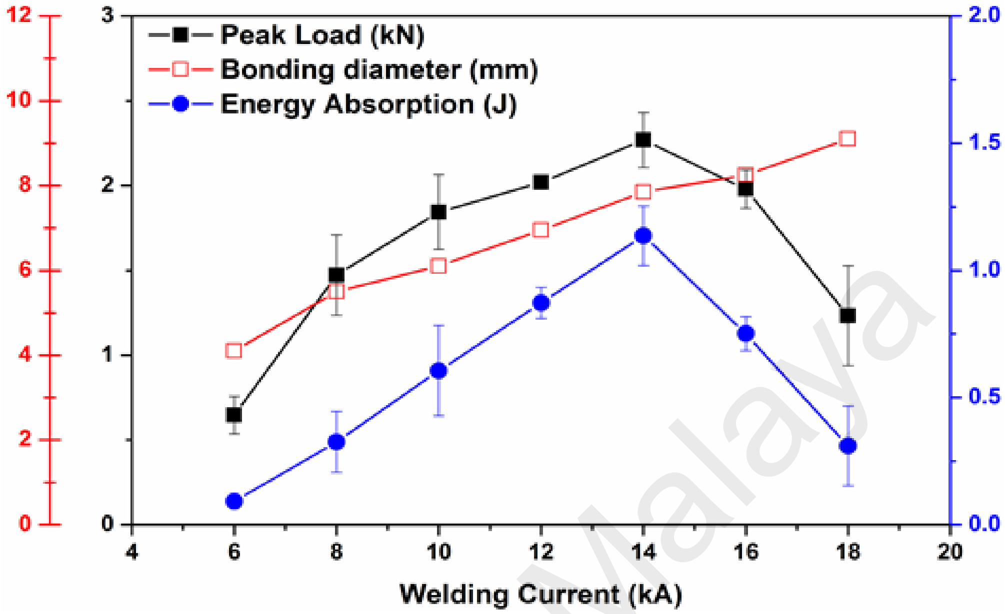

Figure 4.7 : Effect of welding current on the bonding diameter, peak load, and energy absorption of RSW joints

However, with further increase in welding current, both the peak load and energy absorption decreased, despite the increase in bonding diameter. Examination of the fracture surface of the joints produced with welding current above 14 kA revealed heavy expulsion (splashing of molten metal). Therefore, the reduced joint strength could be associated with expulsion and factors related to expulsion, such as porosity and excessive electrode indentation (Pouranvari et al., 2008). A similar phenomenon of decreased peak load and energy absorption despite increased or constant nugget size was also observed during RSW of similar Mg alloys (Lang et al., 2008), ASS steels (Kianersi et al., 2014a), and uncoated low carbon steel (Pouranvari et al., 2008).

Overall, the mechanical performance of the RSW joints, especially its energy absorption is poor. The maximum peak load and energy absorption of the joints is 2.23 kN and 1.136 J, respectively.

4.1.5 Failure mode

Failure mode qualitatively indicates the mechanical performance of spot welds. Spot welds generally fail in two distinct modes, i.e., interfacial failure (IF) and pullout failure (PO) modes. As schematically illustrated in Figure 4.8 a, in IF mode, the two sheets are separated apart by crack propagation via the FZ (path A). In PO mode, the nugget is withdrawn from one of the sheets by crack propagation through the FZ/HAZ (path B), HAZ (path C) or BM (path D). Although, PO is the most preferred mode, failure occurs in the mode which requires less load (Pouranvari, 2017).

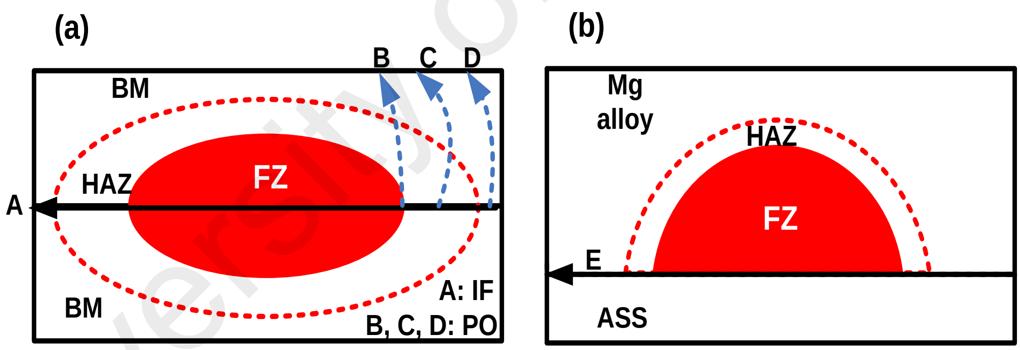

Figure 4.8: Schematic illustrations of the main failure modes of resistance spot welds

In the present study, all the RSW joints, irrespective of the welding current, failed at the Mg nugget/steel sheet interface (Path E in Figure 4.8 b). This kind of failure mode is different from the IF mode commonly observed during tensile-shear test of spot welds (path A in Figure 4.8 a). However, for the sake of simplicity, it also referred to as IF mode. Since all the samples failed in IF mode, the increase in peak load with increased welding current is not because of difference in failure mode. It is as a result of the increased interfacial resistance to shearing due to increased bonding diameter (Pouranvari et al., 2008).

The typical load-displacement curve for RSW joints is displayed in Figure 4.9. The peak point indicates the crack propagation point via the Mg/ASS interface. It is seen that the joints failed abruptly after reaching the peak load. This accounts for the low energy absorption of the RSW joints. This kind of failure mode is detrimental to vehicle crashworthiness.

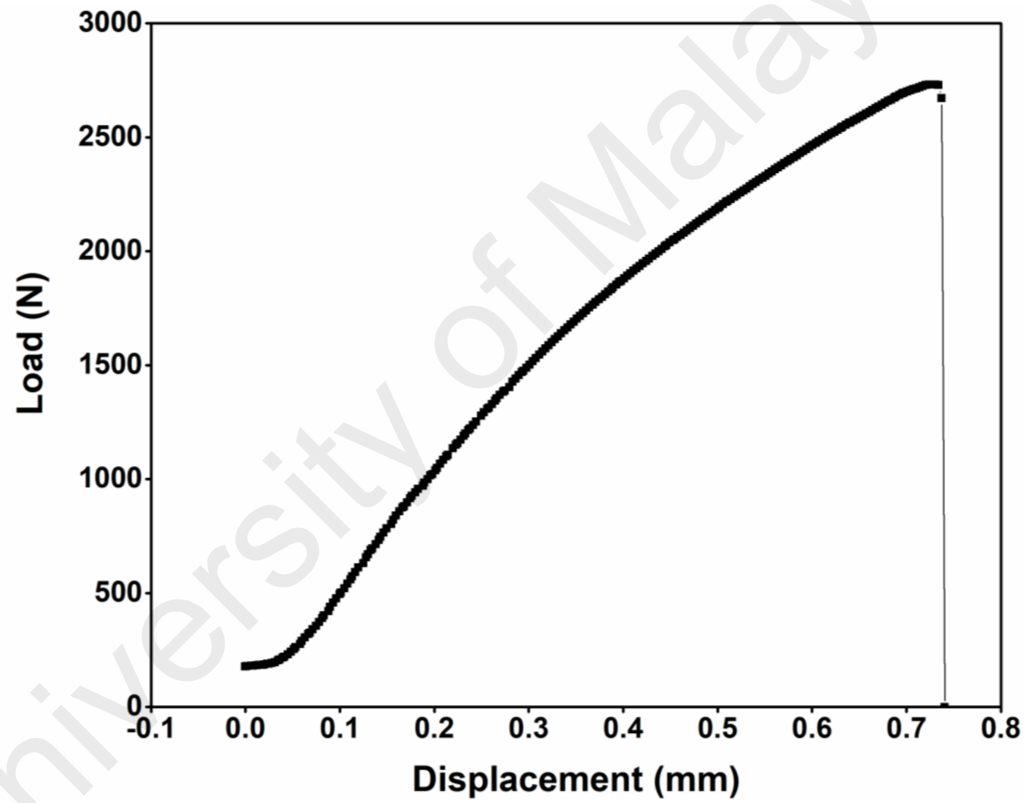

Figure 4.9 : Typical Load-displacement curve for RSW joints

The fracture surface of the RSW joint on the Mg side is shown in Figure 4.10. Shrinkage cracking/cavities, several small voids, and expulsion are observed in the nugget, indicating relatively poor joining. Liu et al. (2010b) also observed numerous small voids on the fracture surface of Mg alloy, while investigating the joining mechanism of AZ31B Mg alloy/ zinc-coated DP600 resistance spot welds. The formation of these small voids is likely due to trapped gases between the sheets (Liu et al., 2010b).

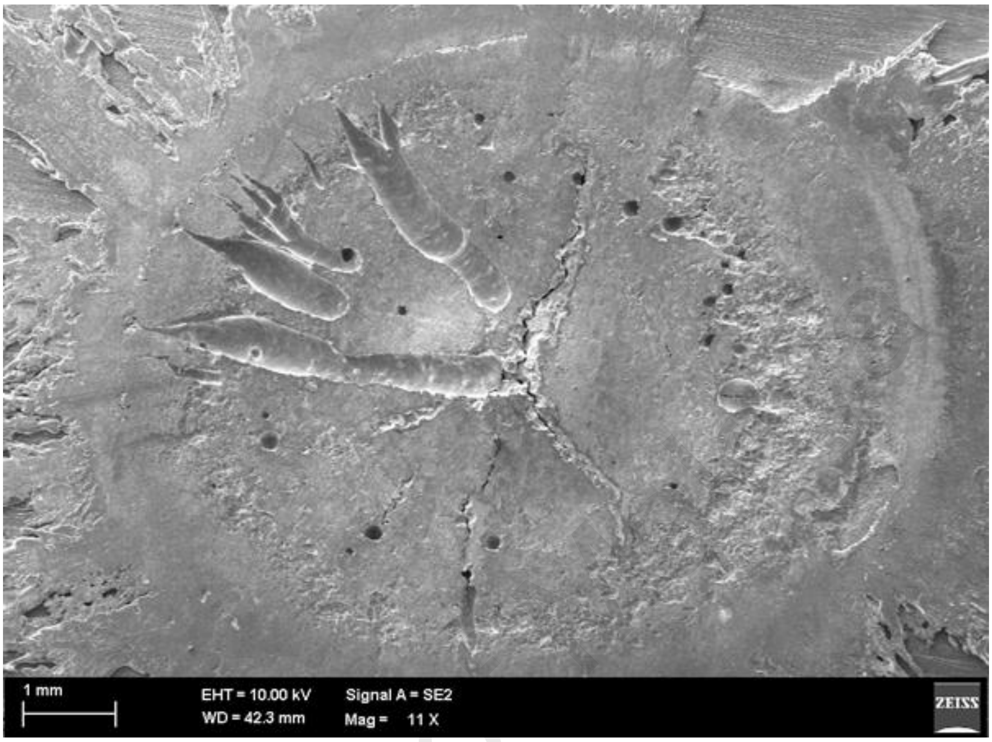

Figure 4.10: Fracture surface of Mg side of the RSW joint

The fracture surface of the ASS side is shown in Figure 4.11. Observation of the fracture surface at higher magnification (Figure 4.11 c) shows that the surface exhibits the surface morphology of the ASS BM (Figure 14 b), with some residual AZ31 Mg alloy, as confirmed by EDS mapping (Figure 4.11 d-h). This further confirmed that the Mg alloy melted and braze-welded to the steel which remained unmelted. The presence of residual Mg alloy at some locations on the steel fracture surface indicates that the fracture path largely followed the Mg/steel interface, and occasionally through the Mg FZ.

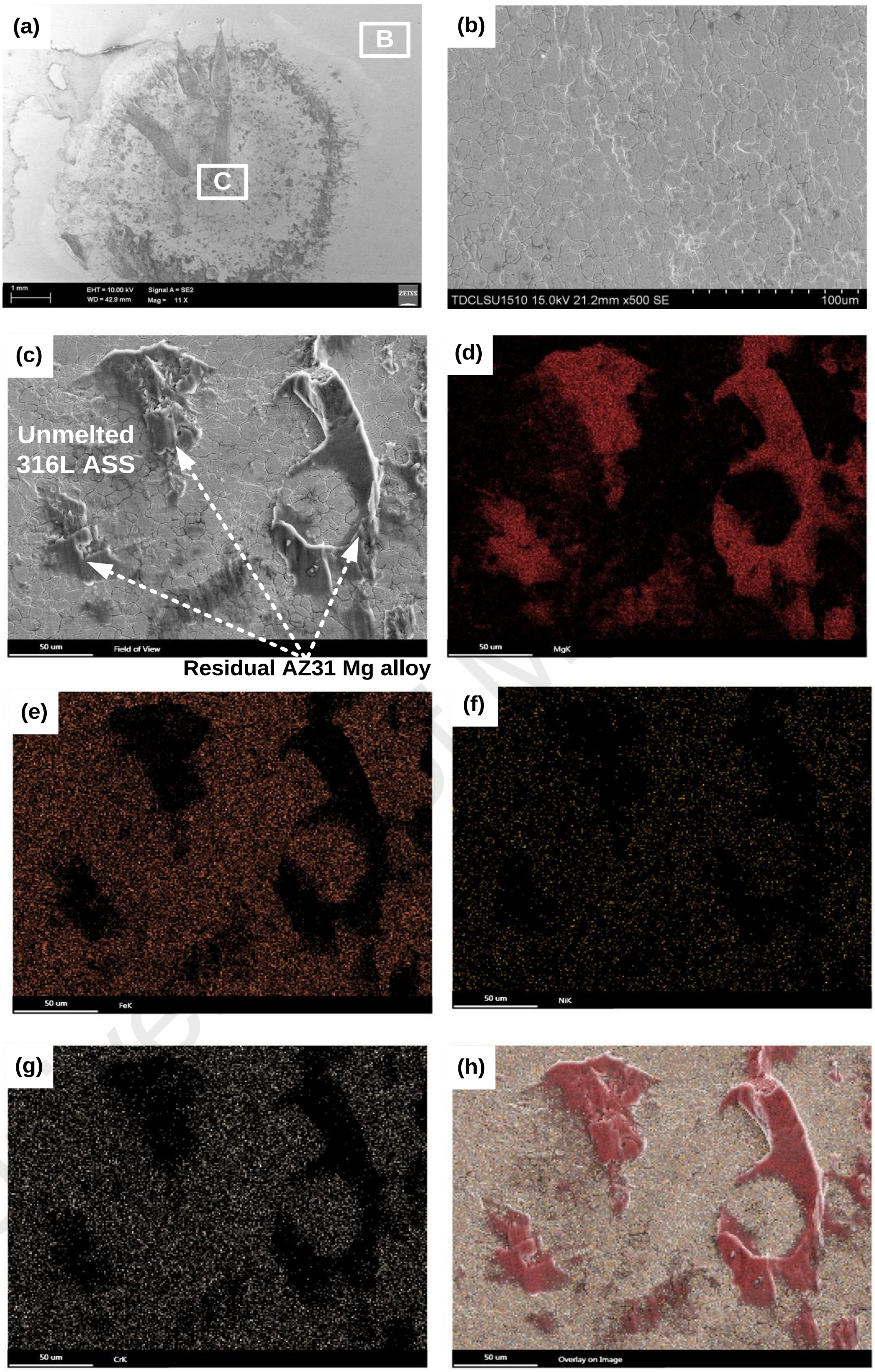

Figure 4.11 : Fracture surface of the ASS side of the RSW joint (a) macroscopic morphology; (b) higher magnification of region B in (a); higher magnification of region C in (a); (d) distribution of Mg; (e) distribution of Fe; (f) distribution of Ni; (g) distribution of Cr; (h) overlay distribution of Mg, Fe, Ni and Cr

4.2 RSWB joints

4.2.1 Macrostructure and microstructure

The typical macrostructure and microstructure of the RSWB joints are shown in Figure 4.12. As shown in Figure 4.12 a, the joint can be divided into two main zones, the weld zone and adhesive zone. The microstructural evolution of the weld zone is similar to that of RSW joints. The weld zone was also produced through welding-brazing mode and the nugget was formed only in the Mg alloy. As shown in Figure 4.12b, a HAZ, PMZ, and FZ were also identified. Furthermore, the microstructure in both the edge and center of the nugget consisted of CDZ. This microstructural evolution has already been discussed in section 4.1.1.

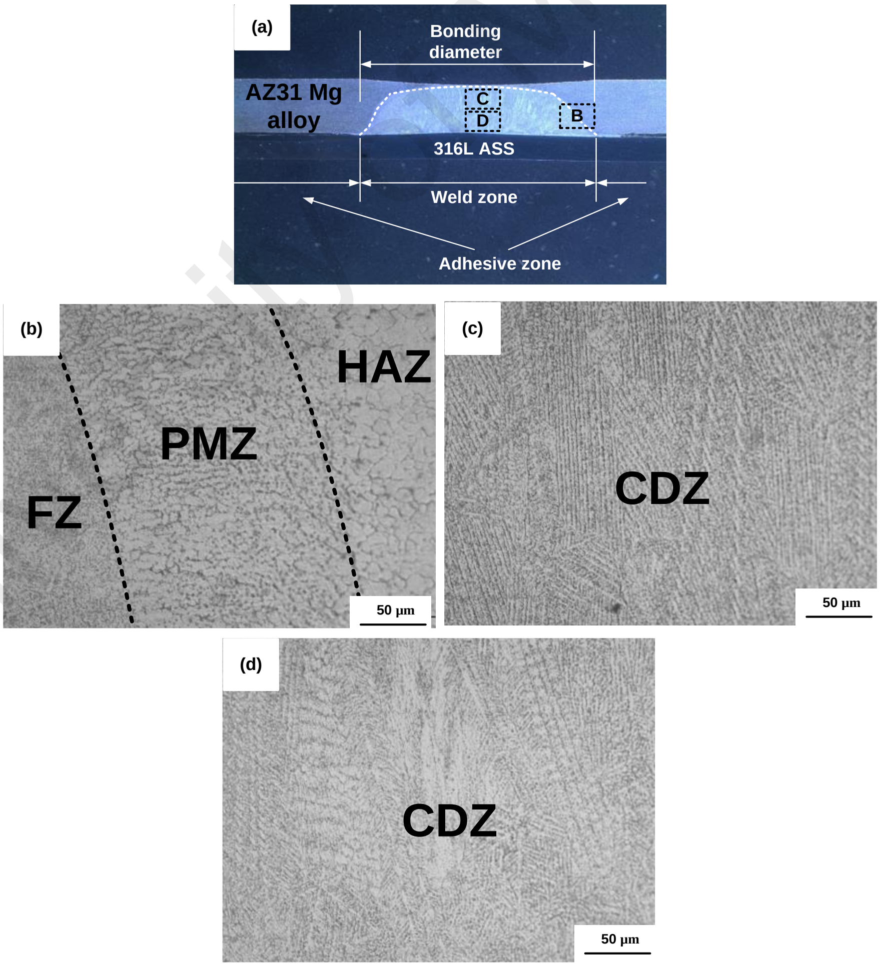

Figure 4.12: (a) Typical macrostructure of RSWB joint; microstructure of (b) region B in (a); (c) region C in (a); (d) region D in (a)

However, unlike in the RSW joints, solidification cracking and shrinkage porosity were not observed in the nugget of the RSWB joints up to the optimum welding current, where the maximum peak load and energy absorption were obtained. A similar observation was reported by Xu et al. (2012), while investigating the microstructure of resistance spot welded and weld bonded AZ31B-H24 Mg alloy/hot-dip galvanized HSLA steel joints. The absence of solidification cracking in the RSWB joints could be attributed to its lower cooling rate compared with that of the RSW process.

The heat generation in RSW is based on Joules law (equation 2.1). It is evident from this equation that the welding current, time, and resistance have influence on the heat input. However, the influence of the welding current is much greater, i.e., square vs linear dependence. The optimum welding parameters, where the maximum tensile shear performance was obtained, were found to be 14 kA, 200 ms , and 3.6 kN for RSW and 12 kA, 100ms, and 3.6 kN for RSWB. Therefore, although the adhesive layer in RSWB increased the dynamic resistance, more heat would be generated in the RSW joints at optimum welding parameters. This higher heat generation would result in faster cooling rate according to Newton's law of cooling (equation 4.1) (Burmeister, 1993; Xu et al., 2012):

$$\dot{Q} = \frac{dQ}{dt} - hA\,\Delta\theta\,(t) = hA\,(\theta_{env} - \theta(t)) \tag{4.1}$$

Where $\dot{Q}$ is the change in heat energy with respect to time *t*, h is the heat transfer coefficient, *A* is the surface area, θ_{env} is the temperature of the environment, and θ is the temperature of the body.

Based on this equation, the rate of heat loss from a body is proportional to the temperature difference between the body and its environment. Therefore, faster cooling rate would be experienced in the RSW than in RSWB joints at optimum welding parameters due to the higher heat input, leading to cracking.

4.2.2 Joint interface characteristics

The typical cross-section macrostructure and interface morphologies of the RSWB joint are shown in Figure 4.13. The interface morphology of the center of weld zone (Figure 4.13 b) is similar to that of RSW (4.13 c) joints, with no visible adhesive at the Mg/steel interface. However, as shown in Figure 4.13 d, adhesive was clearly observed at the edge of the weld zone, indicating that the uncured adhesive was squeezed out of weld zone and pushed towards the weld edge during the RSWB process. Thus, the RSWB joint could be divided into two zones, namely, weld zone and adhesive zone.

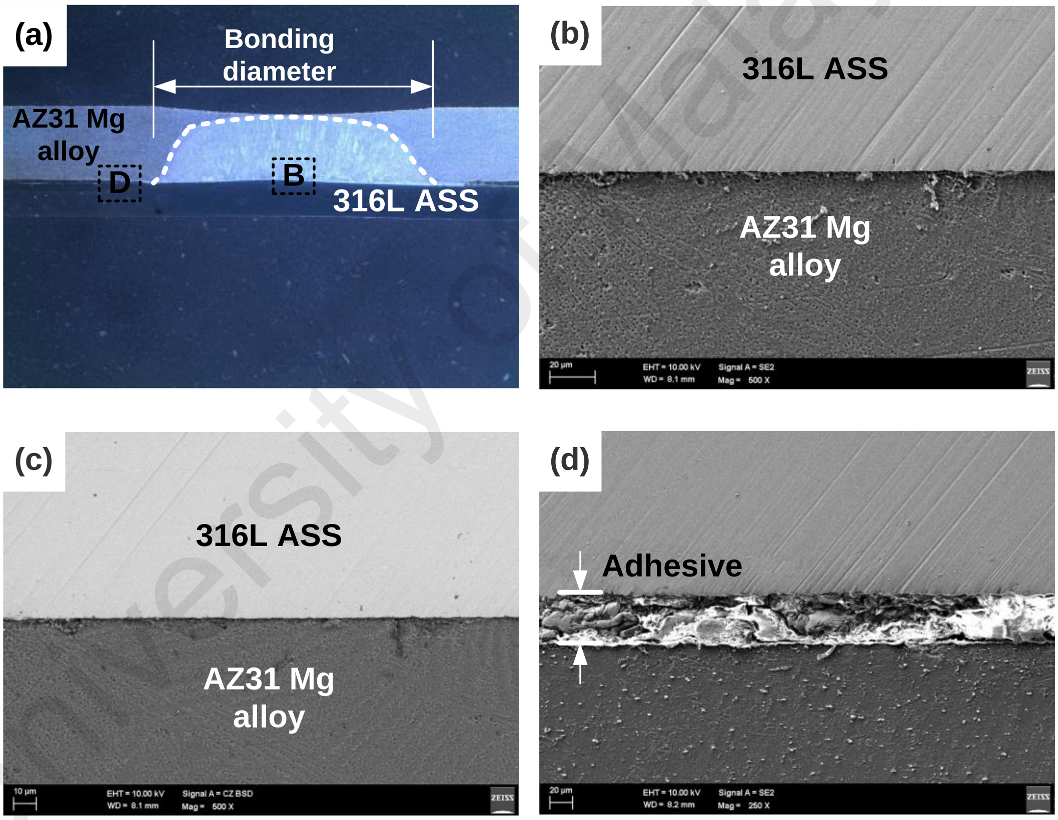

Figure 4.13: Typical macrostructure and interface morphology of the RSWB joints (a) macrostructure; (b) higher magnification of region B in a;(c) interface morphology at nugget center of RSW (d) higher magnification of region D in a

A similar phenomenon was observed during RSWB of DP590/ DP780 steels (Sam & Shome, 2010), ultrasonic spot weld bonding (USWB) of AZ31B-H24 Mg alloy/ hot-dip-galvanized mild steel (Lai & Pan, 2015), USWB of Al/Mg alloys (Feng et al., 2016a), and laser spot weld bonding (LSWB) of Al/Mg alloys (Liu et al., 2007). The disappearance of adhesive from the weld zone can be explained as follows.

Under the influence of the electrode pressure and welding heat, the uncured adhesive, because of its fluidity and viscosity, would deform and flow away from the weld zone towards the natural notch (slight gap) that exists between sheets during RSW, as schematically illustrated in Figure 4.14.

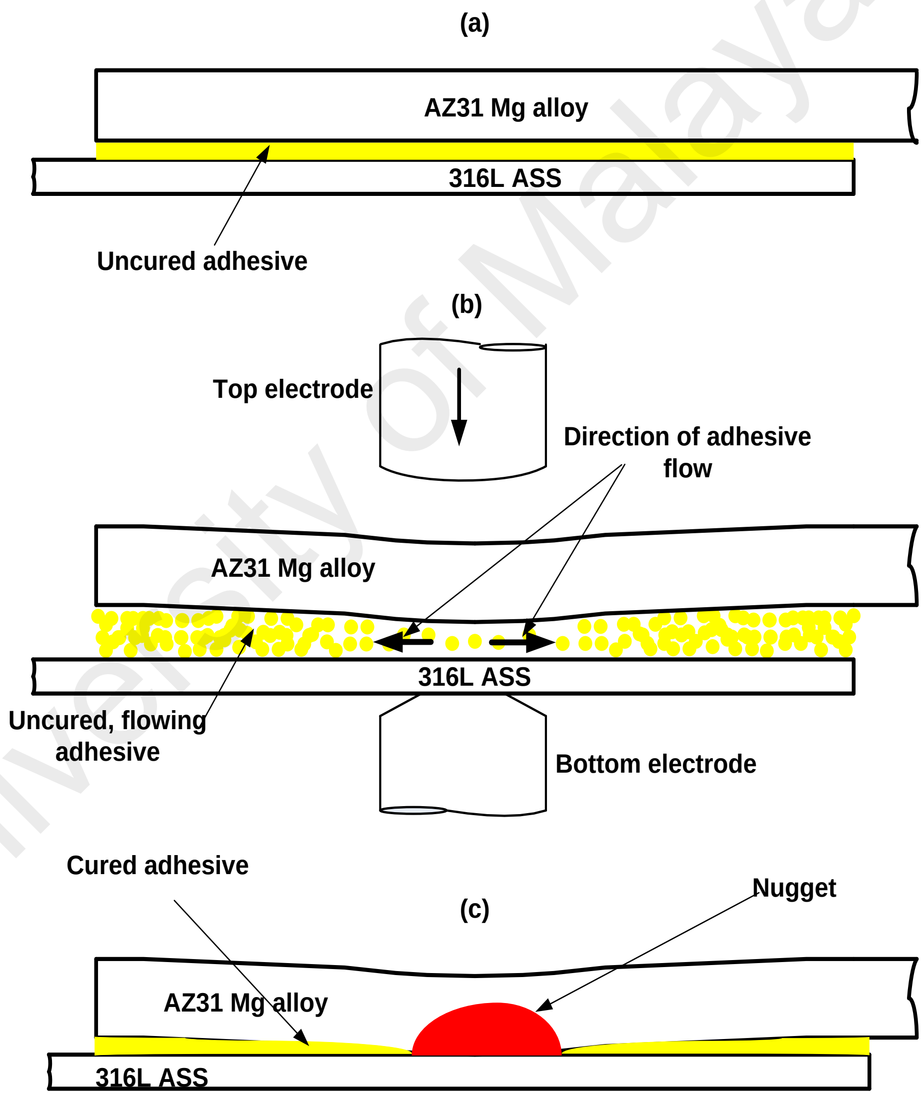

Figure 4.14: Schematic illustration of adhesive flow during RSWB (a) adhesive application and assembly; (b) RSWB process; (c) welded and cured joint

As illustrated in Figure 4.14c, the average thickness of the adhesive was found to increase progressively from the natural notch towards the edges of the overlap area. This is because of the reduction of the intensity of the electrode pressure and heat with increasing distance from the center of the weld zone. Another possible reason for the disappearance of the adhesive in the weld zone is the poor heat durability of the adhesive (Liu et al., 2007; Sam & Shome, 2010), which makes it decompose under the welding heat and escape in the form of gas.

To analyze the inter-diffusion of elements across the ASS/Adhesive/Mg alloy interfaces of the adhesive zone, EDS line scan analysis was conducted across the interfaces at the edge of the weld zone (region D in Figure 4.13 a), and the results are shown in Figure 4.15. It is seen that the contents of Fe, Cr, and Ni elements decreased sharply at the ASS/adhesive interface, indicating that they did not diffuse across the interface. This is probably because the steel has not melted during the RSWB process. An apparent segregation of O element is observed at the center of the adhesive, which is expected because the epoxy adhesive has high amount of oxygen. It is also seen that Mg element diffused from the Mg alloy side across the Mg alloy/adhesive interface and segregated at the center of the adhesive, where there is high concentration of oxygen. This is probably because of its high affinity for oxygen. A somewhat similar phenomenon was displayed by the Al element. However, the Al peaks are very low because of its minimal content in the Mg alloy compared to that of Mg element. A sharp increase in the Al element peak and a sharp decrease in the Mg element peak are observed at a point on the Mg alloy side. This is likely because the line scan crossed β-$Mg_{17}Al_{12}$ phase, causing a decrease in Mg content and increase in Al content (Li et al., 2013). The aforementioned observations are confirmed and seen more clearly in the EDS elemental mapping conducted across the interfaces (Figure 4.16). High concentrations of Mg and O are clearly seen at the center of the adhesive.

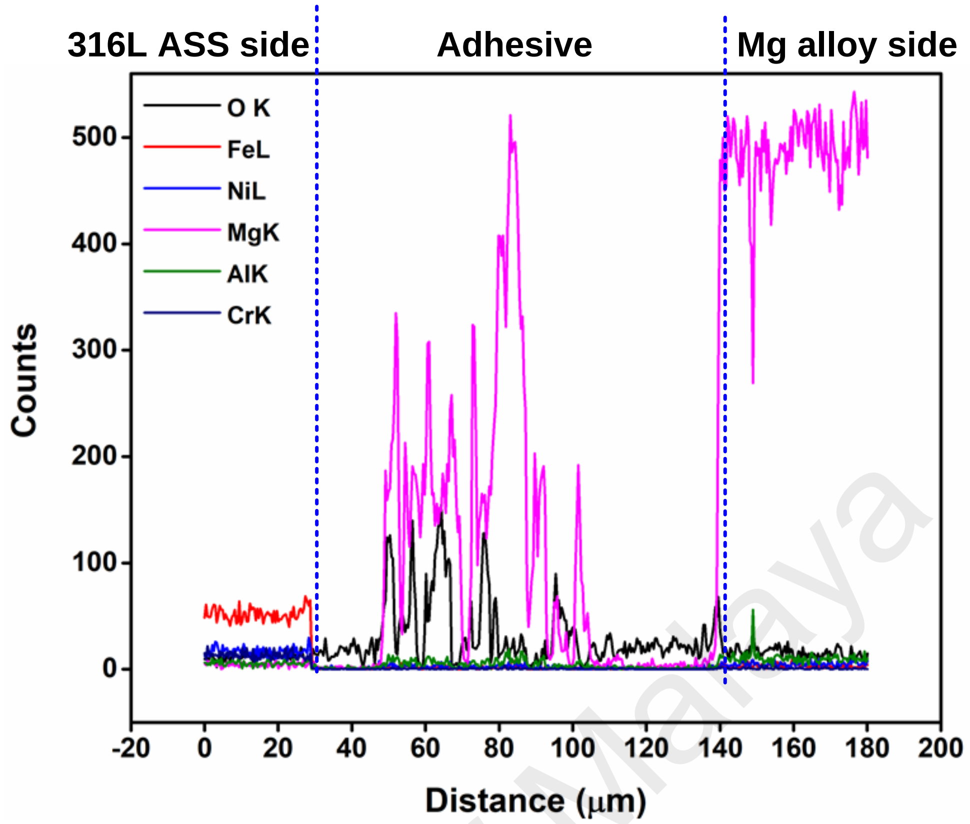

Figure 4.15: Results of EDS line scan across the Mg alloy/adhesive/316L ASS interface of the adhesive zone of the RSWB joint

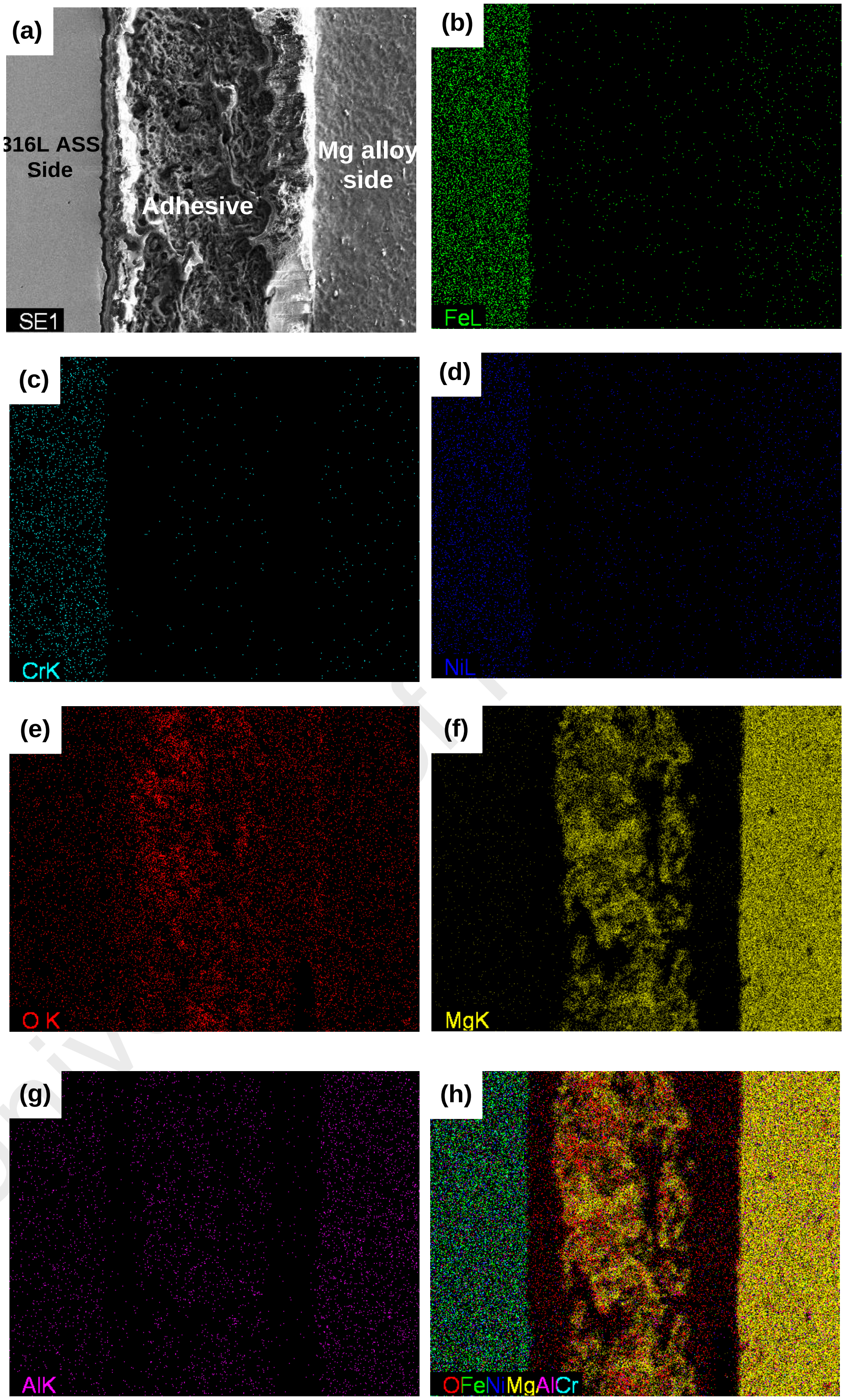

Figure 4.16: EDS elemental mapping across the ASS/adhesive/Mg alloy interface in the adhesive zone of the RSWB joint (a) secondary image; and (b) Fe; (c) Cr; (d) Ni; (e) O; (f) Mg; (g) Al elements and (h) overlay

4.2.3 Hardness characteristics

The harness typical hardness profiles of the RSW and RSWB joints are compared in Figure 4.17. It can be seen that the hardness characteristics across the BM, HAZ, and FZ for both joints are similar. The average hardness of the nugget is 59 HV for the RSWB joints and 60 HV for the RSW joints. This is in agreement with the findings of Xu et al. (2012) while studying the hardness characteristics of weld-bonded AZ31B-H24 Mg alloy/hot-dip galvanized HSLA steel and AZ31B-H24 Mg alloy/AZ31B-H24 Mg alloy joints. The average hardness in the FZ of the weld-bonded Mg/Mg joint and that of weld-bonded Mg/steel joint was found to be approximately 60HV. Furthermore, the hardness characteristics of the Mg side of the weld-bonded Mg/steel side was found to be similar to that of weld-bonded Mg/Mg joints.

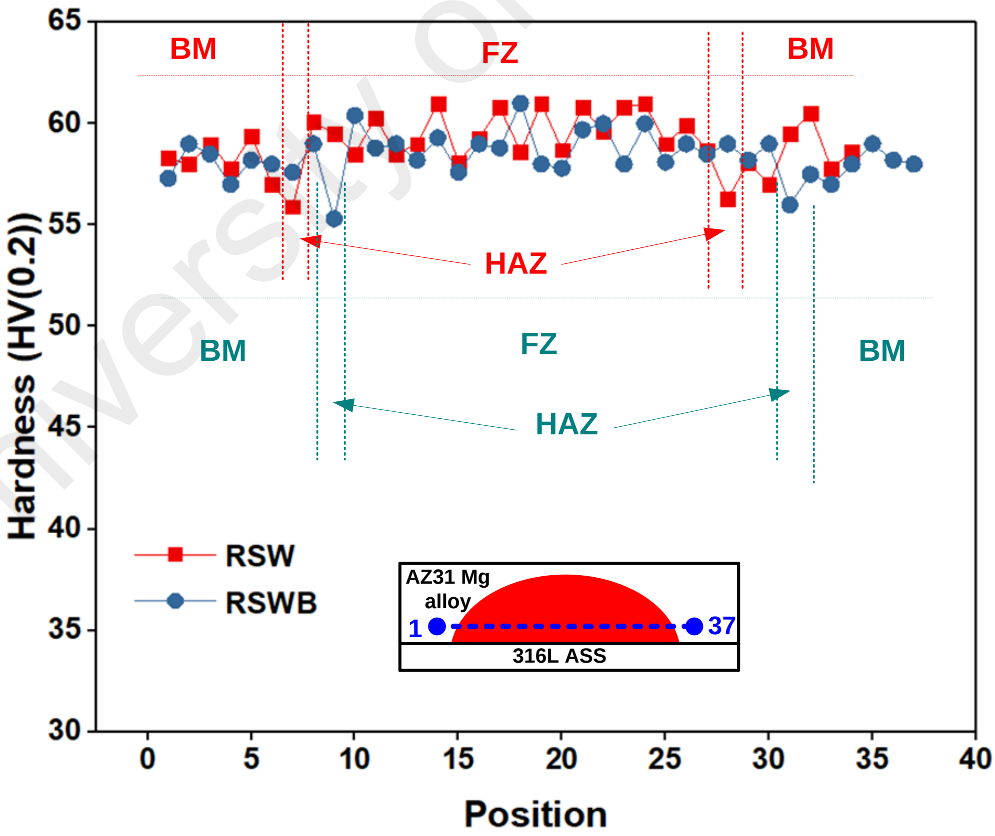

Figure 4.17: Typical hardness profile of RSW and RSWB joints

4.2.4 Tensile-shear performance

It has been shown in section 4.1.4 that the bonding diameter has a great influence on the tensile-shear properties of the RSW joints. Figure 4.18 compares the bonding diameters of the RSW and RSWB joints as a function of welding current. It is seen that for both processes, the bonding diameter increased with increase in welding current, which is due to the increase in heat input and consequently volume of melted metal. However, it is seen that for the same value of welding current, the bonding diameter of the RSWB joints is higher than that of the RSW joints, despite the fact that the RSWB joints are produced using shorter welding times. This is because the adhesive layer would increase the initial contact state and contact resistance between the sheets because of its viscosity and heat insulation, and consequently produce more heat at the interface, leading to larger bonding diameter. A similar phenomenon was observed by Shen et al. (2012), while investigating the effect of adhesive layer addition during RSW of multiple stacks of steel sheets, involving SAE1004, DP600, and DP780 steels. The nugget size of the weld-bonded joints was found to be larger than that of the RSW joints under the same welding conditions.

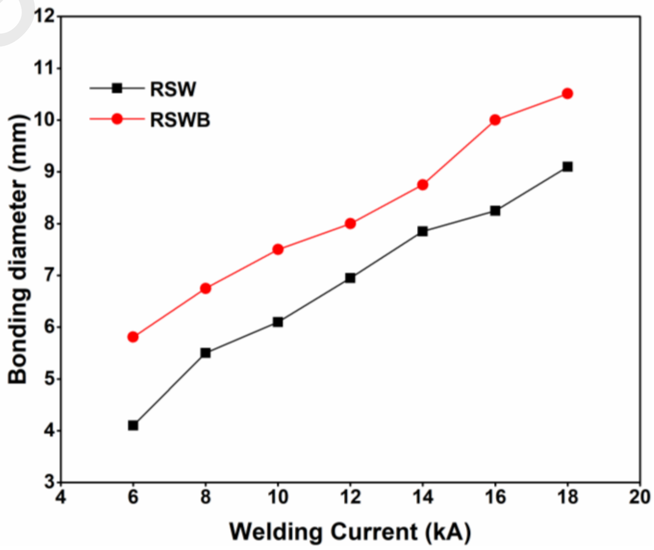

Figure 4.18 : Bonding diameter of RSW and RSWB joints as a function of welding current

The load bearing capacity of weld-bonded joints is influenced by many factors, such as the nugget size and shape, the mechanical properties of the adhesive and that of the BM (Chang et al., 1999). Figures 4.19 and 4.20 compare the peak load and energy absorption of the RSW and RSWB joints, respectively, as a function of welding current. It is seen that at a given welding current, the peak load and energy absorption of the RSWB joints are significantly higher than that of the RSW joints. This is due to the combined effect of larger bonding diameter in the weld zone and the presence of adhesive zone. Although the bonding diameter increased continuously with increased welding current, the peak load and energy absorption of the joints increased to a maximum value and then decreased with further increase in welding current. This has been attributed to expulsion. As shown in Figures 4.19 and 4.20, the maximum peak load and energy absorption were obtained at a welding current of 14 kA for RSW joints and 12 kA for RSWB joints. This indicates that the current required to produce expulsion in the RSWB joints (14 kA) is lower than that in RSW (16 kA). Khan et al. (2015) also observed, while studying the RSWB of 6061-T6 Al alloys, that expulsion occurred at lower welding current than in RSW due to the increased contact resistance caused by the presence of adhesive. The expulsion destroyed the adhesive layer and affected the integrity of the nugget, thus reducing the tensile-shear performance (Khan et al., 2015). Thus, it is unnecessary to employ high welding current during RSWB.

It is interesting to note that, as indicated in Figure 4.20, all the RSWB joints, including those with expulsion, have satisfied the minimum peak load requirement of AWS D17.2 standards (Specification of Resistance Welding for Aerospace Applications) (AWS, 2007). However, none of the RSW joints met this requirement.

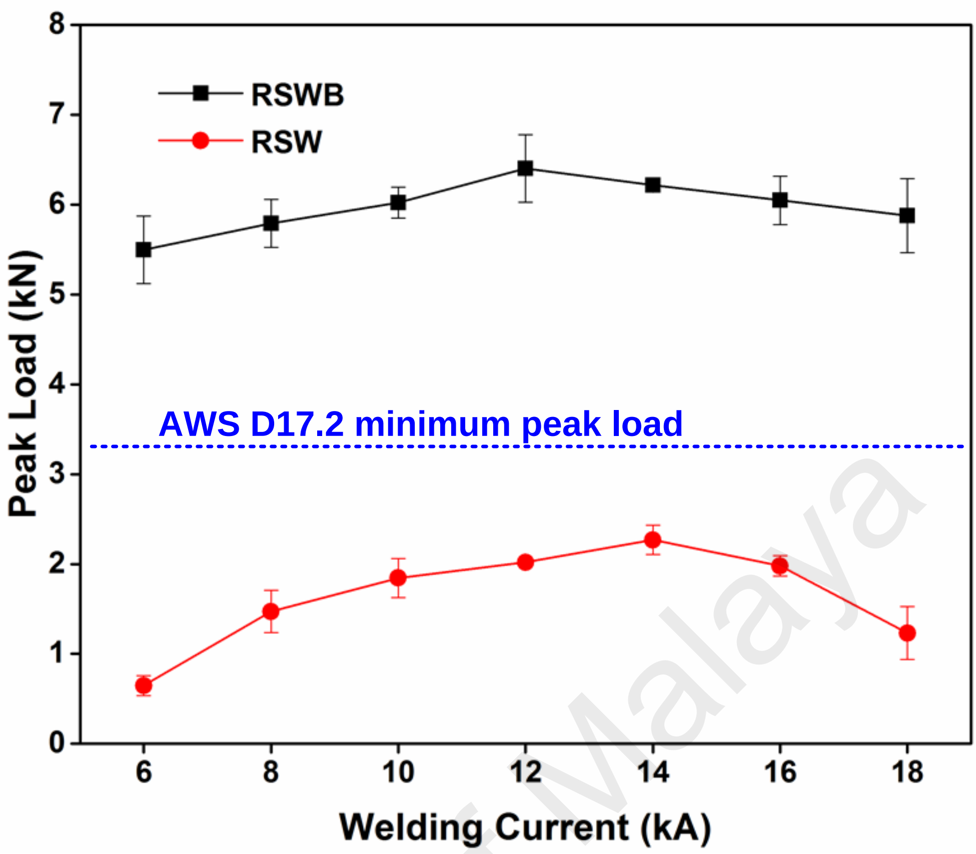

Figure 4.19: Comparison of peak load of RSW and RSWB joints as a function of welding current

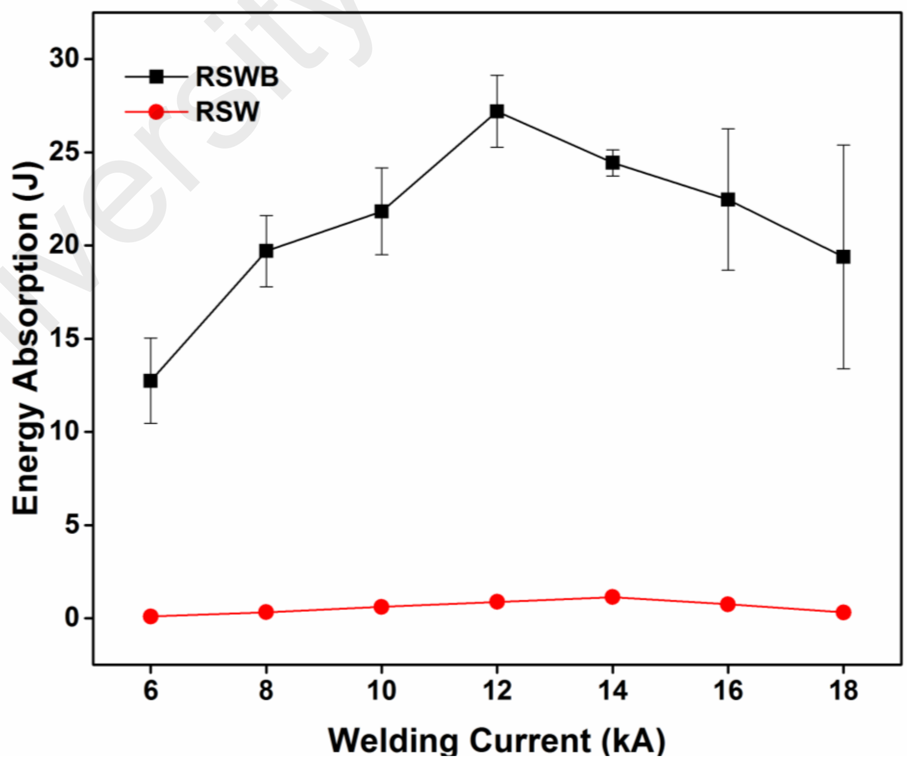

Figure 4.20: Comparison of energy absorption of RSW and RSWB joints as a function of welding current

Since RSWB combines both RSW and AB processes, the tensile-shear performance of the AB joints was also evaluated for the purpose of comparison. Figure 4.21 compares the maximum peak load and energy absorption of the joints produced by RSW, AB, and RSWB. It is seen that the RSWB joints have the best tensile-shear performance. Furthermore, the performance of the AB joints is better than that of the RSW, which can be attributed to larger bonding area. The peak load of AB joints is 4.7 kN, which is about 107% higher than that of RSW joints. The maximum energy absorption of the AB joints is 8.41J, which is about 7.5 times higher than that of RSW joints. The peak load of the RSWB joint is 6.4 kN, which is about 182% higher than the RSW joints and about 36.7% higher than that of the AB joints. The maximum energy absorption of the RSWB joints is 27.2J, which is about 24 times higher than that of RSW joints and about 3.23 times that of the AB joints. To better understand the differences in tensile-shear performances of the joints, the failure characteristics of the joints are analyzed and presented in the next section.

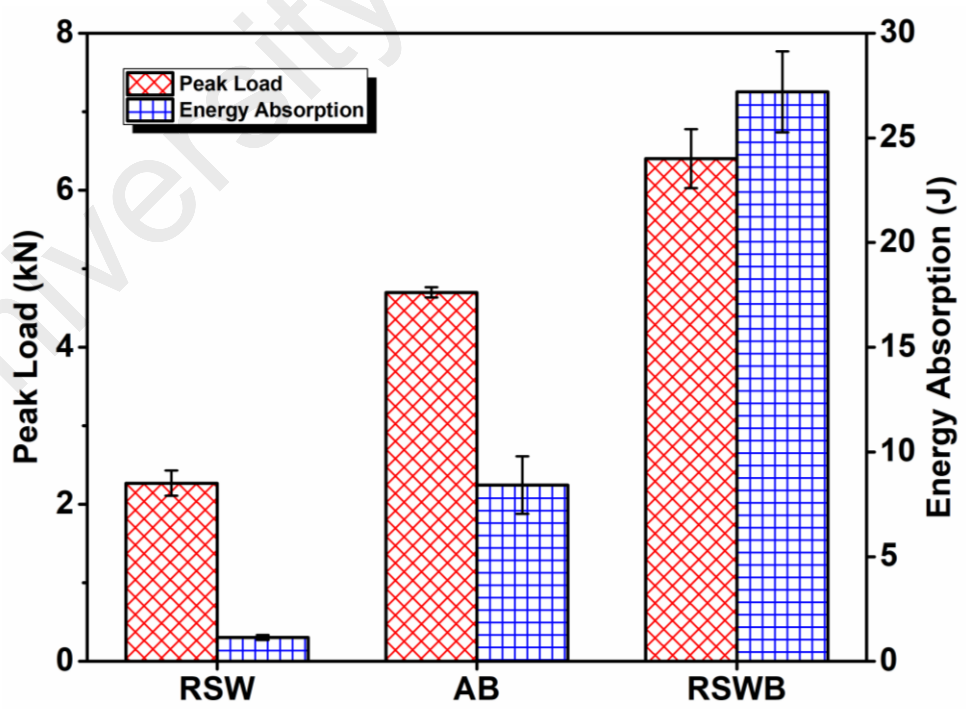

Figure 4.21: Comparison of maximum peak load and energy absorption of RSW, AB , and RSWB joints

4.2.5 Failure mode

Failure mechanism plays a vital role in the design of adhesive structures. To guarantee the safety of adhesive structures, and to promote their industrial applications, it is of paramount importance to understand their failure mechanism under external loading conditions. The mechanical properties of the adhesive and the stress states of the adhesive layer, which is influenced by the geometrical configurations and constraint effects, affect the failure characteristics of adhesive structures (Liao & Huang, 2016).

Adhesive bonded structures commonly fail in three basic modes:

1. Adhesion failure (delamination or decohesion): This type of failure mode occurs at the interface between the adhesive and one of the adherends (path A in Figure 4.22). It generally occurs at a load that is far below the design strength of the bond. It may be caused by lack of a chemically active surface, ineffective surface preparation, or improper curing (Davis, 2007).
2. Cohesive failure: In this failure mode, the crack propagates through the adhesive layer (path B in Figure 4.22), as the adhesive bond strength is exceeded. When this failure mode occurs, adhesive is observed on the matching surfaces of both adherends (Davis, 2007).
3. Adherend (base metal) failure: This type of failure mode involves crack propagation through one of the adherends (path C in Figure 4.22). This is a desirable failure mode as it implies that the joint is stronger than the adherend in which the failure occurs.
4. Hybrid failure mode: This involves a combination of one or more of the above failure modes. For example, path D in Figure 4.22.

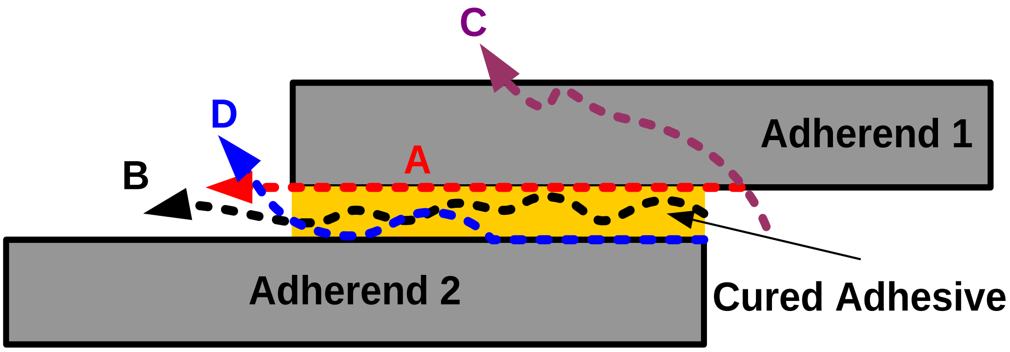

Figure 4.22: Schematic illustration of the basic failure modes in adhesive bonded structures

Figure 4.23 compares the typical load–displacement curves for RSW, AB, and RSWB joints. Clearly, compared with the RSW and AB joints, the RSWB joints showed superior performance, in terms of failure load and extension at failure. The curve for AB and RSW joints exhibit similar behavior, and can be divided into stages, 1 and 2. In stage 1, the load increased rapidly as the adhesive (in the case of AB joints) or the nugget (in the case of RSW joints) is deformed. The load reached its peak value, which corresponds to the point of crack propagation, and then failed abruptly (stage 2), indicating little or no plastic deformation. On the other hand, the curve for the RSWB joints displayed mixed fracture characteristics, and can be divided into three stages, 1, 1', and 2. Similar regions were identified during RSWB of dual phase steels (Sam & Shome, 2010) and USWB of Al/Mg alloys (Feng et al., 2016a). It is interesting to note that stage 1 on both the AB and RSWB curves exhibit similar characteristics, the load increased rapidly and reached approximately the same value, as indicated by blue dotted circle in Figure 4.23. This suggests that the load was sustained primarily by the adhesive in stage 1 of the RSWB joints. In stage 1', which is only observed in the case of RSWB joints, the load increased non-linearly, at a relatively lower rate, leading to a long and progressive tail before reaching the peak point. This behavior has been attributed to the progressive reduction of the strength of the adhesive bond and the increased deformation of the nugget (Sam &

Shome, 2010). This slow and progressive deformation accounts for the tremendous increase in energy absorption of RSWB joints compared to the AB and RSW joints. With further displacement beyond the peak point, the load dropped suddenly due to the complete failure of both the adhesive and spot weld (stage 2). Once failure is initiated, it proceeds rapidly because of the rigidity of the cured adhesive. It is important to note that stage 2 in the RSWB joints exhibit similar behavior to that of the AB and RSW joints: final failure occurred abruptly, with little or no plastic deformation.

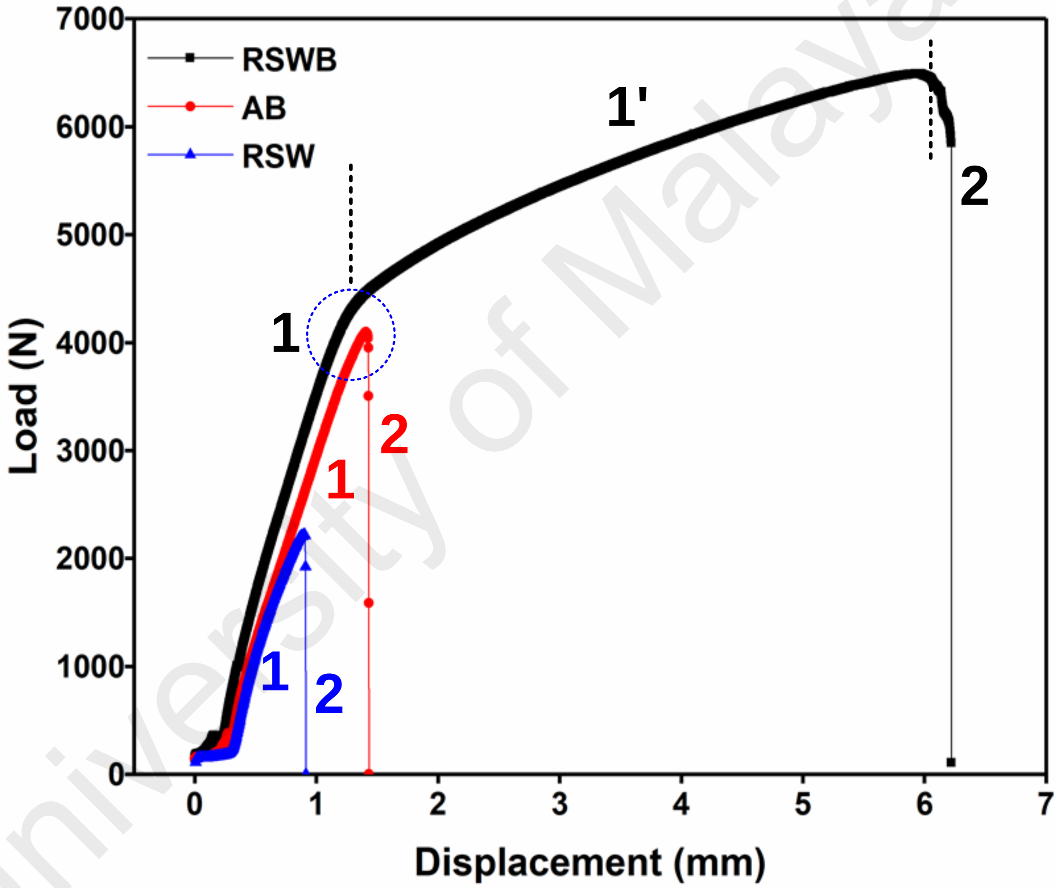

Figure 4.23: Comparison of load-displacement curves for RSW, AB, and RSWB joints

During the tensile shear test, some degree of plastic deformation occurred in the ASS sheet. Thus, after final separation, the ASS steel was found to be longer than the AZ31 Mg alloy. This is due to the low yield strength of the steel and its relatively small thickness. This extension could not have occurred in stage 2, because the final failure occurred abruptly; it likely occurred in stage 1’. Thus, the tremendous increase in tensile-shear performance is mainly because of the processes that occurred in stage 1’.

The fracture surface characteristics of the AB joints are shown in Figure 4.24. To fully analyze the surface characteristics, FESEM images were taken and EDS analysis was conducted at various locations.

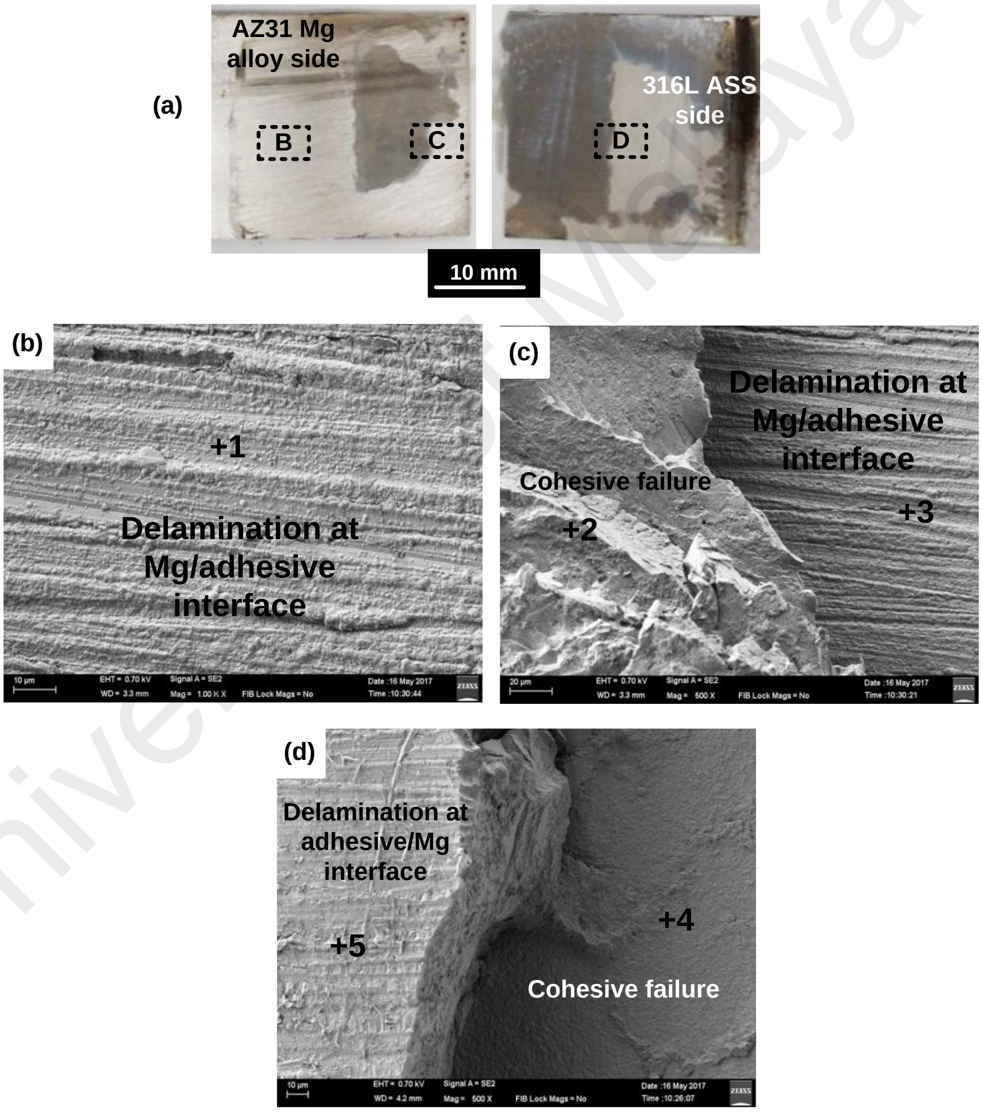

Figure 4.24: Fracture surface of AB joints: (a) Mg and ASS sides; FESEM image of (b) region B in (a); (c) region C in a; (d) region D in a

It can be inferred from the results of EDS analysis (Figure 4.25), that points 1 and 3 are basically Mg alloy, suggesting that delamination or decohesion has occurred between at the Mg alloy/adhesive interface. It can also be inferred that points 2 and 4 are within the adhesive, indicating cohesive failure. The results also indicate that point 5 is adhesive, and from the surface morphology, it can be inferred that delamination has occurred between at the adhesive/Mg interface.

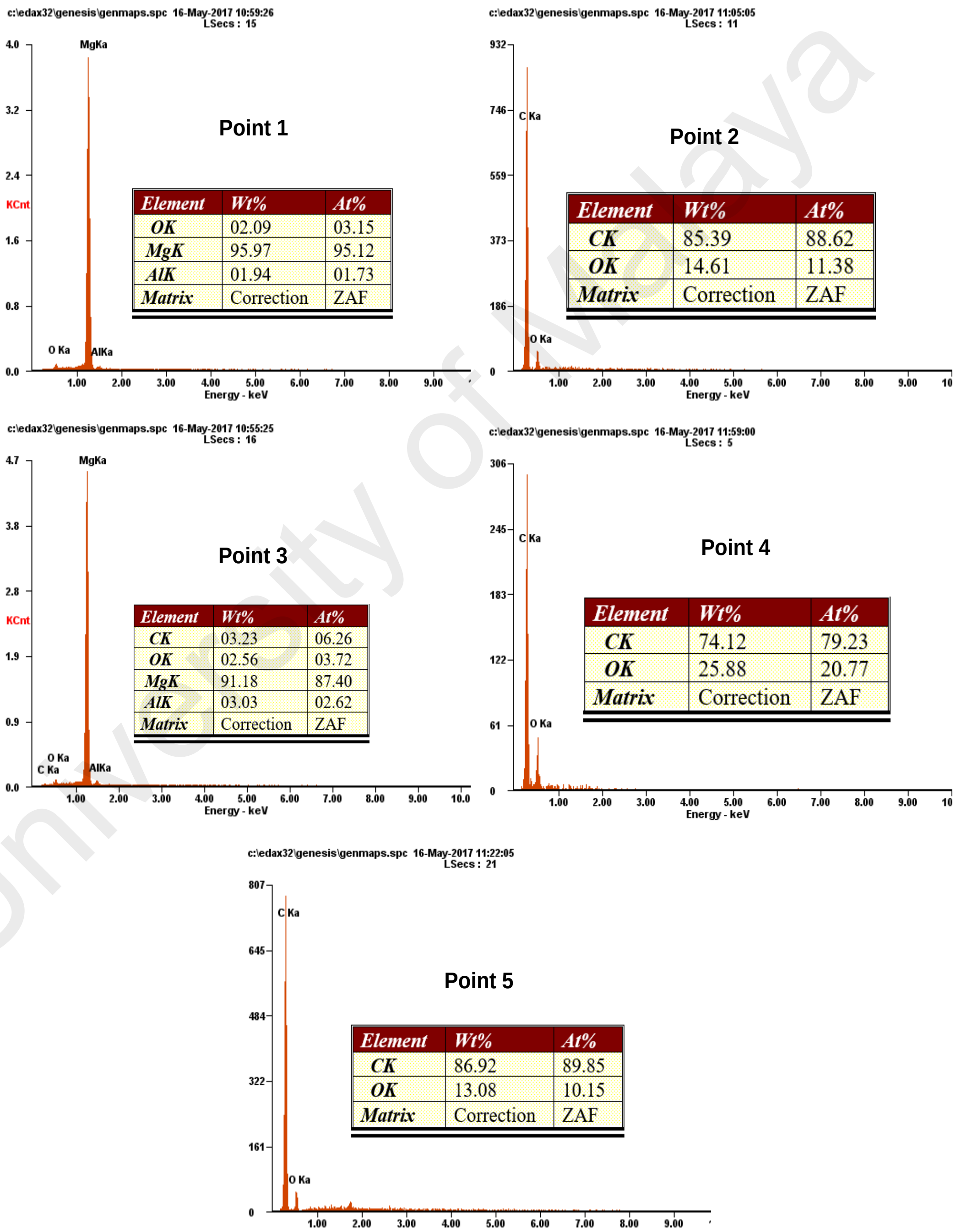

Figure 4.25: EDS spectrum of points 1, 2, 3,4 and 5 in Figure 4.24

Overall, the failure mode of the AB joint consisted mainly of delamination at Mg/adhesive interface and a smaller region of cohesive failure within the adhesive. A similar observation was reported by Feng et al. (2016a) in the case of Al/Mg alloy AB joints, in which the failure occurred through delamination at the Mg/adhesive interface. This was attributed to the brittle nature of the adhesive after curing and the poor adhesion at the of Mg/adhesive interface, leading to rapid crack propagation at this interface.

Figure 4.26 shows the fracture surface morphology of the Mg alloy and ASS sides of the RSWB joints. Figure 4.26 b-d show FESEM images taken at various locations of the adhesive zone of the joints. From the surface characteristics of these images and the results of EDS analysis shown in Figure 4.27, it is seen that the failure mode in the adhesive zone is predominantly cohesive failure and a few regions of delamination at the Mg/adhesive interface. This is different from the case of the AB joints, in which the failure occurred mainly at the Mg/adhesive interface as a result of delamination of the adhesive from the Mg alloy (Figures 4.23 and 4.24). This is probably because the electrode pressure and welding heat increased the ductility of the adhesive and the adhesion between the adhesive and the Mg alloy.

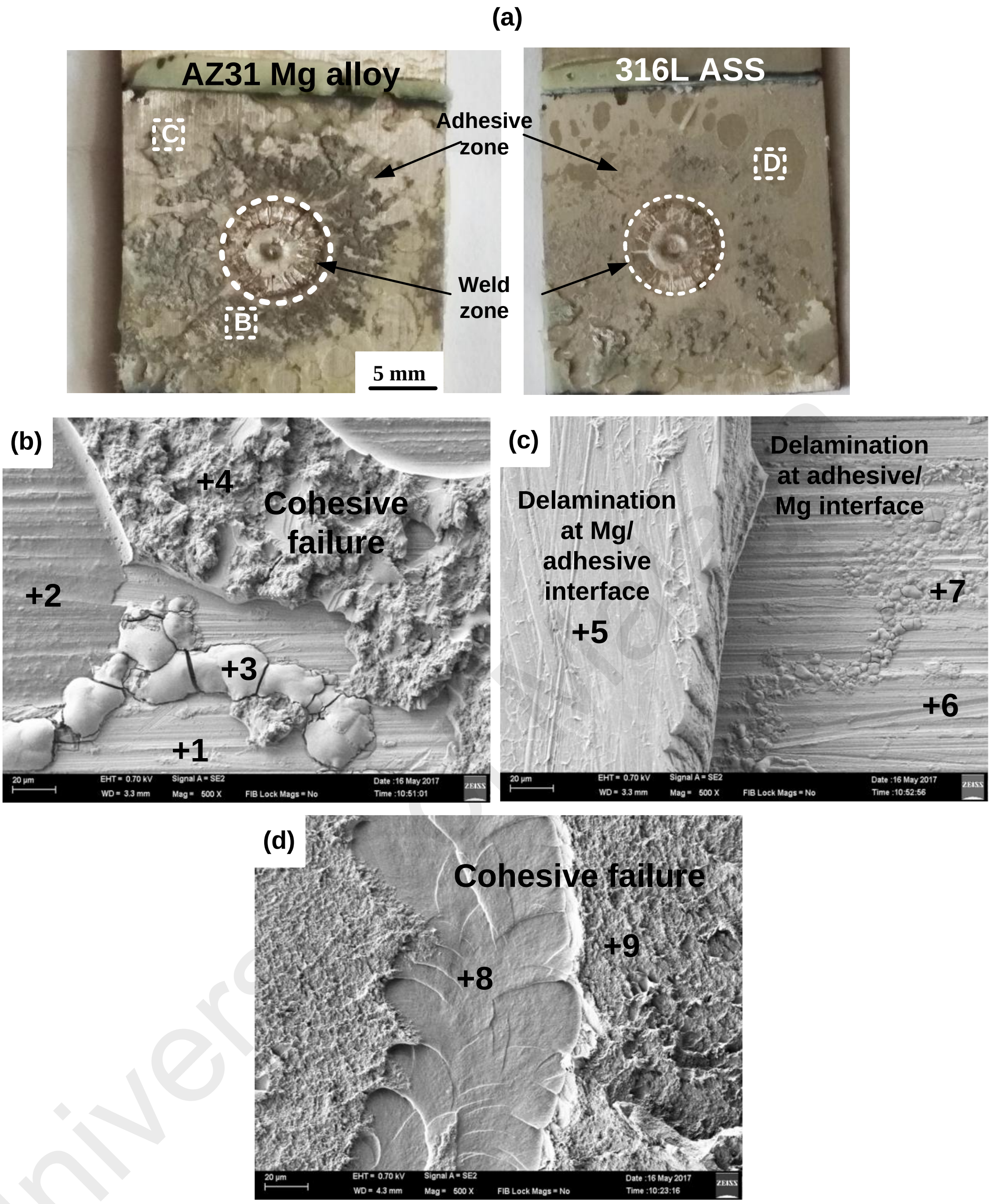

Figure 4.26: Fracture surface of RSWB joints: (a) Mg alloy and ASS sides; FESEM image of (b) region B in a ; (c) region C in a; (D) region D in a

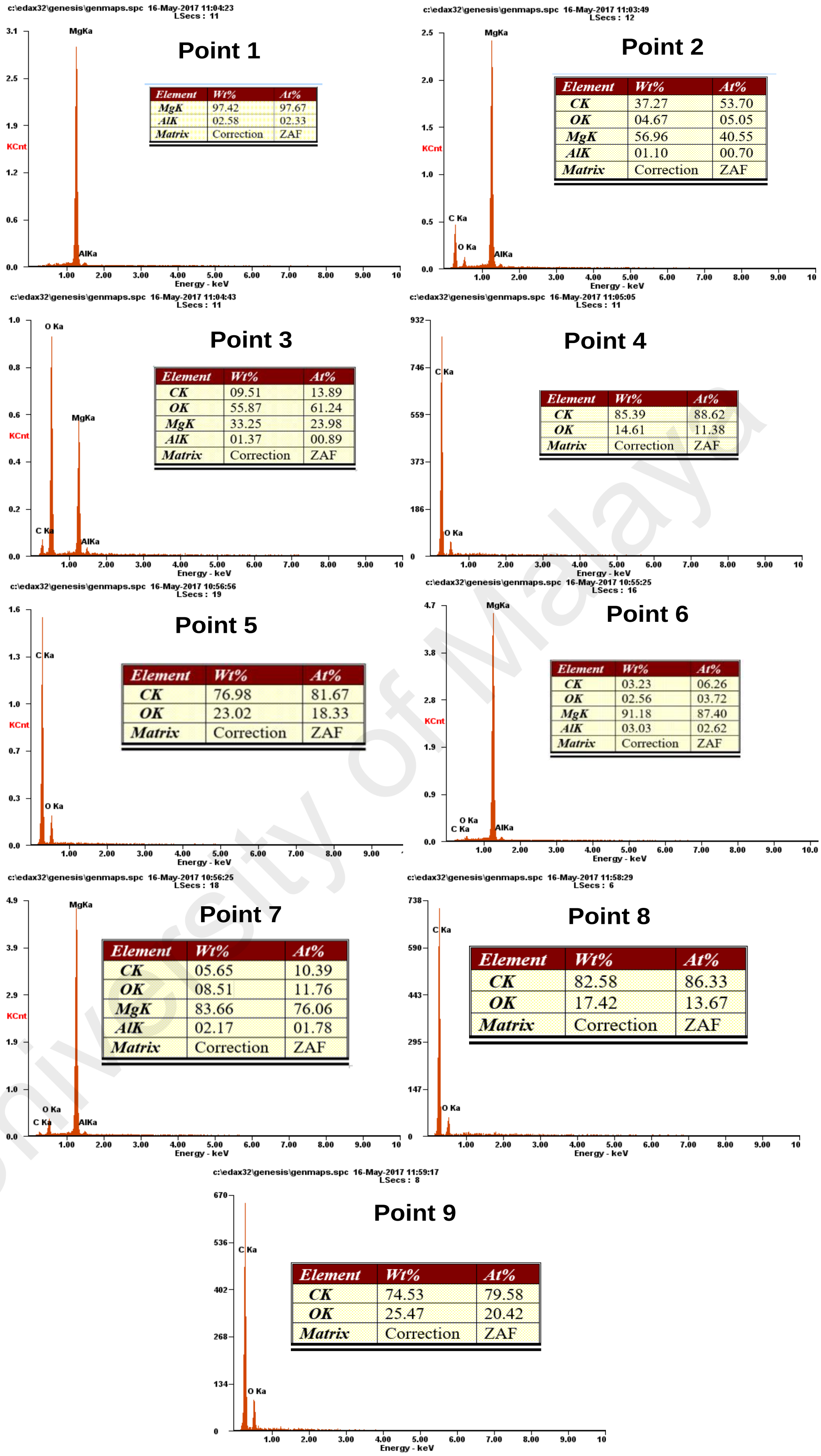

Figure 4.27: EDS spectrum of points 1-9 in Figure 4.26

Figure 4.28 shows the fracture surface characteristics of the weld zone of the Mg side of the RSWB joint. Similar to that of RSW joint (Figure 4.10), shrinkage cavities and numerous small voids are seen on the surface of the weld zone. However, there are more voids in the case of the RSWB joints, which is possibly because of the generation of gases from the decomposition of the adhesives. It is interesting to note that no adhesive is visible on the macroscopic morphology of the weld zone (Figure 4.28 a), further suggesting that the adhesive has been pushed out of the weld zone. To confirm whether or not there is residual adhesive on the surface, higher magnification FESEM image was taken (Figure 4.28b) and EDS analysis was conducted. The results of the EDS analysis, shown in Figure 4.29, indicate that point 1 is Mg alloy and point 2 is Mg alloy with some adhesive. This shows that the adhesive is not pushed completely from the weld zone; a miniscule amount remained.

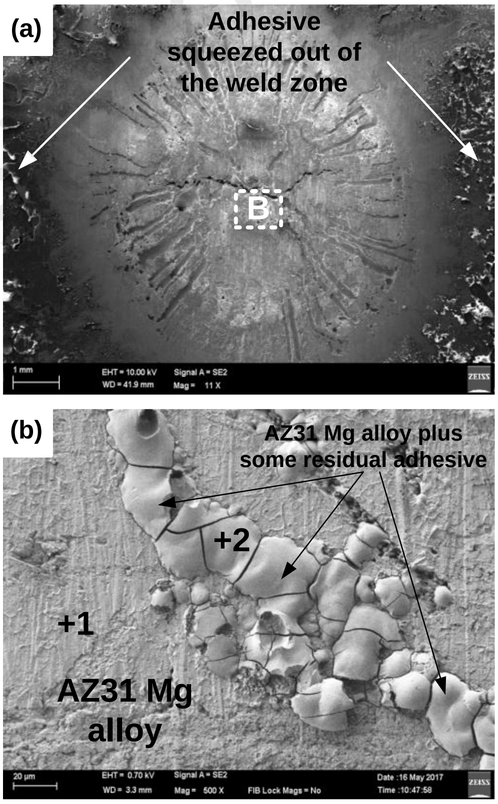

Figure 4.28: Fracture surface of the Mg alloy side of the weld zone of RSWB joints: (a) macroscopic morphology; (b) higher magnification of region B in a

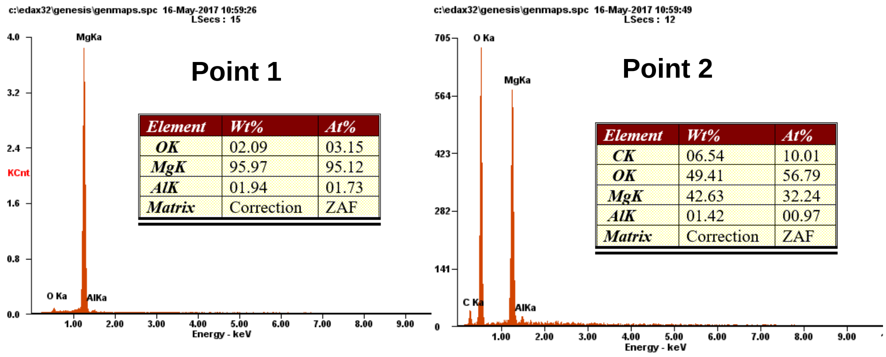

Figure 4.29: EDS spectrum of points 1 and 2 in Figure 4.27

The fracture surface of the ASS side of the weld zone has also been characterized. Figure 4.30 shows the morphology of the surface. Higher magnification FESEM image (Figure 4.30 b) shows that the surface has the morphology of as-received ASS (Figure 4.11 b), with some residual AZ31 Mg alloy and traces of adhesive, as confirmed by EDS mapping (Figure 4.31).

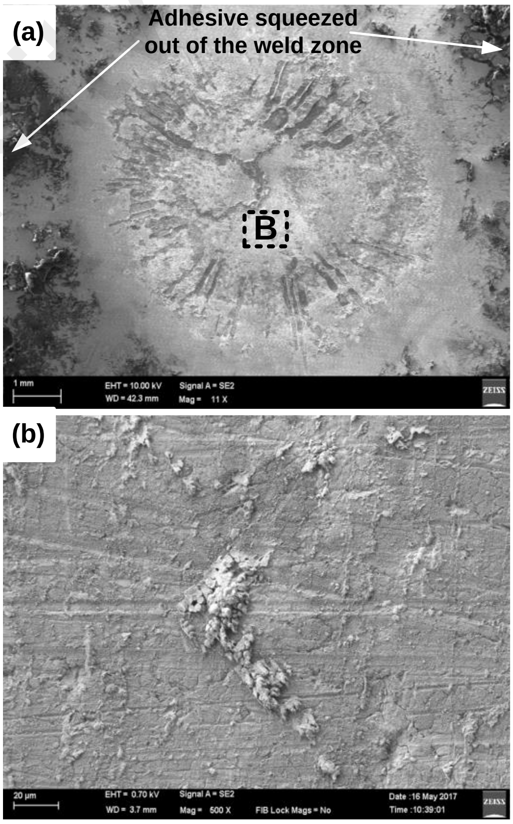

Figure 4.30: Fracture surface of the ASS side of the weld zone of the RSWB joint : (a) macroscopic morphology; (b) higher magnification of region B in a

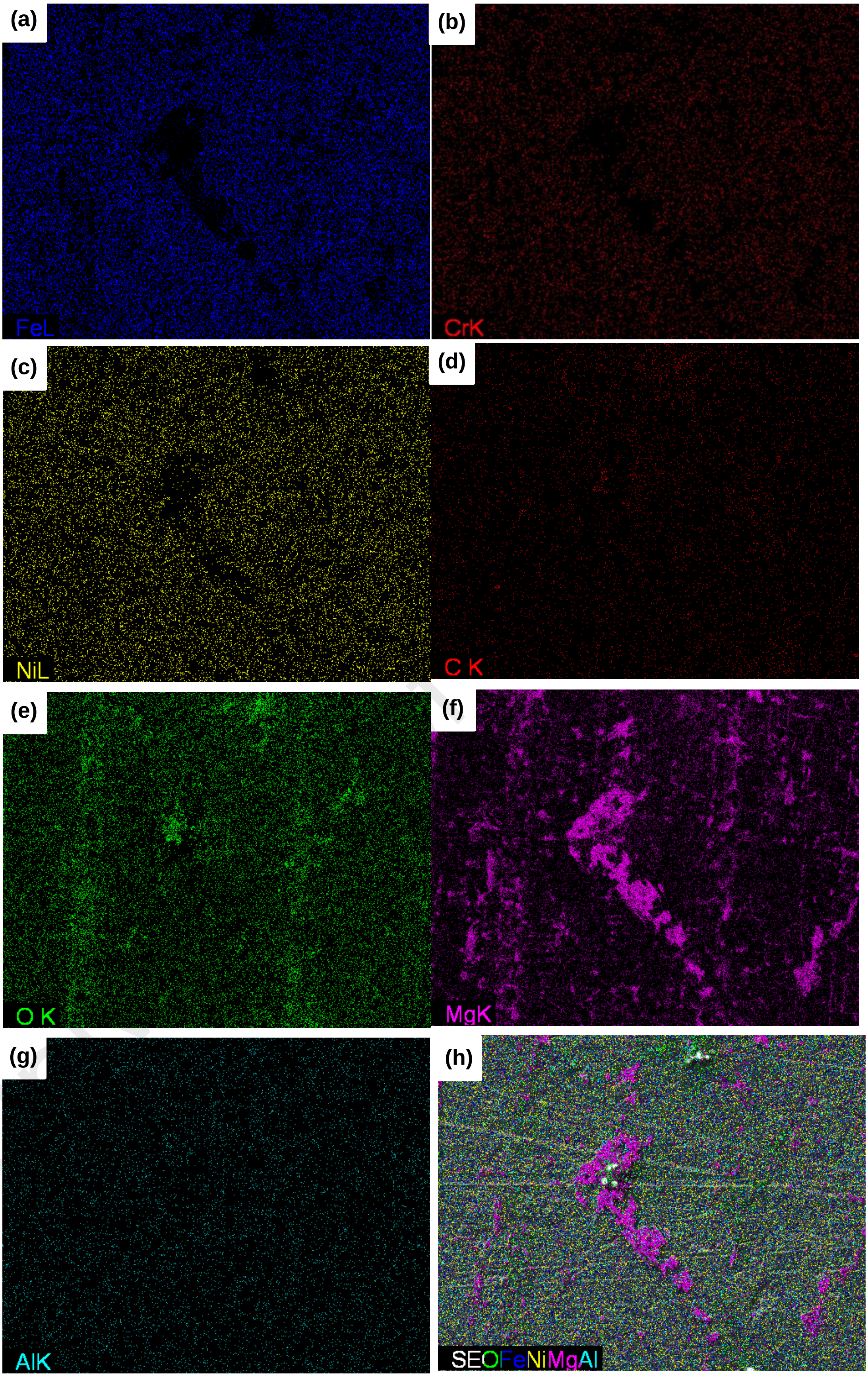

Figure 4.31: EDS mapping of region B in Figure 4.29

These confirmed that the ASS did not melt during the RSWB process and that the failure in the weld zone largely occurred at the Mg/ASS interface. It also confirms that some residual miniscule adhesive remained on the surface. Overall, the RSWB joint exhibited a hybrid failure mode, involving mainly cohesive failure in the adhesive zone and IF failure through the Mg alloy/ASS interface in the weld zone.

4.3 REW joints

4.3.1 Macrostructure and microstructural evolution

Figure 4.32a shows the typical macroscopic morphology of the joint produced by REW. It is seen that the nugget is asymmetrical, with the Q235 rivet side having the larger part. Also, the final solidification line is shifted toward the Q235 steel side. The formation of an asymmetrical nugget is a common phenomenon in RSW of dissimilar steels, and is a result of differences in thermal conductivity and electrical resistivity (Marashi et al., 2008a). For example, it was observed during dissimilar RSW of low carbon steel/martensitic stainless steel (Safanama et al., 2012), galvanized low carbon steel/ASS (Marashi et al., 2008a), and DP600 steel /ASS (Poggio et al., 2005). In all the aforementioned studies, the larger part of the nugget was in the stainless steel due to its lower thermal conductivity and higher electrical resistivity. In the present study, however, the nugget size and penetration are larger on the carbon steel (Q235) side. It has been established that nugget formation is controlled by the rate of heat generation and dissipation. While the heat generation is influenced by the welding parameters and electrical resistivity of the materials being welded, the heat dissipation depends on the stack configuration, sheet thickness and thermal conductivity, and cooling rate (Eizadi & Marashi, 2016). In contrast to the above mentioned studies, where the sheets are more or less of the same thickness, in the present work, the thickness of the Q235 steel rivet (4.5mm) is significantly higher than that of ASS (0.7mm). Thus, the bulk resistance, and consequently, the heat generation in the Q235 steel side is higher. Furthermore, the heat dissipation from the ASS stainless steel is higher because of its proximity to the water-cooled electrodes. These combined effects shifted the nugget as well as the final solidification line toward the Q235 side.

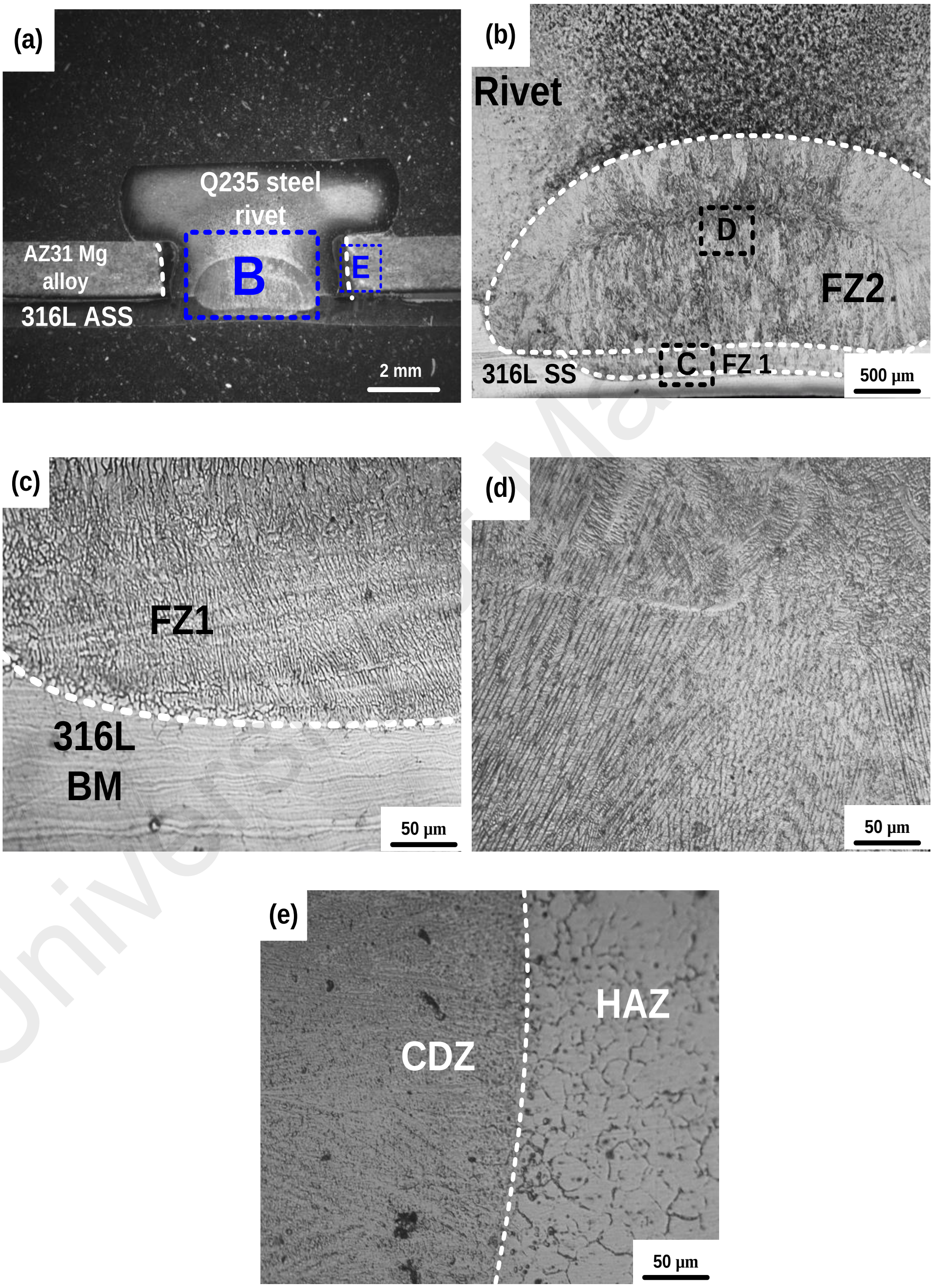

Figure 4.32 : Macrostructure and microstructure of REW joint (a) macrostructure; (b) higher magnification of region B in (a); (C) microstructure of region C in (b); (d) microstructure of region D in (b); (e) microstructure of region E in (a)

As shown in Figure 4.32 b, the FZ can be divided into two zones, i.e., peripheral FZ (FZ1) and the main FZ (FZ2). It is interesting to note that the peripheral FZ formed only on the ASS side. This kind of peripheral FZ was observed in both the upper and lower sheets during RSW of similar two-sheet ASSs (Pouranvari et al., 2015a) and three- sheet ASSs (Zhang et al., 2016). The formation of two-zone nugget in ASS RSW has been attributed to the differences in volume fraction of delta ferrite between the periphery and the main nugget (Pouranvari et al., 2015a). The evolution of microstructure in the nugget is controlled by the chemical composition and cooling rate. According to Figure 4.33, during welding of ASSs, the solidification occurs in ferrite-austenite (FA) mode, according to the transformation path shown equation 4.2 (Lippold & Kotecki, 2005; Pouranvari et al., 2015a; Zhang et al., 2016).

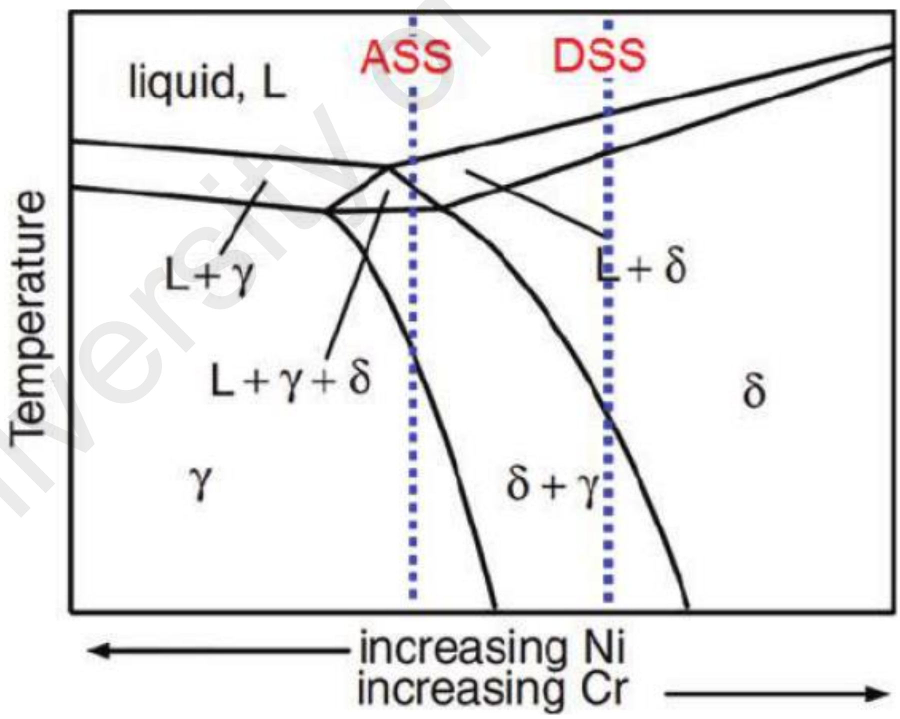

Figure 4.33: Schematic showing solidification and post-solidification transformation path in ASSs and DSSs welds (Pouranvari et al., 2015a)

$$L \xrightarrow{I} L + \delta \xrightarrow{II} L + \delta + \gamma \xrightarrow{III} \delta + \gamma \qquad (4.2)$$

Thus, the austenitic microstructure of the BM transforms into a mixture of austenite and intercrystalline delta ferrite (Zhang et al., 2016). During this transformation, the ferrite is consumed by austenite through a diffusion controlled reaction. The cooling rate is higher at the periphery than at the center of the nugget because of its proximity to the water-cooled electrodes. Therefore, there is limited time for the diffusion controlled reaction (stage III) to occur in the periphery, leading to a higher volume fraction of delta in this region (Zhang et al., 2016).

As indicated by white dotted lines in Figure 4.32 a, the Mg alloy melted and braze-welded to the Q235 steel sides, forming a nugget at the Mg side. The microsctructe of this nugget consisted of CDZ, as shown in Figure 4.32 e. This joining was found to be beneficial as the rivet remained attached to the Mg alloy after tensile test.

Figure 4.34 shows the microstructural evolution in the HAZ of Q235 steel rivet. The observed heterogeneous microstructure is as a result of temperature gradient. The peak temperature and cooling rate experienced at any point in the HAZ are inversely proportional to its separation from the fusion line (Marashi et al., 2008a). As shown in Figure 4.33 a, the HAZ can be divided in two distinct zones, namely, the upper-critical HAZ (UCHAZ) and inter-critical HAZ (ICHAZ). Figure 4.34 b shows a portion of Fe–C phase diagram, which can serve as a basis to explain the phase transformations in the HAZ as follows:

i. UCHAZ- As depicted in Figure 4.34 b, the peak temperature attained in this zone during welding is above A_{C3}, and the BM microstructure underwent complete austenitization. Upon cooling, the austenite transformed into martensite. This martensitic transformation is as a result of the high cooling rate inherent in RSW (Eizadi & Marashi, 2016). It is reported that the cooling rate in RSW is approximately in the range of 3000 ^{o}C/s for 2 mm thick sheets to over 10^5 °C/s for sheets with thickness less than 0.5 mm (Pouranvari & Marashi, 2010). The UCHAZ can further be classified into coarse-grained zone (Figure 4.34 c) and fine-grained zone (Figure 4.34 d). The coarse-grained zone is adjacent to the FZ boundary and experienced a peak temperature that is well above A_{C3}, leading to the formation of large grain sized carbon-rich austenite, which transformed to hard and coarse martensite upon cooling (Figure 4.34 c). The fine-grained zone experienced a relatively lower peak temperature. The primary austenite grain size, and therefore, the martensite plates are relatively smaller (Figure 4.34 d) (Yuan et al., 2017).

ii. ICHAZ- As shown in Figure 4.34 b, this zone experiences a peak teperature that is between A_{C1} and A_{C3}, transforming the microstructure of the BM into ferrite and austenite (Safanama et al., 2012). Depending on hardenability of the steel and cooling rate, the austenite transforms into martensite, bainite, or ferrite/pearlite upon cooling (Pouranvari et al., 2015b). In the present study, the microstructure of the ICHAZ consisted of pearlite and ferrite, as shown in Figure 4.34 e. The volume fraction of pearlite in the ICHAZ (Figure 4.34 e) is higher than in the BM (Figure 4.34 f). This is as a result of the re-austenization that occurred in the ICHAZ (Pouranvari et al., 2015b).

The microstructure of the BM of the Q235 steel rivet consisted essentially of ferrite and some pearlite, both at the rivet cap (BM2) and shank (BM1) as shown in Figure 4.34 f. However, as can be seen in the figure, the grains in the BM2 are deformed, probably because the rivet was produced through cold heading, leading to some amount of cold work in the rivet cap.

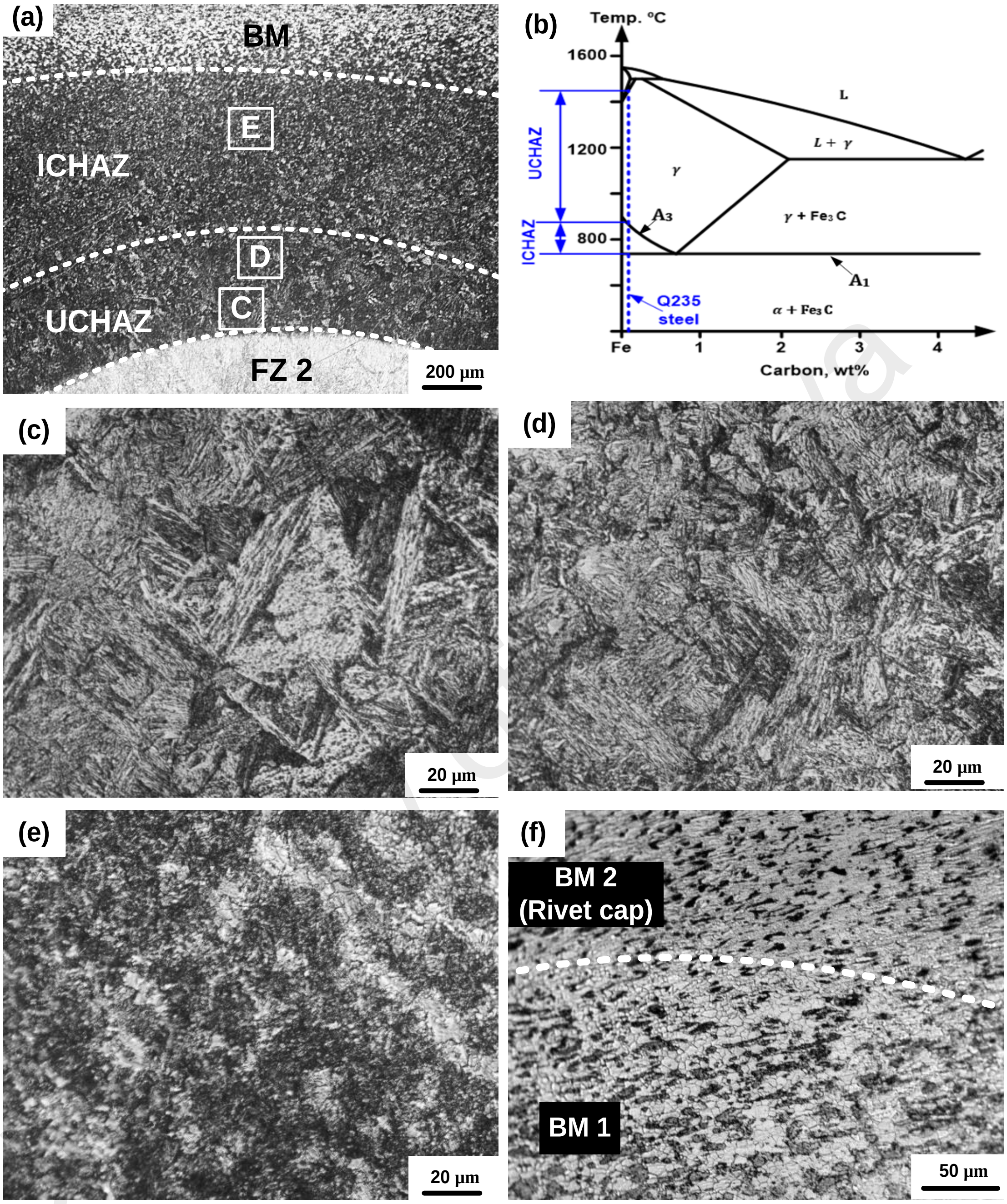

Figure 4.34 : Microstructure of the HAZ and BM of the Q235 steel rivet: (a) microstructural gradient ; (b) Fe-C phase diagram; (c) higher magnification of region C in (a); (d) higher magnification of region D in (a); (e) higher magnification of region E in (a); (f) BM microstructure

4.3.2 Elements distribution across the REW joints

It should be noted that the Q235 steel BM has higher Fe and C contents than the ASS BM, and the ASS BM has higher Ni and Cr contents than the Q235 steel BM (Table 3.1). The elemental mapping of the major alloying elements (Fe, C, Cr, and Ni) across the REW joint is shown in Figure 4.35.

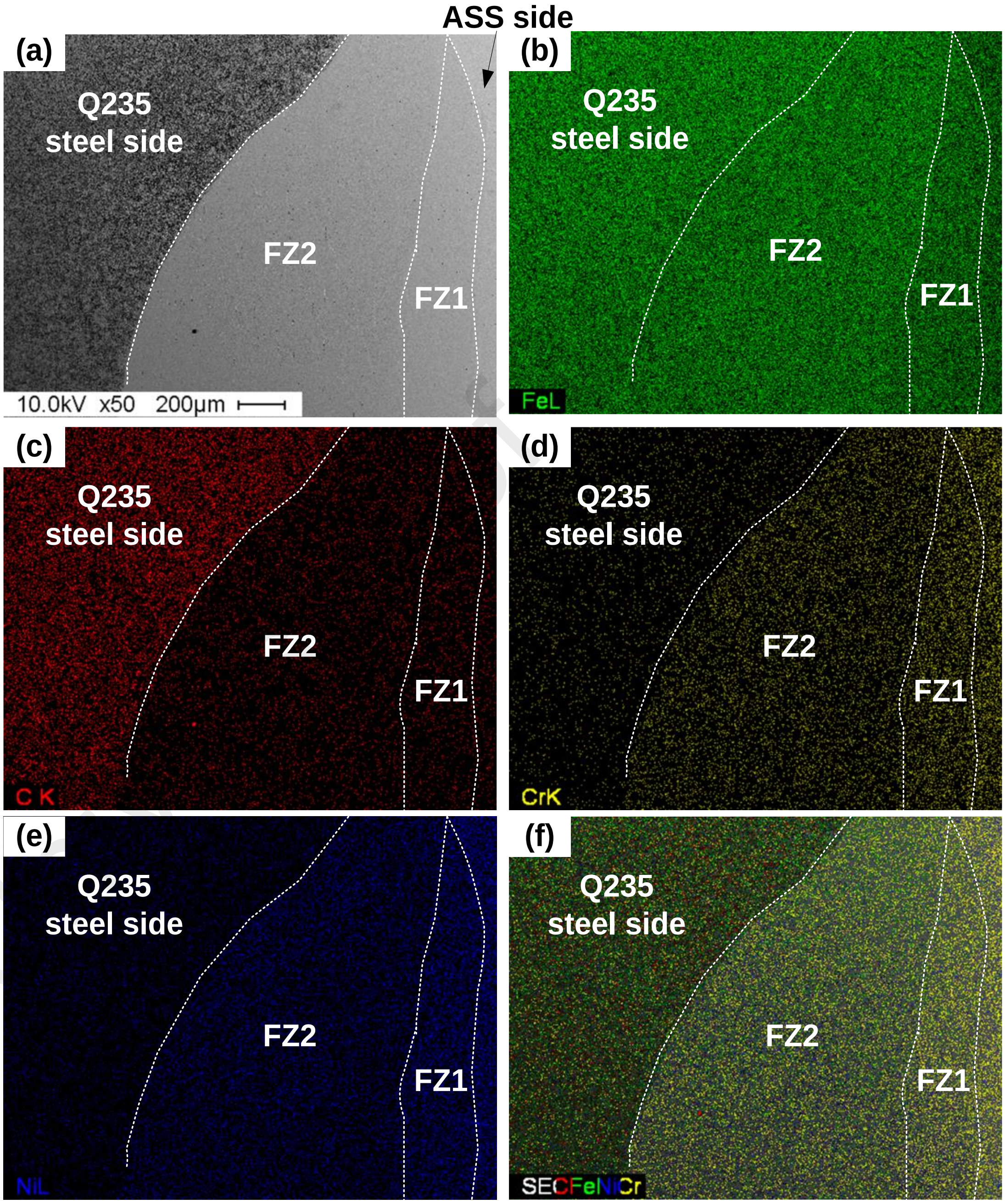

Figure 4.35: Elemental mapping of major alloying elements across the REW joint: (a) secondary image (SE); distribution of (b) Fe; (c) C; (d) Cr; (e) Ni; (f) overlay

Referring to Figure 4.35, it can be inferred that Fe and C diffused towards the ASS side from the Q235 steel side. The concentration of C is evidently higher on the Q235 steel side than in FZ1, FZ2, and the ASS side. The figure also suggests that Ni and Cr elements diffused toward the Q235 steel side from the ASS side. Generally, for each individual zone, there is uniform distribution of each of the major alloying elements. Furthermore, the concentration of each alloying element in FZ1 is similar to the ASS side and different from that of FZ2 and Q235 steel side. This explains the reason for the formation of FZ1 only on the ASS side and why the microstructure in FZ1 is similar to that obtained during RSW of similar ASSs.

4.3.3 Hardness characteristics

The mechanical performance of resistance spot welds are greatly influenced by hardness variation across the weldment (Pouranvari et al., 2015a). Figure 4.36 shows the typical vertical hardness profile of the REW joint. The observed hardness varation is consistent with the microstructural gradient in the FZ (Figure 4.32) and HAZ (Figure 4.34). The hardness value of any zone depends on (i) the hardness of the individual constituents, such as austenite, martensite and ferrite, and (ii) strengthening effect of the grain and phase boundaries (Pouranvari et al., 2016). The average hardness value of FZ2 is 401.3 HV, which is higher than that of FZ1 (331.5HV). The average hardness value of FZ2 is similar to the hardness value obtained by Alenius et al. (2006) during dissimilar RSW of galvanized carbon steel and ASS (slightly above 400 HV 0.2). The higher hardness value of FZ2 can be attributed to its triplex microstructure of austenite and delta ferrite, containing some amount of martensite with the high phase boundaries area fraction (Pouranvari et al., 2016). Furthermore, the FZ is enriched in Cr (Figure 4.35 d), which would strengthen both ferrite and martensite through a substitutional solid solution strengthening process (Pouranvari et al., 2015b).

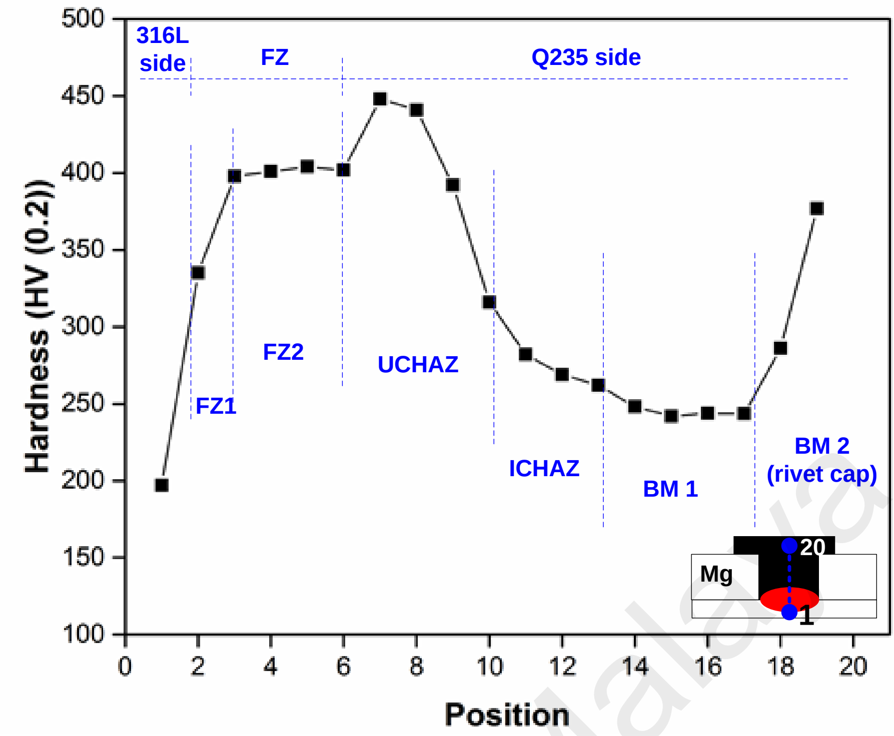

Figure 4.36: Hardness profile of REW joint

The most obvious hardness variation occurred in the Q235 HAZ. The average hardness of the UCHAZ, ICHAZ, and BM is 427 HV, 282.3 HV, and 244.3 HV, respectively. The higher hardness of the UCHAZ and ICHAZ compared to BM is due to martensitic transformation and higher volume fraction of pearlite, respectively. It can be seen that the hardness of both UCHAZ and ICHAZ decreased with increasing distance away from the FZ boundary. This can be attributed to the reduction in peak temperature with distance from the fusion line, resulting in lower volume fraction of martensite and pearlite in the UCHAZ and ICHAZ, respectively (Pouranvari et al., 2015b). The peak point in the hardness profile (448 HV) is located in the UCHAZ, adjacent to FZ2, which corresponds to the fully martensitic coarse-grained zone (Figure 4.33 c). Two different hardness values are obtained in the Q235 steel BM. The average hardness value of the BM2 (331.5 HV) is higher than that of BM 1(244.3) because of the presence of deformed grains in the former (Figure 4.34 f). The hardness value on the ASS side is 197 HV, which is lower than that of the BM (212 HV). This reduction may be attributed to the loss of any possible previous work hardening in the BM (Pouranvari & Marashi, 2012).

4.3.4 Tensile-shear performance

The nugget diameter (measured from the metallographic samples), peak load, and energy absorption of the REW joints as a function of welding current are shown in Figure 4.37. It is seen that the welding current has great influence on the nugget diameter and consequently on the peak load and energy absorption. The nugget diameter increased continuously with increased welding current. Also, by increasing the welding current from 5 to 8 kA, the peak load and energy absorption increased from 1.85 kN and 2.85 J to 3.71 kN and 10.19 J, respectively, due to enlarged nugget diameter. However, further increase in welding current resulted in a significant drop in peak load and energy absorption, as a result of excessive melting of the Mg alloy around the rivet and consequent widening of the rivet hole.

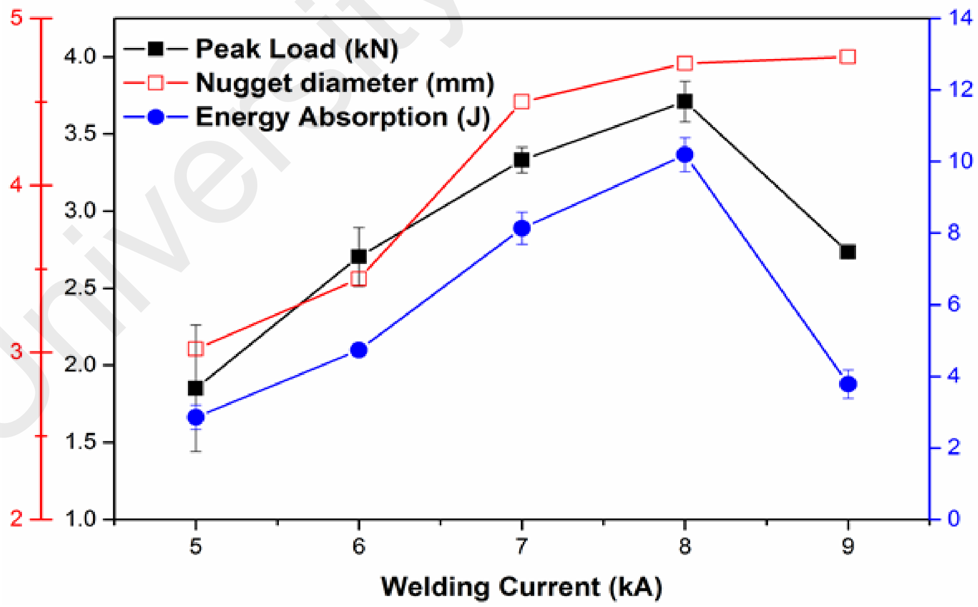

Figure 4.37: Nugget diameter, peak load, and energy absorption of REW joints as a function of welding current

Figure 4.38 compares the maximum peak load and maximum energy absorption of REW and RSW joints. Overall, the REW joints showed superior tensile shear performance. The peak load obtained by REW was 3.71 kN, which is 63% higher than that obtained by RSW. The benefits of the REW are reflected mainly in its superior energy absorption capability, which is a very important parameter that guarantees vehicle crashworthiness. The maximum energy absorption obtained by RSW was just 1.14 J, while that obtained by REW was 10.2 J, representing a nine times increase. This diference in energy absorption can be attributed to differences in failure mode, as discussed in section 4.35. It is interesting to note that the energy absorption obtained by REW in this study is higher than that obtained during traditional RSW of 2 mm AZ31B Mg alloy/1.2 electro-galvanized DP600 steel with hot-dip galvanized Q235 steel interlayer (5.1J) and without interlayer (2.4J) (Feng et al., 2016b). Moreover, the REW required lower welding currents. The peak load and maximum energy of the REW and RSW joints were obtained at a welding current of 8kA and 14 kA, respectively.

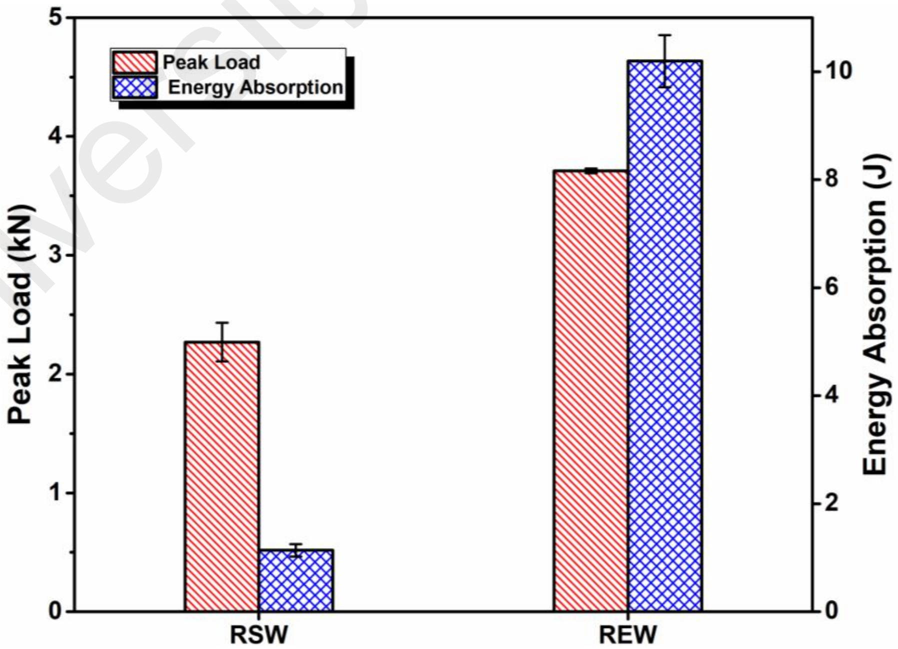

Figure 4.38: Comparison of the peak load and maximum energy absorption of the joints produced by RSW and REW

4.3.5 Failure mode

While all the RSW joints failed in IF mode (section 4.1.5), both IF and PO failure modes were observed in the case of REW joints. IF mode occurred at a welding current of 5 kA, and the failure mode changed to PO with further increase in welding current. The IF to PO mode transition is an important phenomenon that governs the mechanical performance of spot welds, and it is influenced by nugget diameter (Pouranvari, 2017). Failure mode is a competition between crack propagation through the FZ (IF) and necking at failure location (PO) (Pouranvari, 2017). At lower welding currents, where the nugget size is small, the shear stress at the sheet/sheet interface would reach its minimum value before necking takes place in the BM, leading to IF. As the nugget diameter increases, its resistance to IF mode increases. Upon reaching a critical nugget diameter, the failure mode would transit to PO (Safanama et al., 2012).

Figure 4.39 compares the load-displacement curves of the RSW and REW joints that failed in IF mode. It is seen that the RSW joints failed abruptly after reaching the peak load. This accounts for the low energy absorption of the traditional RSW joint. This kind of failure mode is detrimental to vehicle crashworthiness. On the other hand, the curve for the REW joint that failed in IF mode suggested that some degree of plastic deformation had occurred before final failure. The load-displacement curve for the REW joint that failed in PO (Figure 4.40) dropped slowly after reaching its peak load, indicating a ductile failure.

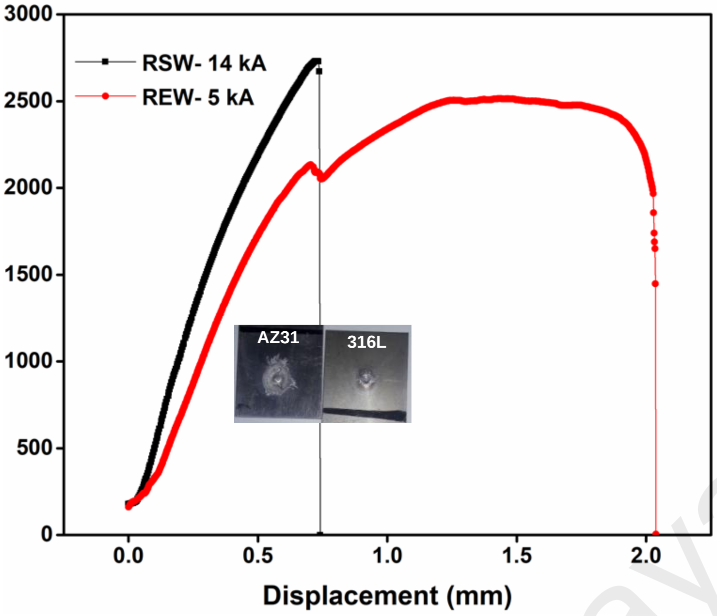

Figure 4.39: Typical load-displacement curves for REW and RSW joints that failed in IF mode

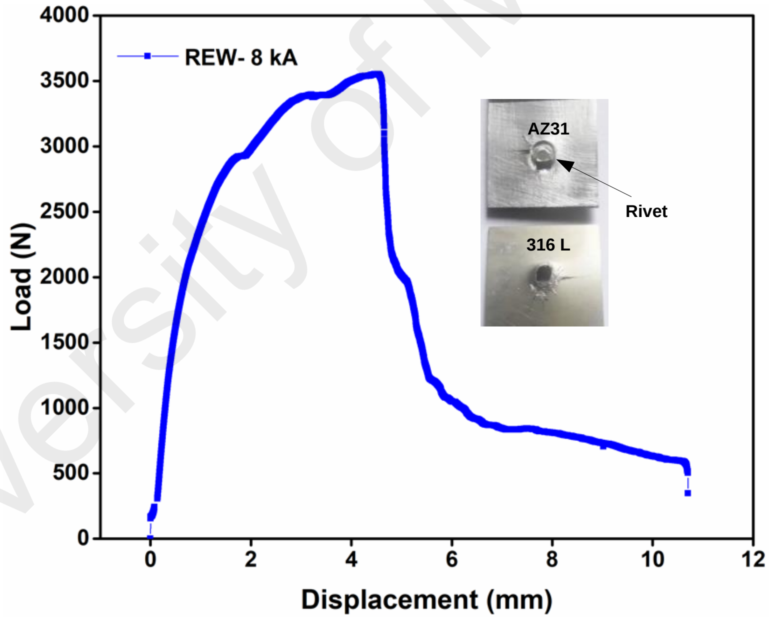

Figure 4.40: Typical load-displacement curve for REW joint that failed in PO mode

Figure 4.41 shows the fracture surface morphology of the REW joint that failed in IF mode. It is seen from Figures 4.41 a and d that the fracture surfaces can be divided into two regions (region1 and region 2). Region 1 corresponds to the region of crack initiation while region 2 corresponds to the region of crack propagation. Higher magnification images of region 1on both sheets (Figures 4.41 b and e) exhibit cleavage characteristics, indicating a brittle failure. On the other hand, higher magnification images of region 2 (Figures 4.41 c and f) indicate quasi-cleavage failure, with combined ductile and brittle microscopic characteristics. The fracture surface of the REW joint that failed in PO mode is shown in Figure 4.42, showing much larger and deeper dimples, indicating a ductile fracture.

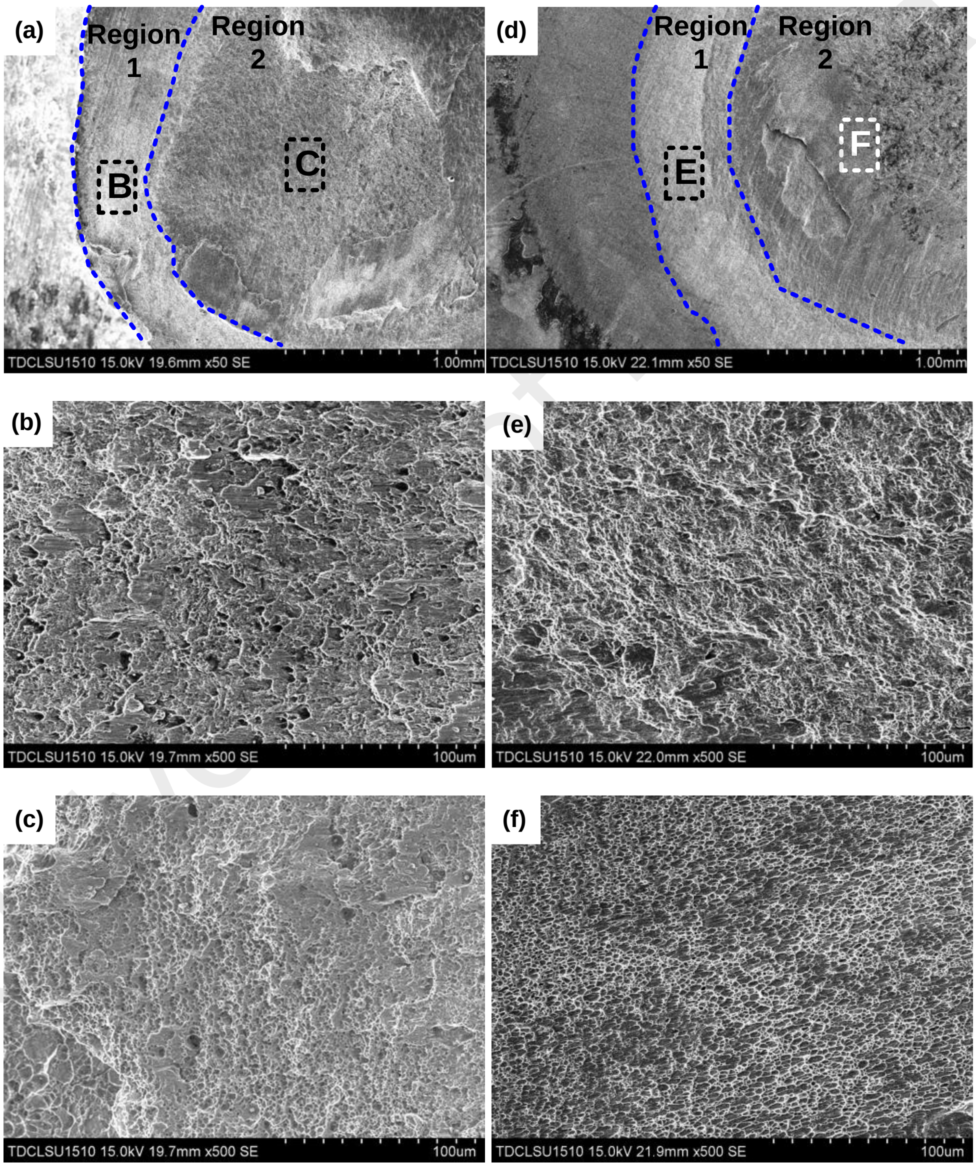

Figure 4.41 : Fracture surface of REW joint that failed in IF mode: (a) Q235 steel side; higher magnification of (b) region B in (a); (c) region C in (a); (d) 316L ASS side; higher magnification of E in (d); (f) region F in (d)

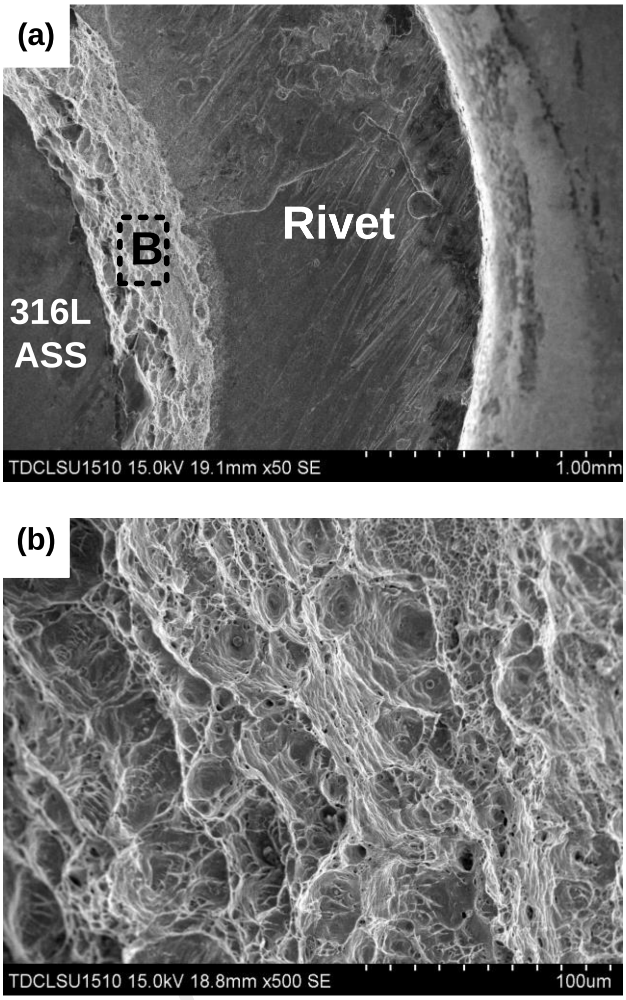

Figure 4.42: Fracture surface of REW joint that failed in PO failure mode: (a) macroscopic morphology; (b) higher magnification of region B in a

4.4 REWB joints

4.4.1 Macrostructure and microstructural evolution

The typical macroscopic morphology of the REWB joints is shown in Figure 4.43 a. Interestingly, the symmetry of the nugget is improved significantly compared to that of REW joint (Figure 4.32 a), in which the nugget is mainly in the Q235 steel. This suggests that the addition of adhesive layer improves the heat balance. It can be seen from Figure 4.43 b that that adhesive is present at the edge of the nugget. Therefore, the joint can be divided into two zones, the weld zone and the adhesive zone. Furthermore, as indicated by white dotted line in Figure 4.43a, the Mg alloy around the rivet melted and braze-welded to the rivet. The microstructure of the Mg alloy nugget consists of CDZ, as shown in Figure 4.43 c.

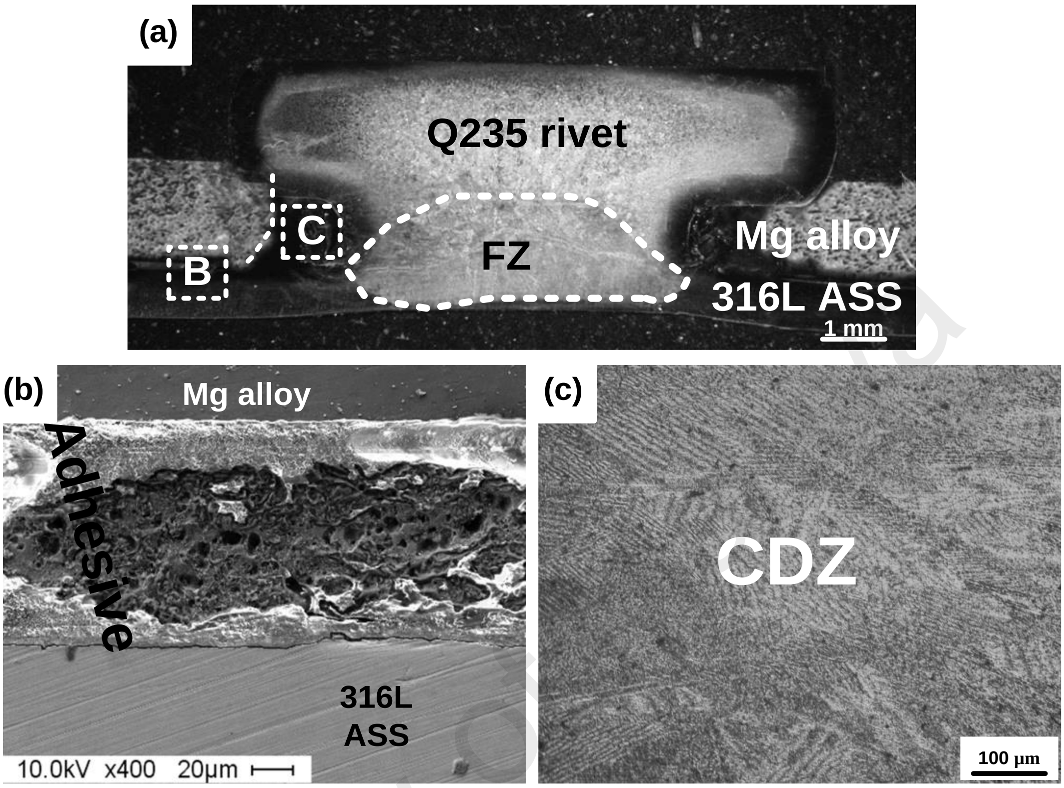

Figure 4.43: (a) Macroscopic morphology of REWB joint; (b) higher magnification of region B in (a); (c) higher magnification of region C in (a)

Figure 4.44 compares the typical microstructures in the FZ of REW and REWB joints. Similar to the REW joint, a two-zone nugget also formed in the REWB joints. Furthermore, the microstructures in different zones of the nuggets are similar.

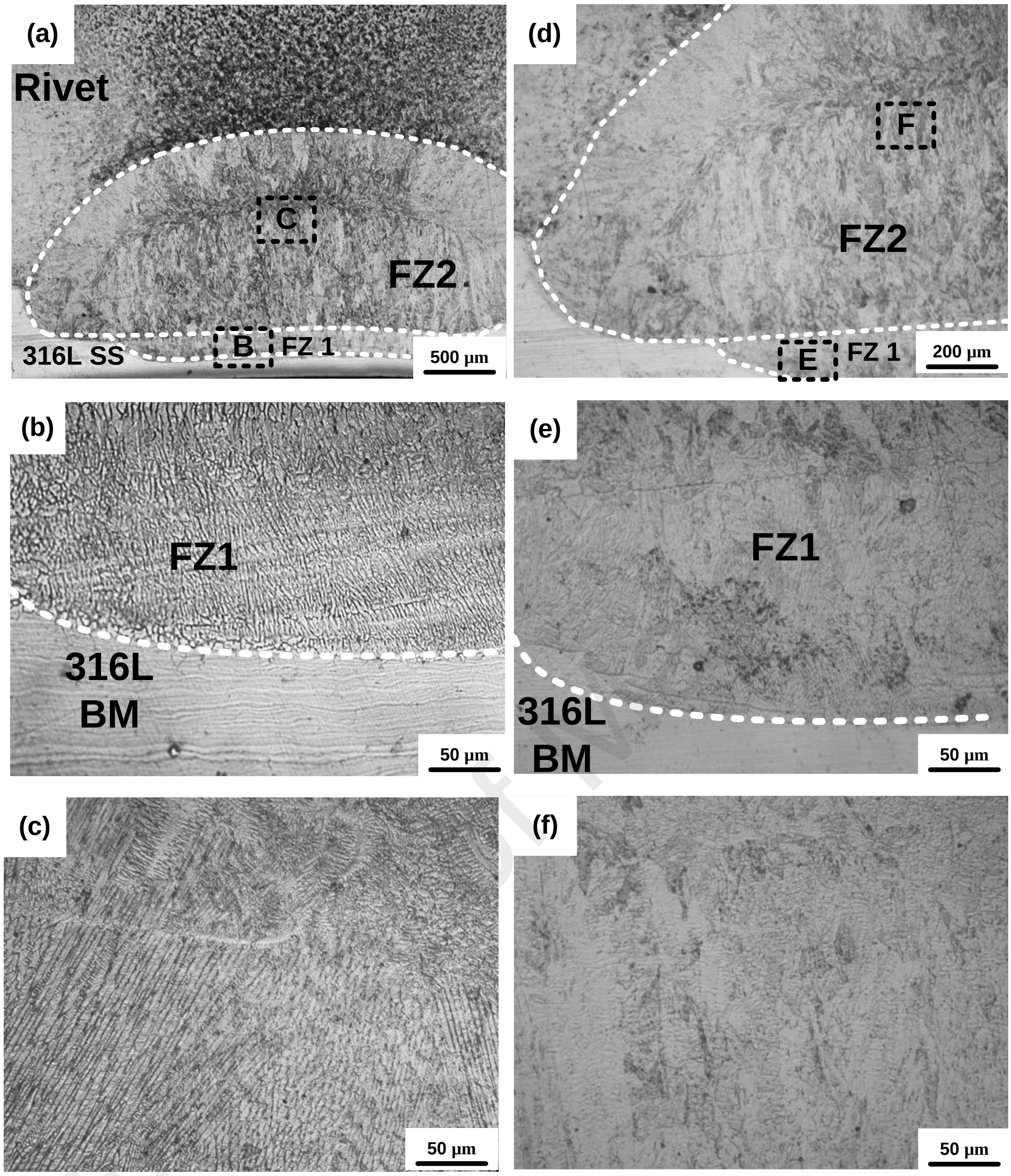

Figure 4.44: Comparison of the FZ microstructure for REW and REWB joints: (a-c) REW joint; (d-f) REWB joint

As discussed in section 4.3.1, the HAZ in the Q235 steel side of the REW joint could be divided into two distinct zones, namely, UCHAZ and ICHAZ. The UCHAZ could further be divided into coarse-grain zone (CGUCHAZ) and fine-grain zone (FGUCHAZ). The microstructure of the UCHAZ consists mainly of martensite.

Martensite is formed by a diffusionless reaction involving shear-type deformation of the parent austenite, leading to a change in shape and volume expansion of the transformed region. As a result of the constraining effect of its surroundings, martensite forms as thin plates or laths to reduce the strain energy arising from the deformation. Lath martensite is usually formed in carbon steels with a carbon content that is less than 0.6 wt.%. During the transformation of austenite to martensite, the crystallographic orientation relationships are retained; thus martensite is highly crystallographic (Kitahara et al., 2006; Krauss, 1999). Figure 4.45 schematically illustrates a typical lath martensite structure, having a three-level hierarchy, consisting of martensite lath, block, and packet. The lath refers to a single crystal of martensite. The block is composed of laths having the same crystallographic orientation. The packet is composed of blocks with the same habit plane in the prior austenite. Several packets may form in a single prior austenite grain (Kitahara et al., 2006; Tamizi et al., 2017).

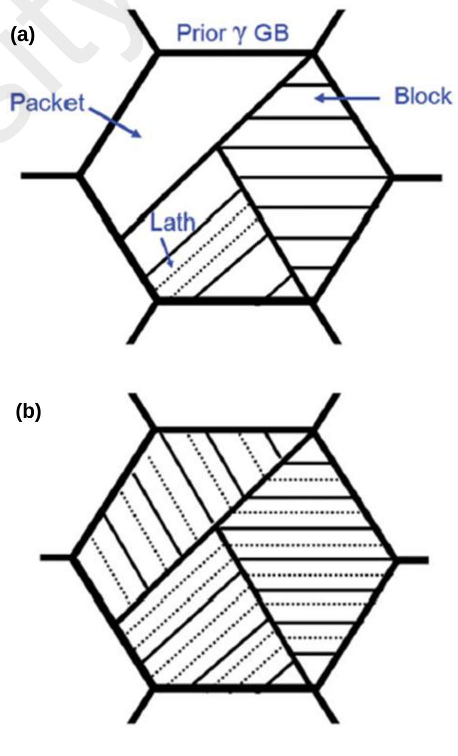

Figure 4.45: Schematic illustration of typical lath martensite structure: (a) three-level microstructural hierarchy of lath, block, and packet; (b) full martensitic structure (Kitahara et al., 2006; Tamizi et al., 2017)

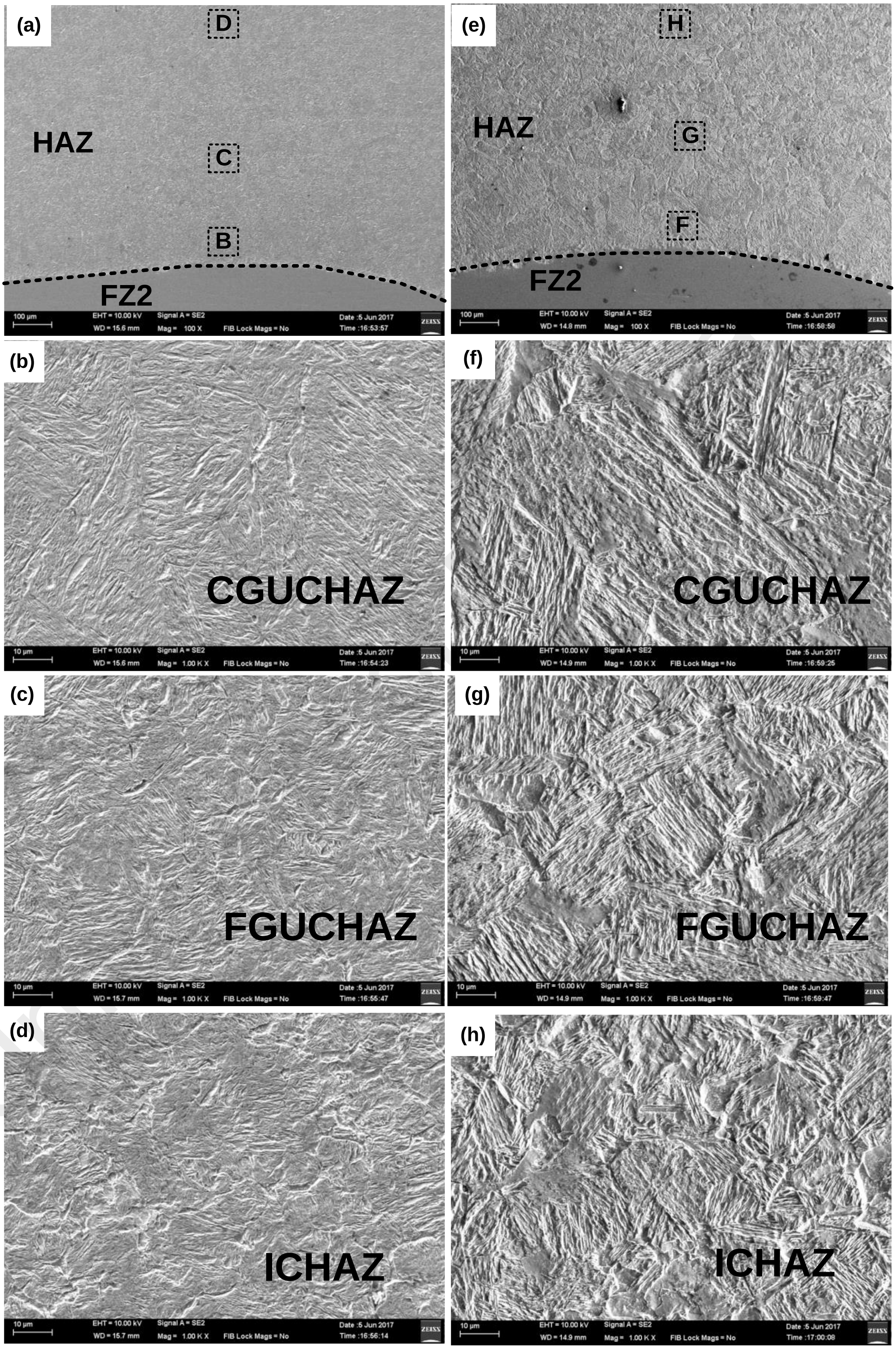

Figure 4.46: Comparison of the microstructures in the HAZ of REW and REWB joints: (a-d) REW joint; (e-h) REWB joints

Figure 4.46 shows FESEM images comparing the microstructures in the CGUCHAZ, FGUCHAZ, and ICHAZ of the REW and REWB joints. The microstructures in the CGUCHAZ and FGUCHAZ of both joints consists of lath martensite, with fine pocket size. However, in both zones, the proportions of martensite are higher in the REWB joints and the packet and lath sizes are larger, which is probably as a result of the enrichment of carbon content from the decomposed adhesive. Furthermore, while the microstructure of the ICHAZ of REW joint consisted of little pockets of martensite, that of REWB joints consisted mainly of martensite, despite the fact the ICHAZ experienced much lower cooling rate than the UCHAZ. This is as a result of the higher hardenability of the carbon-rich austenite (Tamizi et al., 2017).

4.4.2 Interface characteristics

Referring to Figure 4.43b, a gap appears at the adhesive/316L ASS interface. Higher magnification FESEM image (Figure 4.47) indicate that the gap is as a result of some micro-connection defects at the interface. These defects are not observed at the Mg alloy/adhesive interface. Furthermore, they were not observed at the adhesive/316L ASS interface in RSWB. It should be recalled that in the RSWB process, the ASS did not melt. However, in the REWB process, the ASS melted along with the Q235 steel rivet to form the nugget. The formation of these defects is probably because of the increased heat generation in the ASS sheet. Although these defects could reduce the effective connection area, they did not affect the overall joint strength. However, they resulted in change of fracture path, as shall be discussed in section 4.4.5. Micro-connection defects have also been observed by Feng et al. (2016a) at the adhesive/Al interface of adhesive bonded joints.

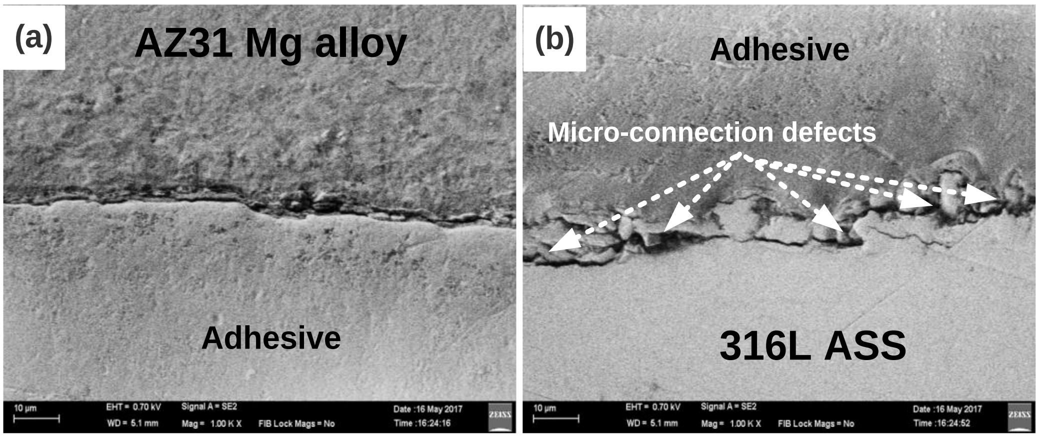

Figure 4.47: Higher magnification FESEM image of (a) Mg alloy/adhesive interface; (b) adhesive/316L ASS interface

Figure 4.48 shows the elemental mapping of the Mg alloy/adhesive/ASS interface in the adhesive zone of the joint (region B in Figure 4.43a). It is seen that there was virtually no inter-diffusion of Fe, Ni, and Cr across the interface. The adhesive is composed mainly of C and then oxygen. It can be seen from Figures 4.48 e and f that the C is concentrated mainly at the Mg alloy/adhesive and adhesive/ASS interface, while the oxygen is concentrated mainly in the center of the adhesive. This suggests that the bonding is achieved mainly by the interaction between C and the adherends. It can also be seen that the Mg element diffused across the Mg/adhesive interface, through the C concentration area, and then react with oxygen and segregated at the center of the adhesive.

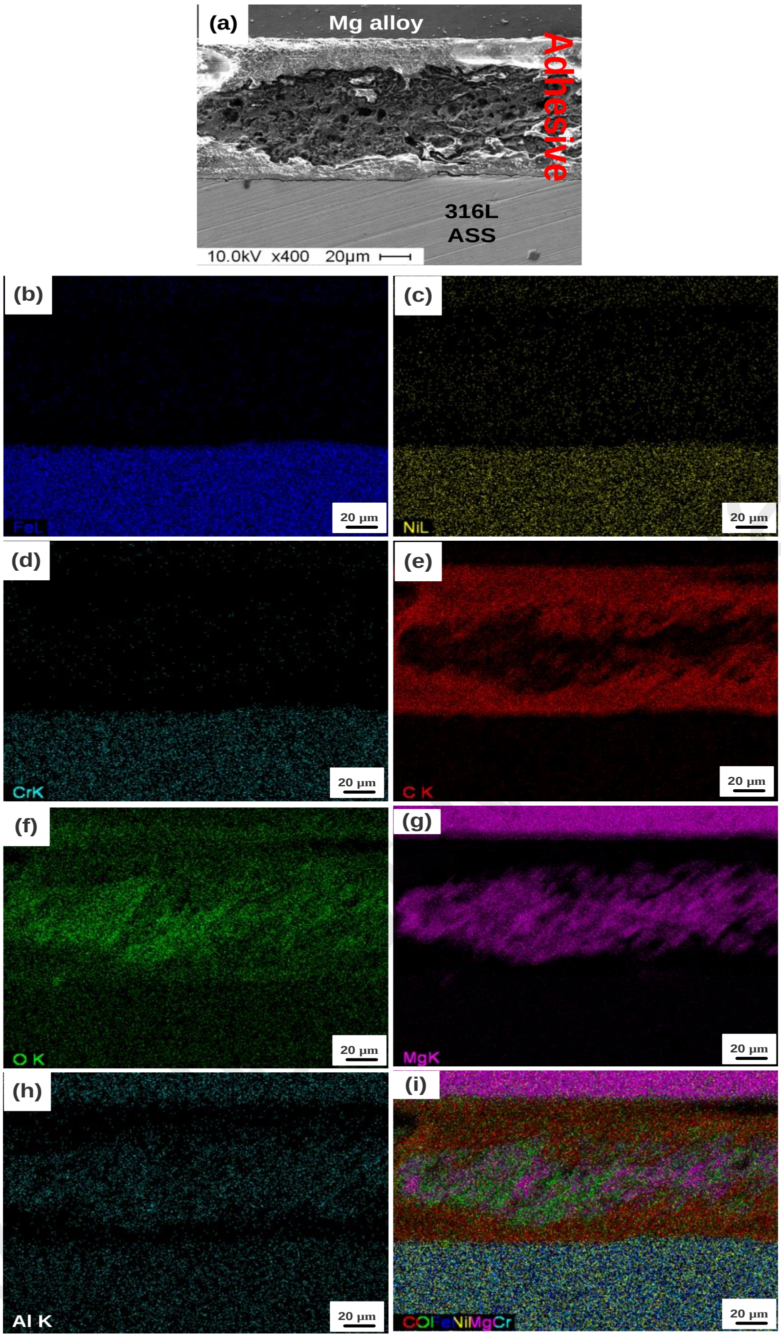

Figure 4.48: Elemental mapping of the adhesive zone of the REWB joints (region B in Figure 4.43)

4.4.3 Hardness characteristics

The average hardness in different zones of the REW and REWB joints is compared in Figure 4.49. The average hardness value in the FZ, UCHAZ, and ICHAZ were found to be slightly higher in the case of REWB joints. This slight difference is probably because the FZ of the REWB joints is enriched with carbon from the adhesive, which would increase its hardenability. A similar phenomenon was observed by (Ma et al., 2012) while investigating the laser spot weld-bonding (LSWB) and laser spot welding (LSW) of Q195 mild steel. The adhesive, having carbon as its major constituent, decomposed during the LSWB process because of its low boiling point compared to the melting point of the BM. Consequently, some carbon diffused into the weld pool, in which it is redistributed uniformly as a result of fluid flow, thereby changing the microstructure of the joint.

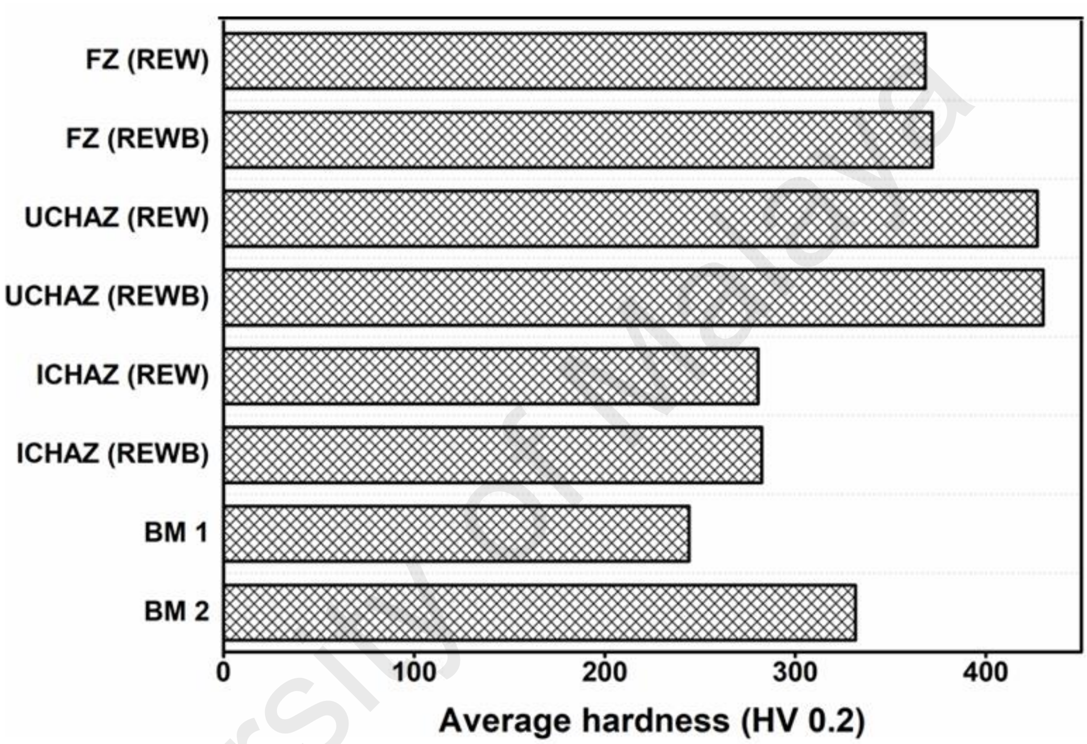

Figure 4.49: Comparison of typical hardness profiles of REW and REWB joints

4.4.4 Tensile-shear performance

Nugget diameter is the main factor governing the mechanical performance of spot welds. Figure 4.50 compares the nugget diameters for REW and REWB joints as a function of welding current. For both processes, the nugget diameter increased progressively with increased in welding current because of increased heat generation and volume of melted metal. However, for the same value of welding current, the nugget diameter of the REWB joints is higher. Again, this is because the addition of adhesive increased the dynamic resistance and consequently heat generation.

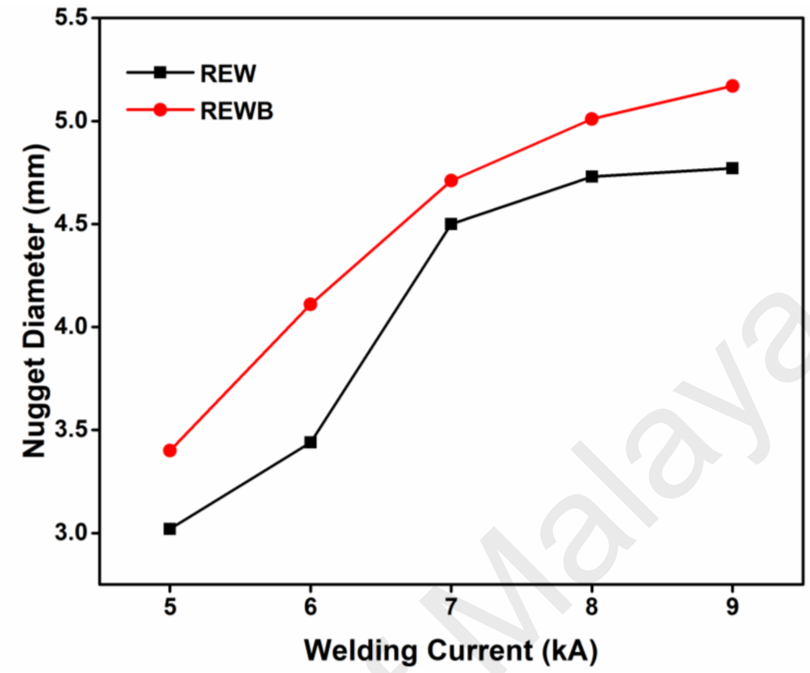

Figure 4.50: Nugget diameter of REW and REWB joints as a function of welding current

As shown in Figures 4.51 and 4.52, the peak load and energy absorption of the REW joints increased sharply with increased welding current, reached their maximum values at a welding current of 8 kA, and then dropped significantly with further increase in welding current due excessive heat input, which led to widening of the rivet hole in the Mg alloy. On the other hand, the peak load of the REWB joints increased relatively slowly with increased welding current and reached a maximum value at a welding current of 8kA and then dropped slightly. This indicates that the welding current and consequently nugget diameter has lesser influence on the tensile-shear performance of the REWB joints than it has on the REW joints, probably because the load was sustained mainly by the adhesive zone. However, for the same value of welding current, the peak load and energy absorption of the REWB joints are significantly higher. Furthermore, as illustrated in

Figure 4.51, while the REW joints satisfied the minimum strength requirement of AWS D17.2 only at a current of 8kA, all the REWB joints easily satisfied this strength requirement.

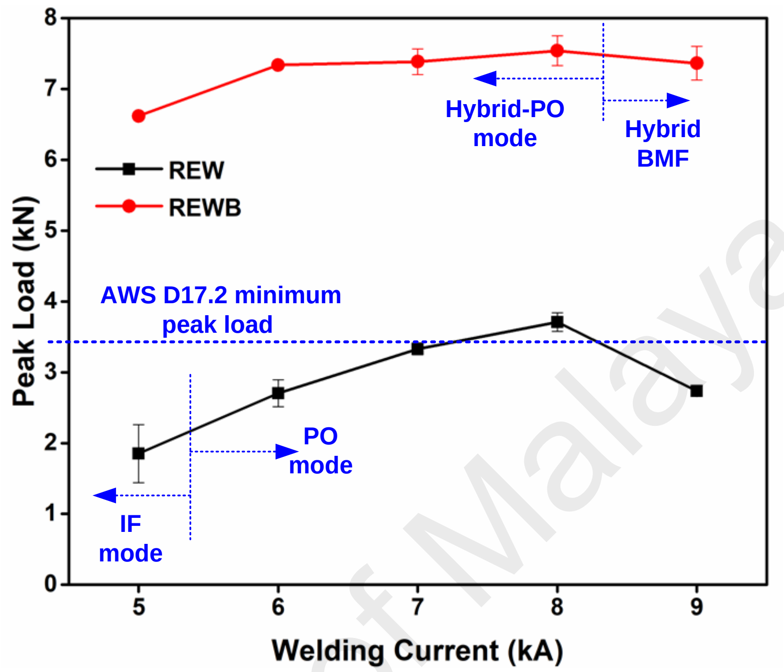

Figure 4.51: A comparison of the peak load of REW and REWB joints as a function of welding current

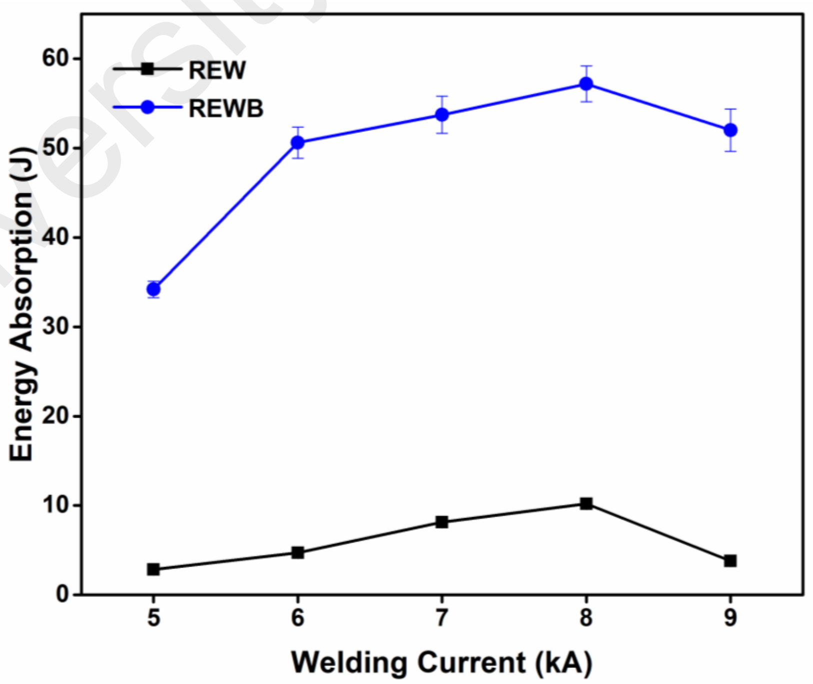

Figure 4.52: A comparison of the energy absorption of REW and REWB joints as a function of welding current

The maximum peak load and energy absorption of the joints produced by REW, AB, and REWB are compared in Figure 4.53. While the peak load of the AB joints (4.70 kN) is higher than that of REW joint (3.71 kN), the energy absorption of the REW joints (10.19 J) is higher than that of the AB joints (8.41 J). The two processes complemented each other in the REWB process to obtain a high peak load (7.54 kN) and outstanding maximum absorption (57.19 J).

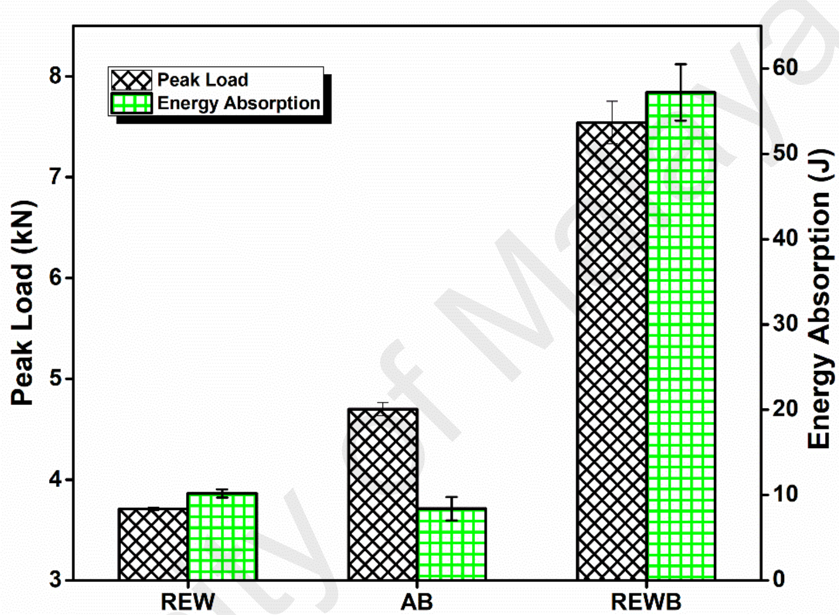

Figure 4.53: Comparison of the peak load and maximum energy absorption of REW, AB, and REWB joints

4.4.5 Failure mode

Two types of modes were observed in the REWB joints. The first one is shown in Figure 4.54 and the second one in Figure 4.56. From the surface morphology shown in Figure 4.54 and the results of EDS analysis shown in Figure 4.55, it can be seen that the first failure mode is a hybrid failure mode involving pull out failure with tearing in the ASS, delamination at both Mg/adhesive and adhesive/ASS interfaces, and cohesive failure. This type of failure mode has not been reported in the literature, and in this work, it is termed as hybrid-pull out failure mode (hybrid-PO). It is important to note that, as seen in section 4.2.4, the failure mode in AB and RSWB joints did not involve delamination at the adhesive/ASS interface. Its occurrence in the REWB joints can be attributed to the presence of micro-connection defects at the adhesive/ASS interface, as discussed in section 4.4.2. The second failure mode (Figure 4.56) involves delamination at the adhesive/Mg alloy interface in the adhesive zone and base metal fracture (BMF) in the Mg alloy. In this work, this failure mode is termed hybrid-BMF. BMF was also observed by Ling et al. (2016), while studying the mechanical performance of 2-mm-thick 6061-T6 Al alloy/1.8-mm-thick 22MnMoB boron steel joints produced by REW.

As indicated in Figure 4.51, the hybrid-PO failure occurred at welding current of 5-8 kA, and then the failure mode changed to hybrid-BMF at welding current of 9 kA. This changed in failure mode can be attributed to increase in nugget dimeter (Figure 4.50).

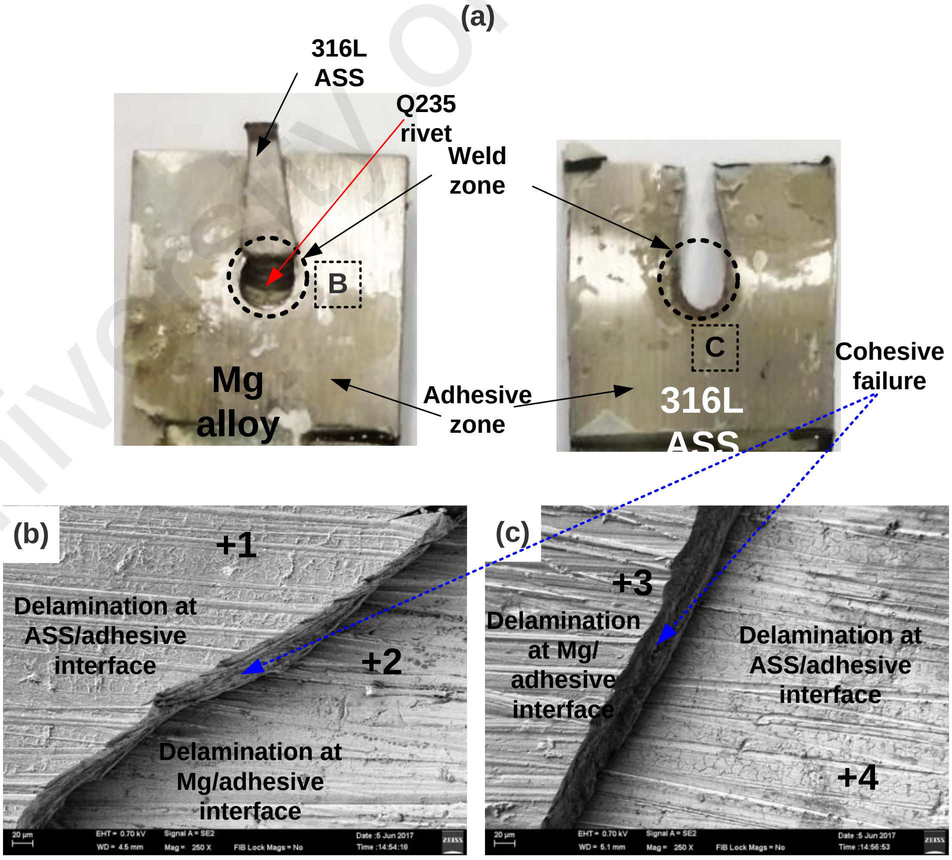

Figure 4.54: Fracture surface of REWB joints that failed in hybrid-PO mode: (a) Mg alloy and ASS sides; (b) higher magnification of regions B in (a); (c) higher magnification of region C in (a)

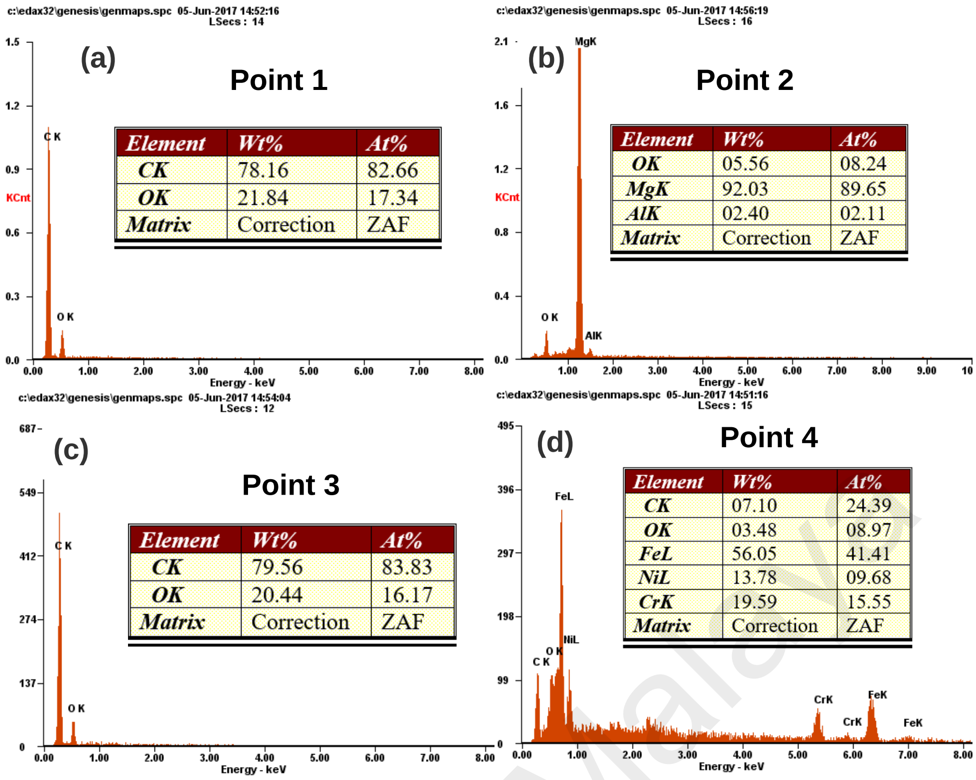

Figure 4.55: EDS spectrum of points 1-4 in Figure 4.54

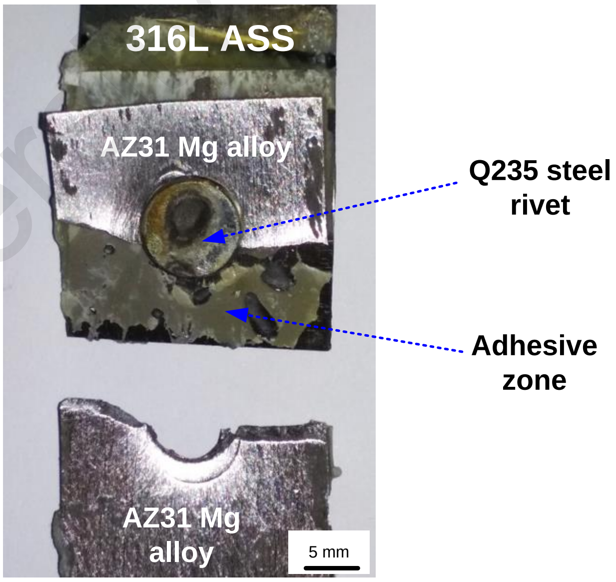

Figure 4.56: Fracture surface of RSWB joint that failed in hybrid-BMF mode

Figure 4.57 compares the load-displacement curves for AB, REW, and REWB joints. The peak point and extension at failure for REWB joints that failed in hybrid-PO are slightly higher than those with hybrid-BMF. The curve for both types of failure mode can be divided into five stages, i.e, 1, 1’, 2,3, and 4. In stage 1, the load increased rapidly and reached approximately the same value with that of AB joint, indicating that the load was sustained mainly by the adhesive. In stage 1’, the load increased progressively at a relatively lower rate, as both the adhesive and the nugget are deformed. The maximum peak load is attained at the end of this stage. With further deformation, the load bearing capacity dropped abruptly as a result of the complete fracture of the adhesive (stage 2). Thereafter, the load was sustained by the nugget in the case of hybrid-PO and by the Mg base metal in the case of hybrid-BMF (stage 3). The curve reached another peak point as the load is sustained and then the joints finally failed (stage 4), slowly in the case of hybrid-PO mode and rapidly in the case of hybrid-BMF. Thus, the final fracture surface of the joint with hybrid-PO mode exhibits ductile fracture characteristics (Figure 4.58) while that with hybrid-BMF exhibits brittle fracture characteristics (Figure 4.59).

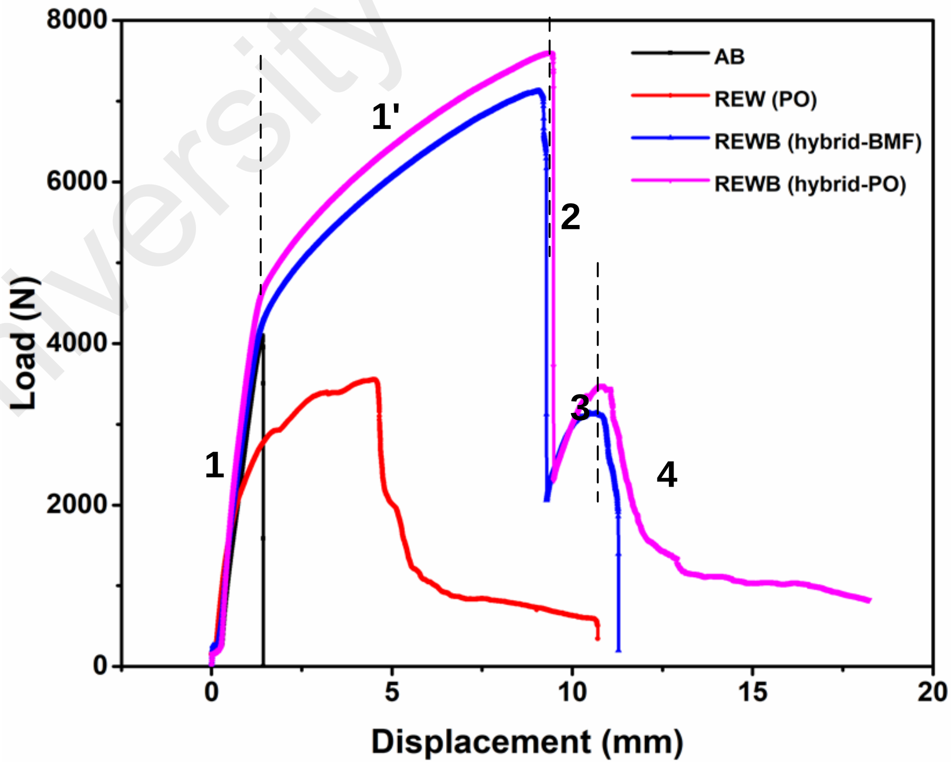

Figure 4.57: Comparison of load-displacement curves for AB, REW, and REWB joints

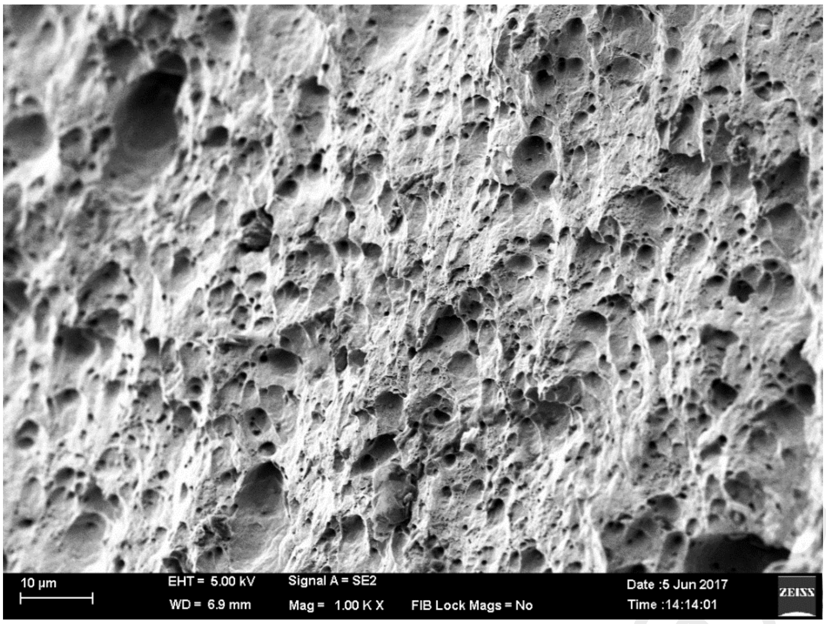

Figure 4.58: Fracture surface of REWB joint that failed in hybrid-PO mode in the ASS

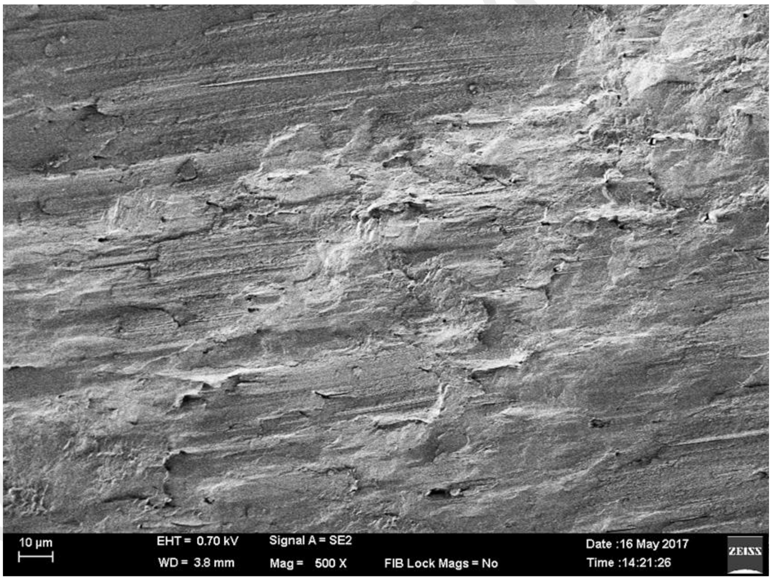

Figure 4.59: Fracture surface of REWB joint that failed in hybrid-BMF in the Mg alloy

It is important to note that, to guarantee crashworthiness, the peak load and energy absorption for both failure modes are taken at the first peak point (end of stage 1' in Figure 4.57), since the load sustained at the first peak is significantly higher than that in the second peak point. Thus, the final fracture mode did not have much effect on the peak load and energy absorption of the joint. This is an important advantage of the REWB joints.

It is interesting to note that the behavior of the REWB hybrid-PO curve in stages 3 and 4 (Figure 4.57) is similar to that of REW that failed in PO mode (REW(PO)). However, the peak load for the hybrid-PO at these stages is slightly lower because the nugget has already been weakened in the previous stages.

4.5 General comparison of the tensile-shear performance of the joints

The typical load displacement curves for the joints produced by RSW, AB, RSWB, REW, and REWB is shown in Figure 4.60. Overall, the REWB and RSWB joints exhibits the most superior tensile-shear performance. Particularly, the energy absorption of the REWB joints is outstanding. On the other hand, the RSW joints show the worst tensile-shear performance. Especially, the energy absorption of the RSW joints, which is an important parameter that guarantees vehicle crashworthiness, is very poor. These shows that the hybrid combination of RSW and AB and especially REW and AB is an important technology for producing strong and reliable Mg alloy/ASS joints.

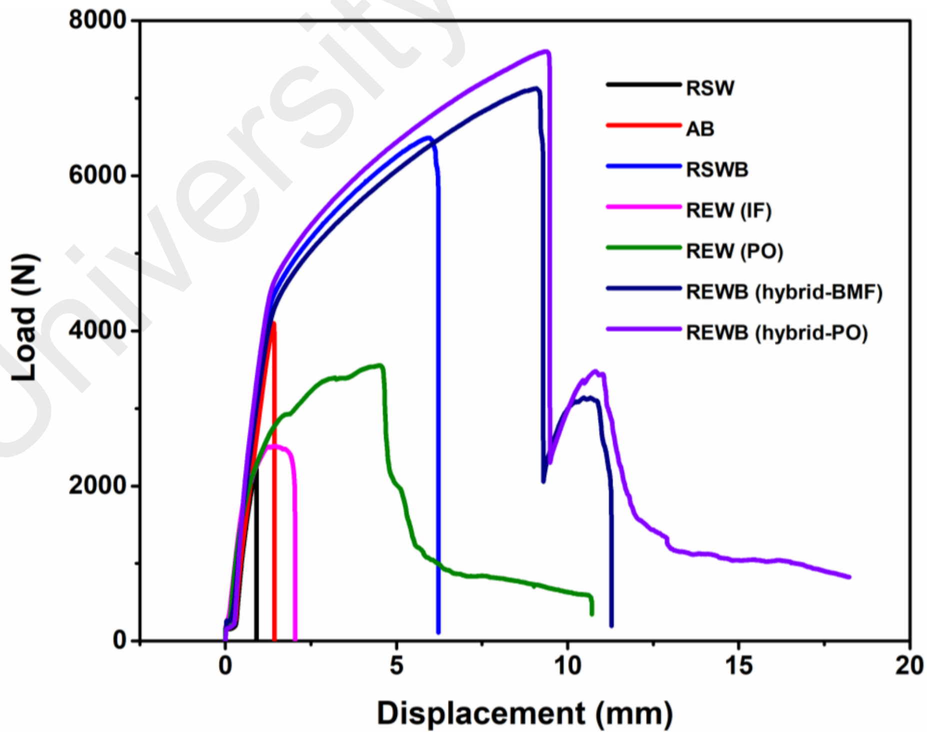

Figure 4.60: Comparison of typical load-displacement curves for RSW, AB, RSWB, REW, and REWB joints

The maximum peak load and energy absorption of the joints are compared in Figure 4.61. The maximum peak load of the RSW joint is 2.23 kN and the energy absorption is just 1.13J. Compared with the RSW joints, the REWB showed approximately 238 % higher peak load (7.54 kN) and 51 times higher energy absorption (57.2 J); RSWB joints showed approximately 187 % higher peak load (6.4 kN) and 24 times higher energy absorption (27.2 J); AB joints showed approximately 111% higher peak load (4.7 kN) and 7 times higher energy absorption (8.4 J); and the REW joints showed approximately 66% higher peak load (3.71 kN) and 9 times higher energy absorption (10.19 J).

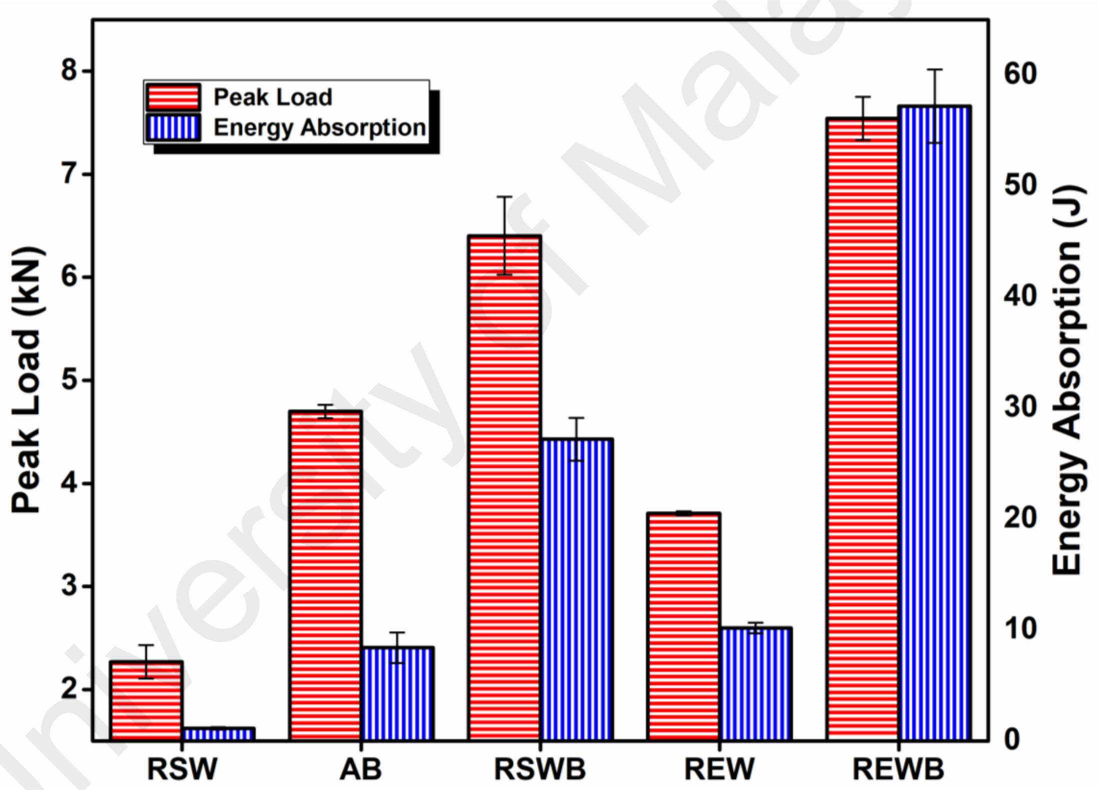

Figure 4.61: A comparison of the peak load and energy absorption of RSW, AB, RSW, REW, and RSWB joints

The tensile shear performance of the REW, RSWB, and REWB joints are compared with the results available in the literature (Figures 4.62 and 4.63). It is should be noted that Mg/DP-1, Mg/DP-2, Mg/DP-3, and Mg/Mg stand for 1.5-mm-thick AZ31B Mg alloy/1.2-mm-thick zinc-coated DP600 steel (Liu et al., 2010b), 2-mm-thick AZ31B Mg alloy /1.2-mm-thick electro-galvanized DP600 steel (Feng et al., 2016b), 2-mm-thick

AZ31B Mg alloy /1.2-mm-thick electro-galvanized DP600 steel with 0.6-mm-thick hot-dip galvanized Q235 steel interlayer (Feng et al., 2016b), and 1.5-mm-thick AZ31 Mg alloy/1.5-mm-thick AZ31 Mg alloy (Liu et al., 2010b). It can be seen that the peak loads of the REWB and RSWB joints obtained in the present study are significantly higher, despite the fact the thickness of the steel used in (0.7 mm) is significantly smaller than those in Mg/DP-1, Mg/DP-2, and Mg/DP-3 joints. Interestingly, the peak load of the RSWB and REWB joints is even higher than that of optimized Mg/Mg alloys.

As shown in Figure 4.63, the superiority of the RSWB and RSWB joints is reflected more clearly in their energy absorption capability. The energy absorptions of the joints are significantly higher than those of Mg/DP-2 and Mg/DP-3. It should also be noted that the energy absorptions of Mg/DP-1 and Mg/Mg were not reported in the literature (Liu et al., 2010b). Therefore, they are not included in Figure 4.63.

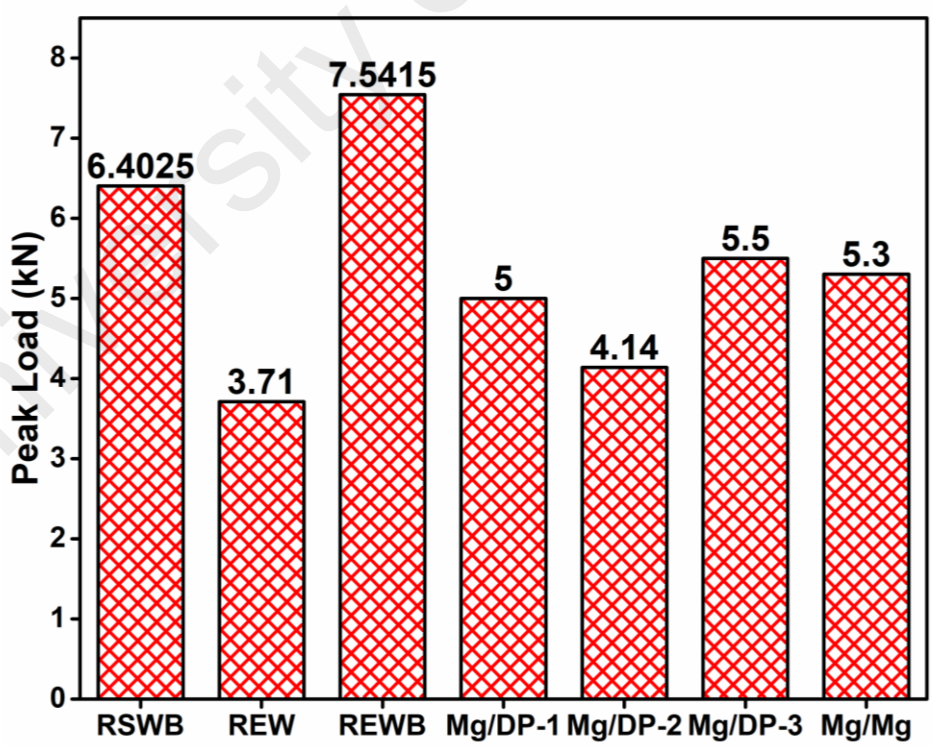

Figure 4.62: Comparison of peak load of REW, RSWB, REWB joints and the results obtained in the literature

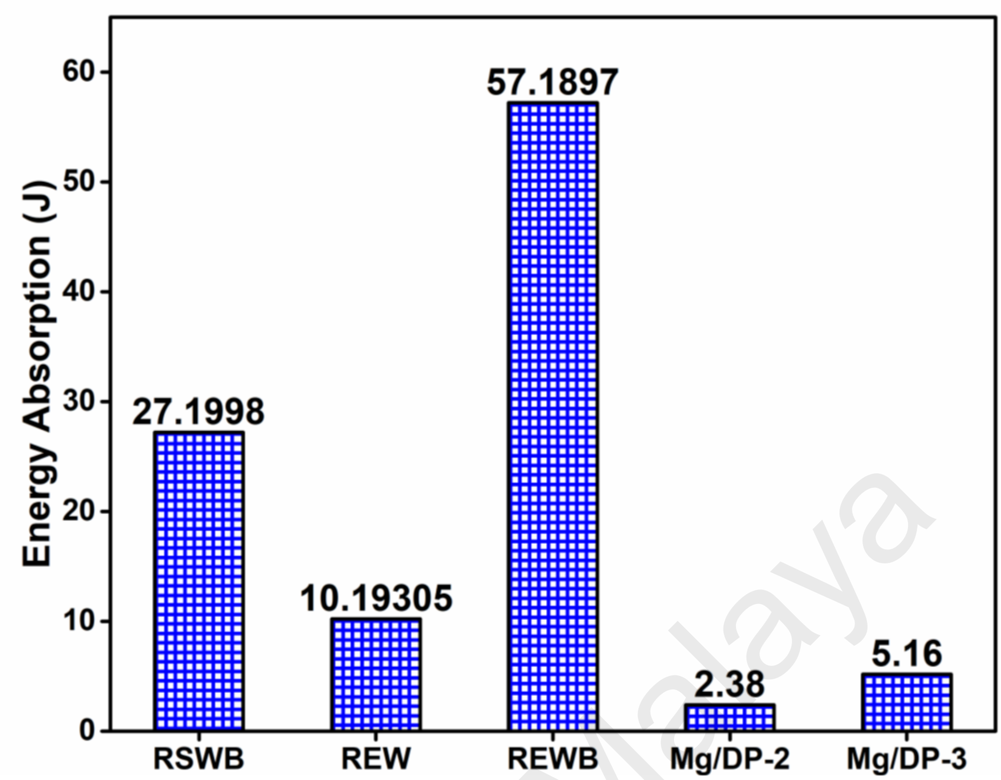

Figure 4.63: Comparison of energy absorption of REW, RSWB, REWB joints and the results obtained in the literature

Furthermore, Figure 4.63 compares the tensile shear performance of the RSWB and REWB joints to that of optimized 1mm 316L ASS similar RSW joints (ASS/ASS) (Kianersi et al., 2014a). The peak load of the REWB and RSWB joints reached 94% and 80% that of the ASS/ASS joints. The energy absorption of the REWB joints reached 1.63 times that of the ASS/ASS joints, while the energy absorption of the RSWB joints only reached 77% that of the ASS/ASS joints. Therefore, the REWB process could be a reliable technique to produce Mg alloy/steel joints that guarantee vehicle crashworthiness.

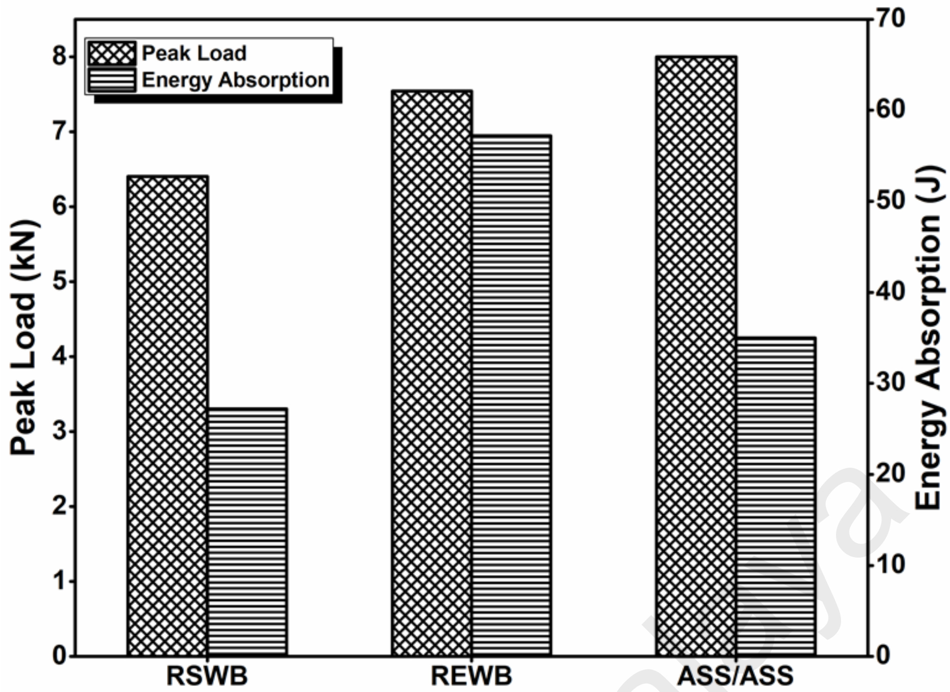

Figure 4.64: Comparison of the peak load and energy absorption of RSWB, REWB, and optimized 1mm ASS/ASS sjoints

CHAPTER 5: CONCLUSIONS

In this research, 1.5-mm-thick AZ31 Mg alloy and 0.7-mm-thick 316L ASS were joined using RSW, AB, RSWB, REW, and REWB techniques. The microstructural evolution and mechanical performance of the joints were studied using optical microscopy, scan electron microscopy, EDS analysis, micro-hardness test, and tensile-shear tests. The following conclusions have been drawn based on the objectives of this study.

1. The RSW joints were produced through welding-brazing mode, in which the Mg alloy melted and spread on the solid steel, forming a nugget only on the Mg side. For the REW joints, a two-zone FZ, consisting of peripheral FZ on the ASS side and main FZ, was observed.

2. RSW produced joints with poor mechanical properties. The peak load of the REW joints was 63% higher than that of RSW joints, and the maximum energy absorption was 9 times higher. Irrespective of the welding current, all the RSW joints failed via IF mode, while the failure mode of the REW joints transited from IF to PO with increase in welding current.

3. Both the REWB and RSWB joints consisted of two zones, namely, the adhesive zone and weld zone. The weld zone of the REWB joints was formed through a metallurgical reaction between molten rivet and molten ASS. The weld zone of the RSWB joints was formed through welding-brazing involving molten Mg alloy and solid ASS, and the nugget was formed only in the Mg alloy

4. The macroscophic morphology and microstructures of the RSWB and REWB joints were similar to those of traditional RSW and REW joints, respectively. However,

compared with the RSW and REW joints, the RSWB and REWB joints possessed larger bonding diameter and nugget diameter, respectively.

5. RSWB and especially REWB could be reliable techniques to produce Mg alloy/ASS joints with high peak load and outstanding energy absorption. Compared with the RSW joints, the REWB showed approximately 238 % higher peak load and 51 times higher energy absorption; and the RSWB joints showed approximately 187 % higher peak load and 24 times higher energy absorption.

6. The RSWB joints exhibited a hybrid failure mode comprising of delamination at the Mg/adhesive interface, cohesive failure in the adhesive, and interfacial failure. With increase in welding current, the failure mode of the REWB joints changed from hybrid failure mode involving delamination at both the Mg/adhesive and adhesive/ASS interfaces, cohesive, and pullout failure to a hybrid failure involving delamination at Mg/adhesive interface and failure in the Mg alloy

5.1 Suggestions for further work

This research has demonstrated that REW produces Mg/ASS joints with better mechanical performance than conventional RSW. Further, it has shown that a hybrid combination of RSW and AB, and especially REW and AB could produce reliable Mg/ASS joints with a combination of high peak load and superior energy absorption. However, further work needs to be conducted for the technique to be fully implemented in actual production line for joining Mg alloy/steel components. The following suggestions are made:

1. Fatigue is the most critical failure mode of spot-welded and weld-bonded joints in automobiles. A profound understanding of the fatigue behavior of the joints is required to ensure the integrity, durability, and safety of welded structures. A detailed study should be conducted to study and compare the fatigue behavior of the joints produced by the various techniques used in this study.
2. Numerical modelling is now used as a powerful tool for process parameter optimization, weld nugget formation and quality prediction, and heat distribution, etc. Thus, it will be of paramount importance to conduct numerical modelling of the Mg alloy/ASS joints during RSW, REW, RSWB, and REWB to offer comprehensive solution to the manufacturing industry.
3. Corrosion is important to the life of transportation structures, and it is a major concern for multi-material design due to differences in corrosion potentials. A study should be conducted to understand the corrosion mechanism of the joints and to develop adequate protection measures.
4. The techniques should be applied to join Mg alloy to other grades of stainless steels, such as ferritic, martensitic, and duplex stainless steels. Furthermore, advanced high strength steels, such dual-phase steel, transformation-induced plasticity steel, twinning-induced plasticity steel, are being developed for vehicles construction. The possibility of joining these steels to Mg alloy using the REW, RSWB, and REWB should be studied.
5. In vehicle design, three or more sheets are required in some complex structures, such as A-, B-, and C- pillars and at cross-member intersections. Therefore, it is important to study the possibility of using these techniques to join stack of multiple sheets

REFERENCES

Alenius, M., Pohjanne, P., Somervuori, M., & Hanninen, H. 2006. Exploring the mechanical properties of spot welded dissimilar joints for stainless and galvanized steels. *Welding Journal*. *85*12, 305.

Alizadeh-Sh, M., Pouranvari, M., & Marashi, S. 2015. Welding metallurgy of stainless steels during resistance spot welding Part II–heat affected zone and mechanical performance. *Science and Technology of Welding and Joining*. *20*6, 512-521.

Arghavani, M., Movahedi, M., & Kokabi, A. 2016. Role of zinc layer in resistance spot welding of aluminium to steel. *Materials & Design*. *102*, 106-114.

Aslanlar, S., Ogur, A., Ozsarac, U., & Ilhan, E. 2008. Welding time effect on mechanical properties of automotive sheets in electrical resistance spot welding. *Materials & Design. 29*7, 1427-1431. Retrieved from

ASTM. (2000). E384, Standard test method for microindentation hardness of materials *West Conshohocken, PA: ASTM International*.

AWS. (1982). Metals and Their Weldability. In W. H. Kearns (Ed.), *Welding Handbook* (7th ed., Vol. 4). Miami, FL: American Welding Society.

AWS. (2007). AWS D 17.2 : Specification for resistance welding for aerospace applications.

Babu, N. K., Brauser, S., Rethmeier, M., & Cross, C. 2012. Characterization of microstructure and deformation behaviour of resistance spot welded AZ31 magnesium alloy. *Materials Science and Engineering: A*. *549*, 149-156.

Behravesh, S. B., Jahed, H., & Lambert, S. 2011. Characterization of magnesium spot welds under tensile and cyclic loadings. *Materials & Design*. *32*10, 4890-4900. doi:DOI 10.1016/j.matdes.2011.06.001

Behravesh, S. B., Jahed, H., & Lambert, S. 2014. Fatigue characterization and modeling of AZ31B magnesium alloy spot-welds. *International journal of fatigue*. *64*0, 1-13.

Burmeister, L. C. (1993). *Convective heat transfer*: John Wiley & Sons.

Cao, X., Jahazi, M., Immarigeon, J., & Wallace, W. 2006. A review of laser welding techniques for magnesium alloys. *Journal of Materials Processing Technology*. *171*2, 188-204.

Chang, B., Shi, Y., & Dong, S. 1999. A study on the role of adhesives in weld-bonded joints. *Welding Journal*. *78*, 275-s.

Charde, N., Yusof, F., & Rajkumar, R. 2014. Material characterizations of mild steels, stainless steels, and both steel mixed joints under resistance spot welding (2-mm sheets). *The International Journal of Advanced Manufacturing Technology*. *75*1-4, 373-384.

Cukovic, J. P., Klopcic, B., Petrun, M., Polajzer, B., & Dolinar, D. 2014. Optimization of Resistance Spot Welding Transformer Windings Using Analytical Successive Approximation and Differential Evolution. *Ieee Transactions on Magnetics*. *50*4.

Davis, M. (2007). *Best practice in adhesive-bonded structures and repairs*: US Department of Transportation, Federal Aviation Administration.

De Tiedra, P., Martín, Ó., López, M., & San-Juan, M. 2011. Use of EPR test to study the degree of sensitization in resistance spot welding joints of AISI 304 austenitic stainless steel. *Corrosion Science*. *53*4, 1563-1570.

Eizadi, H., & Marashi, S. 2016. On the resistance spot welding of four-sheet stack of unequal sheet thickness. *Science and Technology of Welding and Joining*, 1-6.

Eshraghi, M., Tschopp, M. A., Zaeem, M. A., & Felicelli, S. D. 2014. Effect of resistance spot welding parameters on weld pool properties in a DP600 dual-phase steel: A parametric study using thermomechanically-coupled finite element analysis. *Materials & Design*. *56*, 387-397.

Fan, Q., Xu, G., & Gu, X. 2016. Expulsion characterization of stainless steel resistance spot welding based on dynamic resistance signal. *Journal of Materials Processing Technology*. *236*, 235-240.

Feng, J. C., Wang, Y. R., & Zhang, Z. D. 2006. Nugget growth characteristic for AZ(31)B magnesium alloy during resistance spot welding. *Science and Technology of Welding and Joining*. *11*2, 154-162.

Feng, M., Li, Y., Zhao, C., & Luo, Z. 2016a. Mechanical properties and interface morphology of Mg/Al ultrasonic spot weld bonding welds. *Science and Technology of Welding and Joining*. *21*8, 688-699.

Feng, Y., Li, Y., Luo, Z., Ling, Z., & Wang, Z. 2016b. Resistance spot welding of Mg to electro-galvanized steel with hot-dip galvanized steel interlayer. *Journal of Materials Processing Technology*. *236*, 114-122.

Feng, Y., Luo, Z., Li, Y., & Ling, Z. 2015. A Novel Method for Resistance Plug Welding of 7075 Aluminum Alloy. *Materials and Manufacturing Processes*, 1-7.

Florea, R., Bammann, D., Yeldell, A., Solanki, K., & Hammi, Y. 2013. Welding parameters influence on fatigue life and microstructure in resistance spot welding of 6061-T6 aluminum alloy. *Materials & Design*. *45*, 456-465.

Fujii, T., Tohgo, K., Suzuki, Y., Yamamoto, T., & Shimamura, Y. 2016. Fatigue strength and fatigue fracture mechanism of three-sheet spot weld-bonded joints under tensile–shear loading. *International journal of fatigue*. *87*, 424-434.

Fukumoto, S., Fujiwara, K., Toji, S., & Yamamoto, A. 2008a. Small-scale resistance spot welding of austenitic stainless steels. *Materials Science and Engineering: A*. *492*1, 243-249.

Fukumoto, S., Matsuo, T., Kuroda, D., & Yamamoto, A. 2008b. Weldability of Nickel-Free Austenitic Stainless Steel Thin Sheet by Small-Scale Resistance Spot Welding. *Materials Transactions*. *49*12, 2844-2849.

Goodarzi, M., Marashi, S., & Pouranvari, M. 2009. Dependence of overload performance on weld attributes for resistance spot welded galvanized low carbon steel. *Journal of Materials Processing Technology*. *209*9, 4379-4384.

Gould, J. 2012. Joining aluminum sheet in the automotive industry—A 30 year history. *Weld. J. 91*, 23-34.

Gould, J., Khurana, S., & Li, T. 2006. Predictions of microstructures when welding automotive advanced high-strength steels. *Welding Journal*. *85*5, 111.

Hamidinejad, S. M., Kolahan, F., & Kokabi, A. H. 2012. The modeling and process analysis of resistance spot welding on galvanized steel sheets used in car body manufacturing. *Materials & Design*. *34*0, 759-767.

Han, L., Thornton, M., Boomer, D., & Shergold, M. 2011a. A correlation study of mechanical strength of resistance spot welding of AA5754 aluminium alloy. *Journal of Materials Processing Technology*. *211*3, 513-521.

Han, L., Thornton, M., Li, D., & Shergold, M. 2011b. Effect of governing metal thickness and stack orientation on weld quality and mechanical behaviour of resistance spot welding of AA5754 aluminium. *Materials & Design*. *32*4, 2107-2114.

Han, L., Thornton, M., & Shergold, M. 2010. A comparison of the mechanical behaviour of self-piercing riveted and resistance spot welded aluminium sheets for the automotive industry. *Materials & Design*. *31*3, 1457-1467.

Hassanifard, S., & Feyzi, M. 2015. Analytical solution of temperature distribution in resistance spot welding. *Journal of Mechanical Science and Technology*. *29*2, 777-784.

Henkel. (2017). http://na.henkel-adhesives.com/product-search-1554.htm?nodeid=8797912825857.

Holtschke, N., & Jüttner, S. 2016. Joining lightweight components by short-time resistance spot welding. *Welding in the World*, 1-9. doi:10.1007/s40194-016-0398-5

http://www.crct.polymtl.ca/fact/phase_diagram.php?file=Fe-Mg.jpg&dir=TDnucl. Accessed 4th July, 2017.

Innojoin. (2017). Development and evaluation of advanced welding technologies for multi-material design with dissimilar sheet metals. http://www.innovatienetwerk.be/attachments/get/4818/InnoJoin_-_Summary_-_part_1.pdf.

Jiang, X., Yu, H., Lin, Q., & Xu, R. 2015. *Effects of Cu-Zn alloy additions on microstructure and strength of welded joints between magnesium alloy and mild* *steel*. Paper presented at the International Conference on Mechatronics, Electronic, Industrial and Control Engineering (MEIC 2015).

Karcı, F., Kacar, R., & Gündüz, S. 2009. The effect of process parameter on the properties of spot welded cold deformed AISI304 grade austenitic stainless steel. *Journal of Materials Processing Technology*. *209*8, 4011-4019.

Karimi, M., Sedighi, M., & Afshari, D. 2015. Thermal contact conductance effect in modeling of resistance spot welding process of aluminum alloy 6061-T6. *The International Journal of Advanced Manufacturing Technology*. *77*5-8, 885-895.

Khan, M. F., Sharma, G., & Dwivedi, D. 2015. Weld-bonding of 6061 aluminium alloy. *The International Journal of Advanced Manufacturing Technology*. *78*5-8, 863-873.

Kianersi, D., Mostafaei, A., & Amadeh, A. A. 2014a. Resistance spot welding joints of AISI 316L austenitic stainless steel sheets: Phase transformations, mechanical properties and microstructure characterizations. *Materials & Design*. *61*, 251-263.

Kianersi, D., Mostafaei, A., & Mohammadi, J. 2014b. Effect of Welding Current and Time on the Microstructure, Mechanical Characterizations, and Fracture Studies of Resistance Spot Welding Joints of AISI 316L Austenitic Stainless Steel. *Metallurgical and Materials Transactions A*. *45*10, 4423-4442.

Kitahara, H., Ueji, R., Tsuji, N., & Minamino, Y. 2006. Crystallographic features of lath martensite in low-carbon steel. *Acta Materialia*. *54*5, 1279-1288.

Kou, S. 1987. Welding metallurgy. *New York*.

Krauss, G. 1999. Martensite in steel: strength and structure. *Materials Science and Engineering: A*. *273*, 40-57.

Lai, W., & Pan, J. 2015. Failure mode and fatigue behavior of weld-bonded lap-shear specimens of magnesium and steel sheets. *International journal of fatigue*. *75*, 184-197.

Lang, B., Sun, D., Li, G., & Qin, X. 2008. Effects of welding parameters on microstructure and mechanical properties of resistance spot welded magnesium alloy joints. *Science and Technology of Welding & joining*. *13*8, 698-704.

Li, L., Tan, C., Chen, Y., Guo, W., & Song, F. 2013. Comparative study on microstructure and mechanical properties of laser welded–brazed Mg/mild steel and Mg/stainless steel joints. *Materials & Design*. *43*, 59-65.

Li, Y., Luo, Z., Yan, F. Y., Duan, R., & Yao, Q. 2014. Effect of external magnetic field on resistance spot welds of aluminum alloy. *Materials & Design*. *56*, 1025-1033. doi:10.1016/j.matdes.2013.12.005

Li, Y., Yan, F. Y., Luo, Z., Chao, Y. J., Ao, S. S., & Cui, X. T. 2015a. Weld Growth Mechanisms and Failure Behavior of Three-Sheet Resistance Spot Welds Made of 5052 Aluminum Alloy. *Journal of Materials Engineering and Performance*. *24*6, 2546-2555.

Li, Y., Zhang, Y., Bi, J., & Luo, Z. 2015b. Impact of electromagnetic stirring upon weld quality of Al/Ti dissimilar materials resistance spot welding. *Materials & Design*. *83*, 577-586.

Li, Y., Zhang, Y., & Luo, Z. 2015c. Microstructure and mechanical properties of Al/Ti joints welded by resistance spot welding. *Science and Technology of Welding and Joining*.

Liao, L., & Huang, C. 2016. Numerical analysis of effects of adhesive type and geometry on mixed-mode failure of adhesive joint. *International Journal of Adhesion and Adhesives*. *68*, 389-396.

Ling, Z., Li, Y., Luo, Z., Feng, Y., & Wang, Z. 2016. Resistance element welding of 6061 aluminum alloy to uncoated 22MnMoB boron steel. *Materials and Manufacturing Processes*. *31*16, 2174-2180.

Lippold, J. C., & Kotecki, D. J. (2005). *Welding metallurgy and weldability of stainless steels*. Hoboken, New Jersy: John Wiley & Sons, Inc.

Liu, L. (2010). 3 - Preparation for welding of magnesium alloys. In L. Liu (Ed.), *Welding and Joining of Magnesium Alloys* (pp. 16-22): Woodhead Publishing.

Liu, L., Feng, J., & Zhou, Y. (2010a). 18 - Resistance spot welding of magnesium alloys. In L. Liu (Ed.), *Welding and Joining of Magnesium Alloys* (pp. 351-367e): Woodhead Publishing.

Liu, L., Ren, D., & Li, Y. 2011. Static mechanics analyses of different laser weld bonding structures in joining AZ61 Mg alloy. *International Journal of Adhesion and Adhesives*. *31*7, 660-665.

Liu, L., Xiao, L., Chen, D., Feng, J., Kim, S., & Zhou, Y. 2013. Microstructure and fatigue properties of Mg-to-steel dissimilar resistance spot welds. *Materials & Design*. *45*, 336-342.

Liu, L., Xiao, L., Feng, J. C., Tian, Y. H., Zhou, S. Q., & Zhou, Y. 2010b. The Mechanisms of Resistance Spot Welding of Magnesium to Steel. *Metallurgical and Materials Transactions a-Physical Metallurgy and Materials Science*. *41a*10, 2651-2661.

Liu, L., Xiao, L., Feng, J. C., Tian, Y. H., Zhou, S. Q., & Zhou, Y. 2010c. Resistance Spot Welded AZ31 Magnesium Alloys, Part II: Effects of Welding Current on Microstructure and Mechanical Properties. *Metallurgical and Materials Transactions a-Physical Metallurgy and Materials Science*. *41a*10, 2642-2650.

Liu, L., Zhou, S., Tian, Y., Feng, J., Jung, J., & Zhou, Y. 2009. Effects of surface conditions on resistance spot welding of Mg alloy AZ31. *Science and Technology of Welding & joining*. *14*4, 356-361.

Liu, L. M., Wang, H., Song, G., & Ye, J. N. 2007. Microstructure characteristics and mechanical properties of laser weld bonding of magnesium alloy to aluminum alloy. *Journal of Materials Science*. *42*2, 565-572.

Ma, Y., Tao, W., Li, L., Wang, M., Chen, Y., & Wang, Y. 2012. Laser spot weld bonding of mild steel. *International Journal of Adhesion and Adhesives*. *34*, 1-5.

Manladan, S., Yusof, F., Ramesh, S., & Fadzil, M. 2016. A review on resistance spot welding of magnesium alloys. *The International Journal of Advanced Manufacturing Technology*. *86*5, 1805-1825.

Manladan, S., Yusof, F., Ramesh, S., Fadzil, M., Luo, Z., & Ao, S. 2017a. A review on resistance spot welding of aluminum alloys. *The International Journal of Advanced Manufacturing Technology*. *90*1, 605–634.

Manladan, S., Yusof, F., Ramesh, S., Zhang, Y., Luo, Z., & Ling, Z. 2017b. Microstructure and mechanical properties of resistance spot welded in welding-brazing mode and resistance element welded magnesium alloy/austenitic stainless steel joints. *Journal of Materials Processing Technology*.

Marashi, P., Pouranvari, M., Amirabdollahian, S., Abedi, A., & Goodarzi, M. 2008a. Microstructure and failure behavior of dissimilar resistance spot welds between low carbon galvanized and austenitic stainless steels. *Materials Science and Engineering: A*. *480*1, 175-180.

Marashi, P., Pouranvari, M., Sanaee, S., Abedi, A., Abootalebi, S., & Goodarzi, M. 2008b. Relationship between failure behaviour and weld fusion zone attributes of austenitic stainless steel resistance spot welds. *Materials Science and Technology*. *24*12, 1506-1512.

Marques, G., Campilho, R., da Silva, F., & Moreira, R. 2016. Adhesive selection for hybrid spot-welded/bonded single-lap joints: Experimentation and numerical analysis. *Composites Part B: Engineering*. *84*, 248-257.

Meschut, G., Hahn, O., Janzen, V., & Olfermann, T. 2014a. Innovative joining technologies for multi-material structures. *Welding in the World*. *58*1, 65-75.

Meschut, G., Janzen, V., & Olfermann, T. 2014b. Innovative and highly productive joining technologies for multi-material lightweight car body structures. *Journal of Materials Engineering and Performance*. *23*5, 1515-1523.

Meschut, G., Schmal, C., & Olfermann, T. 2017. Process characteristics and load-bearing capacities of joints welded with elements for the application in multi-material design. *Welding in the World*. *61*3, 435-442.

Min, D., Yong, Z., & Jie, L. 2015. Dissimilar spot welding joints of AZ31-443 ferritic stainless steel with cover plate. *The International Journal of Advanced Manufacturing Technology*, 1-7.

Moshayedi, H., & Sattari-Far, I. 2012. Numerical and experimental study of nugget size growth in resistance spot welding of austenitic stainless steels. *Journal of Materials Processing Technology*. *212*2, 347-354.

Niknejad, S., Liu, L., Lee, M.-Y., Esmaeili, S., & Zhou, N. Y. 2014. Resistance spot welding of AZ series magnesium alloys: Effects of aluminum content on microstructure and mechanical properties. *Materials Science and Engineering: A. 618*, 323-334.

Niknejad, S. T., Liu, L., Nguyen, T., Lee, M.-Y., Esmaeili, S., & Zhou, N. Y. 2013. Effects of Heat Treatment on Grain-Boundary β-Mg17Al12 and Fracture Properties of Resistance Spot-Welded AZ80 Mg Alloy. *Metallurgical and Materials Transactions A. 44*8, 3747-3756.

Özyürek, D. 2008. An effect of weld current and weld atmosphere on the resistance spot weldability of 304L austenitic stainless steel. *Materials & Design*. *29*3, 597-603.

Patel, V. K., Bhole, S. D., & Chen, D. L. 2013. Formation of zinc interlayer texture during dissimilar ultrasonic spot welding of magnesium and high strength low alloy steel. *Materials & Design*. *45*, 236-240.

Patel, V. K., Bhole, S. D., & Chen, D. L. 2014. Fatigue life estimation of ultrasonic spot welded Mg alloy joints. *Materials & Design*. *62*, 124-132. doi:DOI 10.1016/j.matdes.2014.05.008

Pereira, A., Ferreira, J., Antunes, F., & Bártolo, P. 2009. Study on the fatigue strength of AA 6082-T6 adhesive lap joints. *International Journal of Adhesion and Adhesives*. *29*6, 633-638.

Pereira, A., Ferreira, J., Antunes, F., & Bártolo, P. 2014. Assessment of the fatigue life of aluminium spot-welded and weld-bonded joints. *Journal of Adhesion Science and Technology*. *28*14-15, 1432-1450.

Pereira, A., Ferreira, J., Loureiro, A., Costa, J., & Bártolo, P. 2010. Effect of process parameters on the strength of resistance spot welds in 6082-T6 aluminium alloy. *Materials & Design*. *31*5, 2454-2463.

Poggio, S., Ponte, M., Gambaro, C., & Adamowski, J. (2005). *Resistance spot welding of advanced high strength steel DP600.* Paper presented at the Proc. 1st Int. Conf. on 'Super high strength steels', Rome, Italy.

Pouranvari, M. 2017. Fracture toughness of martensitic stainless steel resistance spot welds. *Materials Science and Engineering: A. 680*, 97-107.

Pouranvari, M., Abedi, A., Marashi, P., & Goodarzi, M. 2008. Effect of expulsion on peak load and energy absorption of low carbon steel resistance spot welds. *Science and Technology of Welding and Joining*. *13*1, 39-43.

Pouranvari, M., Alizadeh-Sh, M., & Marashi, S. 2015a. Welding metallurgy of stainless steels during resistance spot welding Part I: fusion zone. *Science and Technology of Welding and Joining*. *20*6, 502-511.

Pouranvari, M., Khorramifar, M., & Marashi, P. 2016. Ferritic–austenitic stainless steels dissimilar resistance spot welds: metallurgical and failure characteristics. *Science and Technology of Welding & joining*.

Pouranvari, M., & Marashi, S. 2010. On the failure of low carbon steel resistance spot welds in quasi-static tensile–shear loading. *Materials & Design*. *31*8, 3647-3652.

Pouranvari, M., & Marashi, S. 2012. Failure mode transition in AISI 304 resistance spot welds. *Welding Journal*. *91*, 303-309.

Pouranvari, M., & Marashi, S. 2013. Critical review of automotive steels spot welding: process, structure and properties. *Science and Technology of Welding and Joining*. *18*5, 361-403.

Pouranvari, M., Marashi, S., & Alizadeh-Sh, M. 2015b. Welding metallurgy of dissimilar AISI 430/DQSK steels resistance spot welds. *Welding Journal*.

Pouranvari, M., Mousavizadeh, S., Marashi, S., Goodarzi, M., & Ghorbani, M. 2011. Influence of fusion zone size and failure mode on mechanical performance of dissimilar resistance spot welds of AISI 1008 low carbon steel and DP600 advanced high strength steel. *Materials & Design*. *32*3, 1390-1398.

Qiu, R., Wang, N., Shi, H., Cui, L., Hou, L., & Zhang, K. 2015. Joining steel to aluminum alloy by resistance spot welding with a rivet. *International Journal of Materials Research*. *106*1, 60-65.

Qiu, R., Wang, N., Shi, H., Zhang, K., & Satonaka, S. 2014. Non-parametric effects on pore formation during resistance spot welding of magnesium alloy. *Science and Technology of Welding and Joining*. *19*3, 231-234.

Qiu, R. F., Satonaka, S., & Iwamoto, C. 2009. Mechanical properties and microstructures of magnesium alloy AZ31B joint fabricated by resistance spot welding with cover plates. *Science and Technology of Welding and Joining*. *14*8, 691-697.

Qiu, R. F., Shi, H. X., Yu, H., Zhang, K. K., Tu, Y. M., & Satonaka, S. 2010. Effects of Electrode Force on the Characteristic of Magnesium Alloy Joint Welded by Resistance Spot Welding with Cover Plates. *Materials and Manufacturing Processes*. *25*11, 1304-1308.

Radakovic, D., & Tumuluru, M. 2008. Predicting resistance spot weld failure modes in shear tension tests of advanced high-strength automotive steels. *Welding Journal*. *87*4, 96.

RWMA. (2003). Resistance welding manual: RWMA, Philadelphia, PA.

Safanama, D., Marashi, S., & Pouranvari, M. 2012. Similar and dissimilar resistance spot welding of martensitic advanced high strength steel and low carbon steel: metallurgical characteristics and failure mode transition. *Science and Technology of Welding and Joining*. *17*4, 288-294.

Sam, S., & Shome, M. 2010. Static and fatigue performance of weld bonded dual phase steel sheets. *Science and Technology of Welding and Joining*. *15*3, 242-247.

Satonaka, S., Iwamoto, C., Murakami, G. I., & Matsumoto, Y. 2012. Resistance Spot Welding of Magnesium Alloy Sheets with Cover Plates. *Welding in the World*. *56*7-8, 44-50.

Schuberth, S., Schedin, E., Frohlich, T., & Ratte, E. (2008). *Next generation vehicle engineering guidelines for stainless steel in automotive applications.* Paper presented at the 6th Stainless Steel Science and Market Conference, Helsinki, Finland.

Senkara, J., Zhang, H., & Hu, S. 2004. Expulsion prediction in resistance spot welding. *Welding Journal*. *83*4, 123-S.

Shen, J., Zhang, Y., Lai, X., & Wang, P. 2012. Adhesive placement in weld-bonding multiple stacks of steel sheets. *Welding Journal*. *91*5.

Shi, H. X., Qiu, R. F., Zhu, J. H., Zhang, K. K., Yu, H., & Ding, G. J. 2010. Effects of welding parameters on the characteristics of magnesium alloy joint welded by resistance spot welding with cover plates. *Materials & Design*. *31*10, 4853-4857.

Tamizi, M., Pouranvari, M., & Movahedi, M. 2017. Welding metallurgy of martensitic advanced high strength steels during resistance spot welding. *Science and Technology of Welding and Joining*. *22*4, 327-335.

Tao, W., Ma, Y., Chen, Y., Li, L., & Wang, M. 2014. The influence of adhesive viscosity and elastic modulus on laser spot weld bonding process. *International Journal of Adhesion and Adhesives*. *51*, 111-116.

Wang, Y., Feng, J., & Zhang, Z. 2006. Microstructure characteristics of resistance spot welds of AZ31 Mg alloy. *Science and Technology of Welding & joining*. *11*5, 555-560.

Wang, Y., Mo, Z., Feng, J., & Zhang, Z. 2007. Effect of welding time on microstructure and tensile shear load in resistance spot welded joints of AZ31 Mg alloy. *Science and Technology of Welding & joining*. *12*8, 671-676.

Wei, P. S., Wu, T. H., & Chen, L. J. 2013. Joint Quality Affected by Electrode Contact Condition During Resistance Spot Welding. *Components, Packaging and Manufacturing Technology, IEEE Transactions on*. *3*12, 2164-2173.

Williams, N., & Parker, J. 2004. Review of resistance spot welding of steel sheets Part 1 Modelling and control of weld nugget formation. *International Materials Reviews*. *49*2, 45-75. Retrieved from

Xiao, L., Liu, L., Chen, D. L., Esmaeili, S., & Zhou, Y. 2011. Resistance spot weld fatigue behavior and dislocation substructures in two different heats of AZ31 magnesium alloy. *Materials Science and Engineering: A*. *529*0, 81-87.

Xiao, L., Liu, L., Esmaeili, S., & Zhou, Y. 2012. Microstructure Refinement After the Addition of Titanium Particles in AZ31 Magnesium Alloy Resistance Spot Welds. *Metallurgical and Materials Transactions A*. *43*2, 598-609.

Xiao, L., Liu, L., Zhou, Y., & Esmaeili, S. 2010. Resistance-spot-welded AZ31 magnesium alloys: Part I. Dependence of fusion zone microstructures on second-phase particles. *Metallurgical and Materials Transactions A*. *41*6, 1511-1522.

Xu, W., Chen, D., Liu, L., Mori, H., & Zhou, Y. 2012. Microstructure and mechanical properties of weld-bonded and resistance spot welded magnesium-to-steel dissimilar joints. *Materials Science and Engineering: A*. *537*, 11-24.

Xu, W., Liu, L., Zhou, Y., Mori, H., & Chen, D. 2013. Tensile and fatigue properties of weld-bonded and adhesive-bonded magnesium alloy joints. *Materials Science and Engineering: A*. *563*, 125-132.

Yao, Q., Luo, Z., Li, Y., Yan, F., & Duan, R. 2014. Effect of electromagnetic stirring on the microstructures and mechanical properties of magnesium alloy resistance spot weld. *Materials & Design*. *63*, 200-207.

Yovanovich, M. (2006). *Micro and macro hardness measurements, correlations, and contact models.* Paper presented at the Collection of technical papers—44th AIAA aerospace sciences meeting.

Yuan, T., Chai, X., Luo, Z., & Kou, S. 2015. Predicting susceptibility of magnesium alloys to weld-edge cracking. *Acta Materialia*. *90*, 242-251.

Yuan, X., Li, C., Chen, J., Li, X., Liang, X., & Pan, X. 2017. Resistance spot welding of dissimilar DP600 and DC54D steels. *Journal of Materials Processing Technology*. *239*, 31-41.

Zhang, G., Tian, C., Liu, L., & Xu, R. 2014a. *Interfacial structure of the joints between magnesium alloy and mild steel with nickel as interlayer*. Paper presented at the International Conference on Logistics Engineering, Management and Computer Science (LEMCS 2014).

Zhang, H., & Senkara, J. (2011). *Resistance welding: fundamentals and applications*: CRC press.

Zhang, N., Wang, W., Cao, X., & Wu, J. 2015. The effect of annealing on the interface microstructure and mechanical characteristics of AZ31B/AA6061 composite plates fabricated by explosive welding. *Materials & Design*. *65*, 1100-1109.

Zhang, W., Qiu, X., Sun, D., & Han, L. 2011. Effects of resistance spot welding parameters on microstructures and mechanical properties of dissimilar material joints of galvanised high strength steel and aluminium alloy. *Science and Technology of Welding and Joining*. *16*2, 153-161.

Zhang, Y., Li, Y., Luo, Z., Feng, Y., & Zhou, J. 2016. Effect of joint design on the failure behaviour of three-stack-up austenitic stainless steel resistance spot welds. *Science and Technology of Welding and Joining*, 1-9.

Zhang, Y., Sun, H., Wang, P.-C., & Chen, G. 2014b. Improvement of Process Robustness in Weld Bonding of Galvanized DP780 Steel. *Welding Journal*. *93*12, 472S-481S.

Zhou, S., Liu, L., Jung, J. P., Lee, M.-Y., & Zhou, Y. N. 2010. Effects of welding parameters and surface pretreatments on resistance spot welding of AZ31B Mg alloy. *Metals and Materials International*. *16*6, 967-974.

Zhu, T., Chen, Z. W., & Gao, W. 2010. Effect of cooling conditions during casting on fraction of β-Mg 17 Al 12 in Mg–9Al–1Zn cast alloy. *Journal of Alloys and Compounds*. *501*2, 291-296.

LIST OF PUBLICATIONS AND PAPERS PRESENTED

Publications

1. Manladan, S., Yusof, F., Ramesh, S., & Fadzil, M. 2016. A review on resistance spot welding of magnesium alloys. *The International Journal of Advanced Manufacturing Technology*. *86*5, 1805-1825.

2. Manladan, S., Yusof, F., Ramesh, S., Zhang, Y., Luo, Z., & Ling, Z. 2017b. Microstructure and mechanical properties of resistance spot welded in welding-brazing mode and resistance element welded magnesium alloy/austenitic stainless steel joints. *Journal of Materials Processing Technology*.

3. Manladan, S., Yusof, F., Ramesh, S., Fadzil, M., Luo, Z., & Ao, S. 2017a. A review on resistance spot welding of aluminum alloys. *The International Journal of Advanced Manufacturing Technology*. *90*1, 605–634.

Papers presented

1. Manladan, S., Yusof, F., Ramesh, S., Zhang, Y., Luo, Z., & Ling, Z . Resistance element welding of magnesium alloy/austenitic stainless steel. Joining and Welding Symposium 2017, Universiti Malaysia Pahang